PhD-FSTM-2023-07
The Faculty of Science, Technology and Medicine

DISSERTATION

Defence held on 07/07/2023 in Luxembourg

to obtain the degree of

DOCTEUR DE L'UNIVERSITÉ DU LUXEMBOURG EN SCIENCES DE L'INGÉNIEUR

by

Navid Aminnia
Born on 09 September 1991 in Gorgan, Iran

CFD-XDEM COUPLING APPROACH TOWARDS MELT POOL SIMULATIONS OF SELECTIVE LASER MELTING

DISSERTATION DEFENSE COMMITTEE

Dr. Bernhard Peters, Dissertation Supervisor
Professor, University of Luxembourg, Luxembourg

Dr. Alexander Tkatchenko, Chair
Professor, University of Luxembourg, Luxembourg

Dr. Alvaro Estupinan, Vice-Chair
Postdoctoral Researcher, University of Luxembourg, Luxembourg

Dr. Eric Wyart, Member
Directeur Opérationnel, Réseau LiEU

Dr. Davide Baroli, Member
Postdoctoral Researcher, USI Università della Svizzera italiana

Acknowledgement

I would like to express my sincerest gratitude to my supervisor Prof. Bernhard Peters for his exceptional guidance and unwavering support throughout my PhD journey. His excellent management and valuable feedback have been instrumental in shaping my research and enhancing my professional development. I am greatly thankful to his mentorship in my path to the achievement of my Doctor of Philosophy qualification.

Besides my supervisor, I would like to thank the thesis committee: Prof. Alexander Tkatchenko and Dr. Eric Wyart for their constructive comments and suggestions during the annual meetings, which helped to improve the quality of this work. My sincere thanks to Dr. Alvaro Estupinan and Dr. Davide Baroli for their friendly and effective guidance and support throughout my PhD study.

I would like to sincerely thank all my colleagues in LuXDEM team, especially Dr. Xavier Besseron for his helpful assistance with IT issues. Dr. Daniel Louw for the productive modeling discussions that we had. Fateme Darlik, Prasad Adhav, Sina Hassanzadeh, Dr. Muhammad Mashhood and Dr. Vikram Sundara for their friendship and the memorable time that we had at the University of Luxembourg. I would also like to thank my dear friends Dr. Pooyan Heravi, Dr. Faezeh Moshfeghifar and Ahmad Kolahdooz for their insightful comments and discussions over the years.

I would like to express my heartfelt gratitude to my late mother, who was a constant source of love and support throughout my life. As well an immense gratitude towards my father and my brothers Saeed and Vahid who have always been a source of inspiration and unwavering support.

I also appreciate the administrative assistance of Odile Marois through out my study. Finally, I gratefully acknowledge the Fonds National de la Recherche (FNR) in Luxembourg, making this project possible with their financial and administrative support (grant reference no. 13558062).

Navid Aminnia
University of Luxembourg
July 2023

Abstract

Within the domain of metal Additive Manufacturing (AM), the challenge of qualification emerges prominently. This challenge encapsulates the endeavor to establish a set of process parameters that can reliably yield consistent and repeatable production outcomes. While additive manufacturing technologies like selective laser melting (SLM) have gained widespread usage for crafting metal parts boasting intricate geometries and high precision, they are not exempt from critical concerns. Defects, most notably porosities, persist as a substantial hurdle. The origin of these imperfections lies in microscale phenomena inherent to the melting and solidification processes occurring during layer-by-layer fabrication.

This study presents a Computational Fluid Dynamics-eXtended Discrete Element Method (CFD-XDEM) coupling to model the dynamics and thermodynamic interplay between the powder bed and melt pool during SLM. The XDEM model simulates various aspects of powder behavior, including deposition, heating via laser radiation, melting, shrinkage, and the associated transfer of mass, momentum, and energy between the particles and the surrounding liquid and gas. The CFD model is based on the Volume Of Fluid (VOF) method and simulates the formation and evolution of the melt pool, taking into account surface tension force, Marangoni flow, buoyancy-driven flow inside the melt pool, phase change (solidification and melting), and the laser radiation on the melt surface. A direct coupling establishes a bidirectional transfer of source term data between the XDEM and the CFD . This involves the exchange of information such as the mass source of molten metal, convective heat transfer between particles and the fluid mixture, as well as the drag forces acting between the liquid and the particles in both directions. This direct coupling is achieved through the incorporation of source terms within the equations of the XDEM and CFD models.

The present study is currently undertaking a comprehensive validation of the proposed method throughout each stage of development. This validation involves comparing model results with experimental data and benchmark problems. To initiate the process, the Marangoni model is being

validated against benchmark problems. Subsequently, the laser model is being implemented to predict the results of a laser melting experiment on a metal block. As the CFD model is finalized, the coupling is concurrently being developed. To validate the reliability of heat, mass, and momentum transfer within the coupling, an experiment involving the melting of ice is being replicated. This experiment serves as a method to affirm the performance of the melting model. The outcomes of this experiment are providing validation for the CFD-XDEM coupling's performance. Moving forward, the model is being utilized to predict outcomes for a low-power SLM experiment involving a single layer, considering various laser scanning velocities. Impressively, the simulation outcomes are demonstrating excellent agreement with experimental data. This alignment is underlining the model's capacity to accurately forecast melt pool dimensions. Furthermore, the model is being extended to simulate a larger powder bed, enabling an examination of melt pool characteristics as well as heat transfer interactions with the powder particles.

The model presented in this study offers several distinctive features: The phase change of the particles is explicitly solved in the XDEM model, with particles undergoing melting at the melting temperature, shrinking, and disappearing when they are completely melted. The XDEM model solves for conduction and radiation between adjacent particles, providing an advantage over continuous powder bed models that require an estimate of effective thermal conductivity. Moreover, The particles are modeled as one-dimensional elements instead of 3-dimensional CFD spherical geometries, which is anticipated to be computationally more efficient. The CFD model incorporates all the relevant physical phenomena to the dynamics of melt pool, including Marangoni flow, buoyancy-driven flow, and surface tension forces. The volumetric heat source for the laser radiation is adaptive to the geometry of melt pool.

The proposed model offers a reliable and efficient method for predicting the behavior of melt pool, and it is expected to facilitate the optimization of SLM process parameters to reduce the defects and improve the quality of manufactured parts.

Contents

List of Figures

List of Tables

Chapter 1

Introduction

1.1 Preface

Additive manufacturing, also known as 3D printing, is an innovative method of manufacturing that operates under the fundamental principle of constructing 3D designs directly from computer-aided design (CAD) files, without the need for any specialized tools or dies tailored to individual parts [1]. Additive manufacturing involves a process of building parts and components by consolidating successive layers of material. Each layer is a thin cross-sectional slice of the final product, contributing to the additive process that creates the 3D object. AM facilitates the production of near net shape parts, resulting in reduced waste generation when compared to conventional machining techniques. Furthermore, the absence of design limitations in AM allows for the optimization of parts to achieve both lighter weight and increased strength [2].

Numerous methods of additive manufacturing have been developed to fabricate metal parts, incorporating diverse combinations of stock material form, material delivery, and heat source to achieve the desired end result [3]. Additive manufacturing processes can be categorized based on the state of the raw material into liquid-based, solid-based, and powder-based classifications. The potential and versatility of powder and liquid-based methods are widely recognized due to their ability to be utilized across a wide range of materials. Within the powder bed fusion class, two distinct methods have emerged: Selective Laser Melting (SLM) and Electron Beam Melting (EBM). SLM utilizes a movable laser beam to melt particular areas of a metal powder bed while being shielded by an inert gas environment, while EBM replaces the laser beam with an electron beam and functions in a vacuum. In both scenarios, a roller or blade is utilized to distribute additional layers

of powder over the bed between each pass of the laser or electron beam.

Although SLM is one of the most promising AM technologies, the reproducibility and quality of the process remain a challenge due to the complex multiphysical phenomena associated with the process. These parameters encompass factors like laser power and scanning speed, thermophysical properties of the powder, as well as process conditions including preheat temperature and ambient gas composition. It is crucial to thoughtfully analyze these parameters to successfully attain the desired properties of the final part. To comprehend the intricate relationships between the manufacturing process and the resulting properties of the final product, a comprehensive understanding of the underlying physical phenomena involved in the process is essential. The utilization of modeling and simulation techniques represents a potent and economically feasible method for gaining insight into the governing mechanisms of the SLM process.

A complete simulation of the SLM process can be deconstructed into various sub-models. These models encompass diverse aspects, such as residual stress, microstructure evolution, powder-bed raking, and the intricate behavior in and around the melt pool [4]. Each of these topics has prompted extensive research endeavors aimed at developing models that exhibit high predictive capability. The ultimate objective is to attain a comprehensive model capable of serving as a digital twin to an SLM process. In this study, we have focused on developing a simulation framework for modeling the transport phenomena associated with the metal pool.

The dynamics and characteristics of the melt pool have a direct influence on the quality of the solidified part, with inadequate melting and fusion potentially causing defects and porosities in the final product. The "balling effect," characterized by un-melted powder clumping, and "keyhole porosities," voids formed due to melt pool instability especially at high-intensity laser powers, are phenomena that contribute to these issues [5]. Additionally, the microstructure of the solidified part is also strongly influenced by the melt pool geometry and temperature history of the heat-affected zone [6]. Therefore a significant amount of research has been directed towards developing models that can capture the formation and evolution of the melt pool in SLM process [4, 7, 3]. These models have employed different numerical methods. A comprehensive review of these methods is available in section 2.7.

In this study, we introduce a fully coupled computational fluid dynamics-discrete element method (CFD-XDEM) model designed to tackle a category of granular media problems that involve thermal phase change and particle-fluid interactions. The proposed model is utilized to simulate the SLM process. The powder particles' motion as well as their thermal behavior including melting is modeled in XDEM. The melt pool dynamics, including Marangoni flow, buoyancy-driven flow, surface tension, thermal behavior, and solidification are modeled in a Volume of Fluid (VOF) CFD model. The full particle-fluid interactions, i.e. mass, heat, and momentum transfer between them are performed via a direct coupling between XDEM and OpenFOAM. The proposed model is capable

of simulating multi-track SLM processes, and it can accurately predict the resulting geometry and thermal distribution of the solidified tracks. The data obtained from this simulation can then be inputted into a microstructure growth model to accurately predict the microstructural properties of the manufactured part.

1.2 Thesis Structure

The structure of this thesis is designed to follow a cumulative progression, and it is comprised of different chapters that collectively contribute to the exploration of the subject matter. The text begins with an introductory chapter in chapter 2, setting the stage for the subsequent exploration. Moving forward, chapters 3 to chapter 5 form the core of the thesis, consisting of a compilation of both published and submitted articles that collectively contribute to a comprehensive understanding of the subject matter.

Within this framework, chapter 2 serves as a foundational cornerstone, delivering an encompassing overview of the fundamental principles of additive manufacturing. This pivotal chapter is divided into several sections, each addressing distinct aspects. The emergence and evolution of additive manufacturing are unveiled in Section 2.3, tracing its trajectory to the establishment of an intricate industrial ecosystem. Section 2.4 subsequently introduces diverse additive manufacturing technologies, revealing their functionalities, strengths, and limitations. The spotlight then narrows onto the selective laser melting (SLM) process, the focal point of the study. In Section 2.6, the inherent defects inherent to the SLM process are meticulously discussed, outlining their implications for its broader applications. Concluding this chapter, the primary numerical methods adopted to dissect the intricate phenomena within the SLM process are comprehensively examined.

As we journey through the chapters, we encounter a seamless progression. chapter 3 delves into the heart of the research endeavor, highlighting its initial stages. The formulation and validation of the computational fluid dynamics (CFD) model takes center stage, followed by the integration of this model with the discrete element method (XDEM), validated through rigorous comparisons with experimental data. This chapter offers a panoramic view of the research evolution, encompassing foundational equations, validation exercises, and resultant findings. The model's efficacy in forecasting Marangoni flow within a laser-induced melt pool is underscored, accompanied by an intricately detailed representation of the intricate heat, mass, and momentum transfer between the CFD model and the particles in XDEM.

The subsequent chapter, chapter 4, ushers us into the next phase, concentrating on the model's verification through an experimental selective laser melting (SLM) process. Here, the theoretical bedrock of selective laser melting is meticulously laid out, explicating the nuances of source terms and process parameters embedded within the model. Moreover, this chapter unfurls the model's

ability to replicate a randomized powder bed, enabling the comprehensive simulation of the laser melting process. This, in turn, empowers a profound exploration into the fluid dynamics and thermodynamics that govern the intricate dance of the melt pool.

Lastly, chapter 5 extends the model's application, as it is harnessed to simulate the raceway region of iron-making blast furnaces. This marks a pivotal application point, where a three-dimensional raceway model is crafted to dissect the temperature distribution across varying working conditions.

In essence, the thesis structure creates a seamless narrative that unfolds through a sequence of interwoven chapters, each contributing a distinct layer to the exploration of the subject matter.

Chapter 2

Background

2.1 Preface

The aim of this chapter is to provide an introduction to additive manufacturing (AM), discussing the advantages that this technology offers compared to conventional manufacturing processes. The first part of the chapter examines the brief history of AM during its first three decades, with a particular focus on the pioneering companies that have led the development of this technology and the standardization efforts of organizations such as American Society for Testing and Materials (ASTM). Next, the chapter introduces and evaluates the most common AM processes. The following section explores the defects and deficiencies that AM has faced, and how the research community is addressing these issues. Finally, the chapter provides a summary of the different methods used to simulate additive manufacturing. By the end of this chapter, readers will have a comprehensive understanding of the state of the art in AM technology, its challenges, and its potential to revolutionize various industries.

2.2 Introduction to Additive Manufacturing

Additive manufacturing (AM) refers to a technique of building objects from 3-Dimensional (3D) model data by joining materials, typically layer by layer [8]. It encompasses a variety of terms such as additive fabrication, additive processes, additive techniques, additive layer manufacturing, and freeform fabrication. It can be applied to all kinds of materials, including metals, ceramics,

polymers, composites, and biological systems. Despite being used for material processing for over three decades, AM has only recently gained recognition as a crucial manufacturing technology in commercial industries.

Casting, forging, stamping, and machining stand as quintessential examples of conventional production techniques that have shaped industries for generations. In general, these processes entail making a mold or pattern, pouring in a liquid or heated substance, and letting it cool or solidify. The final product is then removed from the mold or pattern and may undergo additional processing, such as machining or polishing. Conventional manufacturing processes are well-established and frequently utilized, however additive manufacturing has significant benefits over traditional manufacturing methods:

Complex shapes and internal features: Additive manufacturing facilitates the creation of intricate forms and inner structures that would be challenging or unattainable through conventional fabrication methods. [2]. This includes overhangs, cavities, and interior channels.

Reduced waste: Excess material is frequently chopped away or wasted in conventional production to get the required form. In contrast, additive manufacturing provides precise control over the amount of material used, resulting in reduced waste [2].

Customization: As the digital model can be easily adjusted to match specific specifications, additive manufacturing allows for the production of customized items on demand. This enables more design flexibility and the capability to adapt swiftly to changing consumer demands [9].

Speed: Since it does not need the use of tooling or other specialized equipment, additive manufacturing can be faster than traditional production methods for some application [1].

Cost: Additive manufacturing has the potential to reduce costs for low-volume production runs since it eliminates the need for costly tooling. Additionally, as it eliminates the need for multiple manufacturing steps, it can be a more cost-effective approach for creating complex parts [1].

Material options: Additive manufacturing showcases remarkable material versatility, allowing for the utilization of an extensive array of substances, including metals, plastics, ceramics, and composites [9].

2.3 History of Additive Manufacturing Industry

Additive manufacturing or 3D printing, started in 1987 with the development of stereolithography (SL) by Chuck Hull [10]. SL involves using a laser to solidify layers of a UV light-sensitive liquid polymer to create an object layer by layer. Hull founded 3D Systems and released the first commercially available AM system, SLA-1 (as shown in Figure 2.1), which served as a predecessor to the popular SLA 250 machine. The term SLA stands for StereoLithography Apparatus [11].

Figure 2.1: SLA-1 machine by 3DSystems was the first commercially avaialable 3D printing system [11]

In the early 1990s, additive manufacturing (AM) saw pivotal advancements. Notably, Germany's Electro Optical Systems (EOS) introduced STEREOS, the company's first SL machine, in 1991, alongside the emergence of Fused Deposition Modeling (FDM) by Stratasys, Solid Ground Curing (SGC) by Cubital [12], and Laminated Object Manufacturing (LOM) by Helisys [13]. The mid-1990s witnessed more accessible 3D printing systems, featuring FDM, stereolithography, inkjet printing, and paper lamination. The early 2000s brought additional players like Helisys, Sanders Design International, and Buss Modeling Technology, marking a dynamic evolution of AM technologies during these years [14].

A new era in the 3D printing industry was ushered in during the first half of the 2000s with the introduction of innovative machines. One such machine was Quadra, a 3D inkjet printer developed by Objet Geometries of Israel in April 2000 [15]. It utilized 1,536 nozzles and a UV light source to deposit and harden photopolymer. Another significant development was the unveiling of Direct metal deposition (DMD) by Precision Optical Manufacturing (POM), a laser-cladding method that utilized metal powder for part production and repairs [16]. In the mid-2000s, several companies in the 3D printing industry introduced new machines and materials, including inkjet-printing for sand molds and cores, laser-sintering machines with speed improvements and new materials, and systems that combined laser sintering, marking, and machining [11]. During 2006 and 2007, numerous new machines were launched, along with the introduction of new materials, including those with improved durability and impact resistance. In 2008 and 2009, new technologies emerged, including precision wax-printing [17] and microfabrication technology for small electronic and sensing devices. New materials were also introduced, such as biocompatible FDM material [18] and Titanium Grade 2 for electron beam melting systems. Companies also entered into collaborative materials agreements to enhance their products [11].

In 2009, ASTM published its first additive manufacturing standard named F2792 [19]. It provided

a standard definition of AM and therefore a common language for those in the industry, including users, producers, researchers, educators, and the media. It established a set of standardized terms, definitions, and acronyms to ensure consistency and promote the development of AM standards. In 2010, 3D Systems continued to expand its operations in Europe through acquisitions [11].

In December 2012, The National Institute of Standards and Technology (NIST) in United States conducted a workshop, the findings of which were later published in a report titled "Measurement Science Roadmap for Metal-Based Additive Manufacturing" [20]. The report highlights significant technological challenges in four areas: (i) AM materials, (ii) AM process and equipment, (iii) AM qualification and certification, and (iv) AM modeling and simulation. The report also identifies opportunities for technology development, such as the creation of robust in-situ process monitoring techniques, the establishment of a metals design allowable and performance capability database, the development of a shared third party database, the creation of an expert system for AM design, and the validation of physics and properties-based models.

In 2013, The market for 3D printing and additive manufacturing experienced significant growth, with major equipment manufacturers acquiring related companies. This attracted the attention of the investment community, leading to an unprecedented appetite for AM-related companies and technology. This interest resulted in numerous IPOs and additional stock offerings, as well as the launch of the first mutual fund dedicated to 3D printing stocks. Furthermore, there was a noticeable increase in attendance at established conferences, and new events related to 3D printing emerged, demonstrating the heightened interest in this field [11].

In 2015, the International Organization for Standardization (ISO) and ASTM released their first joint standard for additive manufacturing processes, known as ISO/ASTM 52900 [21]. This new standard succeeded F2792 and was significant for its expansion of the original terminology used in F2792. ISO/ASTM 52900 was the first standard for additive manufacturing to be developed jointly by both ISO and ASTM International. Additionally, it was subsequently adopted by the European Committee for Standardization (CEN), signifying a coordinated effort among the world's standards bodies to unify and coordinate standards development in additive manufacturing across borders and industries.

The worldwide market for all products and services related to additive manufacturing (AM) experienced a significant growth rate of 25.9% in 2015, based on a compounded annual growth rate (CAGR). This growth rate was slightly lower compared to the previous three years' CAGR of 33.8%. However, when observed over a longer period of 27 years, the CAGR for the AM industry is an impressive 26.2%. According to Wohlers report [22], The number of manufacturers who sold industrial-grade AM systems in 2015 was 62, which is higher than the 49 manufacturers who sold them in the previous year, 2014. In addition, the number of manufacturers selling industrial systems in 2015 was double the number of manufacturers who sold these systems in 2011, which was

only 31. In 2016 the additive manufacturing industry had a 17.4% growth in revenues worldwide, reaching a total of $6.063 billion. The Wohlers Report 2017 [23] showed that 97 manufacturers sold AM systems, up from 62 in 2015 and 49 in 2014. New companies like GE Aviation, HP, Carbon, Markforged, and Additive Industries joined established industry leaders like EOS and EnvisionTEC. GE Aviation formed an official AM division in 2016 after acquiring Arcam and Concept Laser. In 2018 the industry continued to grow and topped $ 7 billion [24]. The number of AM system sold worldwide was nearly 80 precent more than the previous year. Based on the data presented in Figure 2.2, it can be observed that there was no growth in the number of sold AM systems in the following three years. However, the industry continued to strive especially in desktop 3D printers.

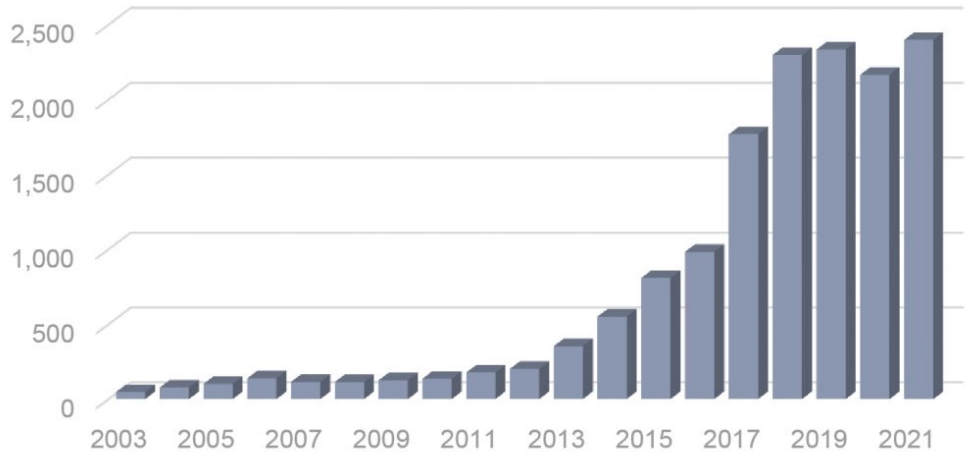

Figure 2.2: Number of metal AM machines sold worldwide from 2003 to 2021 [25]

Table 2.1 presents a summary of the AM industry, indicating that the industrial machinery, aerospace, and automotive sectors are the primary users of AM-produced goods which are results of a relevance analysis conducted in a project co-funded by the Erasmus Program of the European Union. However, it is predicted that there will be a substantial increase in AM applications in the medical and dental fields in the near future [26].

2.4 Additive manufacturing methods

There are several different technologies that are used in additive manufacturing, also known as 3D printing. Within this section, we delve into several widely recognized additive manufacturing techniques that hold prominence within the industry. These technologies can be broadly classified into three main categories:

Application Market	Participation (%)
Industrial machinery	20.0
Aerospace sector	18.9
Automotive sector	16.0
Consumer products/electronics	11.7
Medical/Dental industry	11.3
Academic institutions	7.9
Government/Military	5.1
Architecture	1.9
Other	7.0

Table 2.1: Participation share of different industries in using parts manufactured through additive manufacturing (AM) technology in 2019 [26]

2.4.1 Liquid Based

Fused Deposition Modeling (FDM) is a method of additive manufacturing that builds three-dimensional objects through the layer-by-layer melting and extrusion of a thermoplastic filament. The procedure begins with slicing a 3D model into tiny layers, followed by the FDM 3D printer heating and melting the filament material, which is then deposited onto a build platform in a manner defined by the sliced layers. After a layer is finished, the printer moves up slightly and the procedure is repeated until the product is finished. Because of its inexpensive cost and ability to print in a wide range of thermoplastic materials, FDM is frequently used. While FDM offers design flexibility, it can present drawbacks such as limited material options, relatively lower part strength compared to some other methods, and visible layer lines on the surface that might require post-processing for improved aesthetics.

Stereolithography (SL) is an additive manufacturing technology that layers three-dimensional structures in a vat of liquid photopolymer resin using a UV laser. The procedure begins with the development of a 3D computer-aided design (CAD) model, which is subsequently sliced into various 2D cross-sectional layers. After pouring the resin into a vat, the UV laser is used to selectively cure the resin according to the pattern of each layer, hardening the resin and adhering it to the preceding layer. Once each layer is cured, the construction platform is lowered by one layer's height, and a new layer of resin is poured and cured. Layer by layer, this procedure is continued until the final 3D object is generated. Upon completion of the printing process, the object is extracted from the vat and undergoes a cleaning process to eliminate any residual uncured resin. Subsequently, the object is exposed to UV light to strengthen and optimize its properties.

While SL enables intricate details and smooth surface finishes, it has drawbacks including limited material choices compared to other methods, potentially brittle parts, and the need for

post-curing to achieve optimal material properties. Additionally, SL can be slower than some other rapid prototyping methods, and support structures might be necessary for overhanging features, affecting design complexity and post-processing.

Digital light processing (DLP) is an additive manufacturing technique in which liquid photopolymer resin is cured layer by layer by digital projectors. It begins with the creation of a 3D computer-aided design (CAD) model, which is then sliced into multiple cross-sectional layers in 2D.

Light is projected onto the resin surface by a digital light projector. The light cures each layer according to its pattern. This process is repeated layer by layer until the final object is created. Objects are removed from the vat after printing and cleaned to remove any uncured resin.

A key advantage of DLP over other additive manufacturing technologies is its ability to produce high-resolution objects with smooth surfaces faster. It is important to note, however, that the materials used in this process may have limitations in terms of strength and durability, and the layer-by-layer curing technique may leave the surface of the object stepped. DLP is widely used in manufacturing industries such as dental, jewelry, and toys.

Powder bed and inkjet head (PBIH) is a binder Jetting process that involves the layer-by-layer deposition of a powdered material using an inkjet printhead. Computer-aided design (CAD) models are first created, then sliced into layers of 2D cross-sections. On the build platform, the powdered material is spread evenly and a liquid binder is applied selectively by the inkjet printhead according to the layer pattern. The binder solidifies the powder and bonds it to the previous layer. In this process, layers are added one after another until the final object is formed.

In addition to producing complex geometries with high precision and accuracy, PBIH also has the capability to use a range of materials, such as metals, ceramics, and plastics. PBIH offers high-resolution printing and the potential for multi-material objects; however, challenges include potential material limitations, post-processing for strength due to binder use, and the need to manage powder removal and infiltration steps. In infiltration, a secondary material is introduced to enhance the part's properties or fill in voids, often through a liquid or molten phase. Additionally, complex geometries might require intricate support structures and the process can be slower for large-scale production.

2.4.2 Sheet Based

Laminated object manufacturing (LOM) is an additive manufacturing technology in which thin sheets of material are cut and bonded layer by layer to create 3D objects. Typically, LOM uses paper, plastic, or metal that is layered and adhered with a heated roller or laser cutter. It is repeated layer by layer until the final object is created, and the build platform moves down by the height of each layer.

Post-processing is conducted after printing to enhance the object's properties. Excess material is removed after printing. LOM produces large, low-cost objects quickly and accurately, with a high level of surface finish. Nevertheless, the objects produced may be weak and fragile, and the layering process may produce a stepped appearance on the surface of the objects. LOM is commonly used in the automotive, aerospace, and architectural industries, among others.

Ultrasonic consolidation (UC) is an additive manufacturing method that bonds layers of metal foils together to form a solid metal item using high-frequency ultrasonic vibrations. In this procedure, thin metal foils are placed on top of one another, then ultrasonic vibrations are applied to the stack, causing the metal to fuse together via solid-state welding.

The method may be used to manufacture totally dense metal components with complex geometries, and it's especially useful for creating parts out of incompatible metals or repairing damaged or worn-out sections. However this method can exhibit challenges such as limited material compatibility, anisotropic properties due to layer bonding, and a slower process speed compared to other methods, potentially impacting its suitability for specific applications.

2.4.3 Powder Based

Powder bed fusion (PBF) processes, like Binder Jetting processes, create 3D printed objects out of powder beds . However in PBF the powder particles are fused together using a selectively steered energy source.

Electron Beam Melting (EBM) involves utilizing an electron beam to selectively melt metal powder in a high vacuum environment. In this process the kinetic energy of electrons is converted into heat when they interact with the powder material.The beam is directed at a powder bed to fuse it layer by layer, creating a three-dimensional object. This process is typically used with high-temperature alloys like titanium.

EBM offers rapid production and can use various metals; however, drawbacks include potential residual stresses in parts, limitations in surface finish compared to other methods, and the need for support structures that can be difficult to remove. Additionally, EBM parts might exhibit anisotropic properties due to the layering process, and the specialized equipment can come with high initial costs.

Selective Laser Sintering (SLS) Selective Laser Sintering (SLS) is an additive manufacturing process that involves fusing powdered materials, typically polymers or metals, layer by layer using a high-powered laser. The laser selectively heats the powder to a point where particles reach a state just below melting, allowing them to fuse and create a solid structure. SLS offers design flexibility

and a wide range of material options, as well as the ability to produce complex geometries without the need for support structures. However, post-processing might be required to improve surface finish, and there can be challenges in achieving precise dimensions due to factors like shrinkage during sintering.

Selective Laser Melting (SLM) utilizes laser radiation to melt and fuse powder particles in an ambient environment of inert gases like Nitrogen or Argon. In the SLM process, the laser beam is absorbed by the material through either Fresnel absorption or plasma absorption.

This technology is commonly used to produce parts with intricate geometries and lattice structures that can't be made using traditional machining methods. It is widely applied in aerospace, automotive, and medical industries to manufacture high-strength, lightweight components.

In this research the additive manufacturing process of interest is as selective laser melting (SLM) also known as laser-based powder bed fusion , because it is the most common, widely applied, and possibly the most evolved metal additive manufacturing technology available [27, 28]. Therefore, the following sections of the introduction concern mainly this technology.

2.5 Selective Laser Melting Process

The process of SLM or EBM involves directing a focused laser beam or electron beam onto a bed of metal powder that is located within a manufacturing chamber. The chamber is filled with either inert gas such as Nitrogen or Argon or maintained in a vacuum in EBM systems. After melting the designated areas of the powder bed, a machine-integrated recoater or roller will automatically apply another thin layer of powder, usually with a thickness of 20-90 μm [29], onto the previous layer. Then, the building platform is lowered by the layer thickness, and the process is repeated.

To achieve adequate melting and ensure that the melt pool reaches the previously melted solid layer, the laser beam's energy density must be sufficiently high. While a portion of the beam reflects away from the powder bed, a significant amount of it is absorbed by the material, leading to melting. The powder absorbs the beam much more effectively on the powder bed than on a flat surface of solid metal, due to the beam's multiple reflections and the powder material's large specific surface area [31, 28]. As the beam moves across the powder bed during laser-based powder bed fusion, the molten material solidifies and rapidly cools due to the fast thermal cycle, resulting in a distinct microstructure that deviates significantly from those achieved through conventional manufacturing methods [31]. As a result, imperfections such as unwanted microstructures, residual stresses, and porosity can occur during the process [32]. These defects will be more thoroughly addressed in the following section.

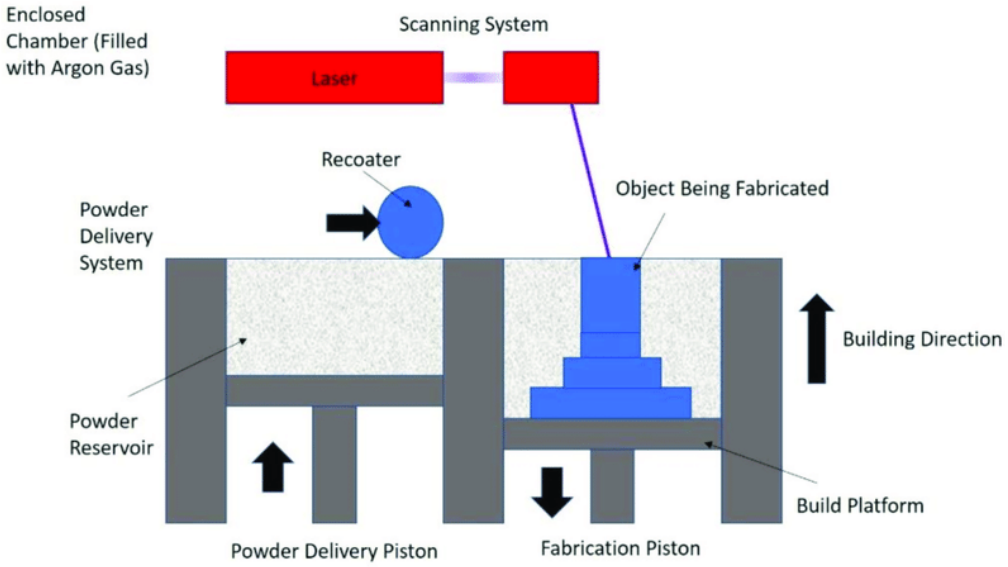

Figure 2.3: A schematic diagram of Selective Laser Melting (SLM) process [30]

The parts of the work-piece undergo cyclic temperature variations, with some regions contracting during cooling and others expanding during heating. These inherent variations induce residual stresses due to the ensuing thermal expansions and contractions, leading to bending and distortions in the part [32]. These residual stresses and undesired microstructures are among the issues that arise during the process, with the rapid cooling and unique microstructure being a hallmark of laser-based powder bed fusion.

2.6 Defects and mechanisms of formation

Understanding the formation of internal processing flaws, such as gas porosity and lack-of-fusion, in metal additive manufacturing (AM) is increasingly important as the technology becomes more widely used. These flaws, or material voids, are a major contributor to variability in mechanical properties of AM material and can significantly degrade fatigue and fracture behavior [33, 34, 35]. Material voids act as stress concentration sites and can lead to accelerated crack nucleation and propagation during cyclic loading. These defects limit the use of AM in fatigue-limited applications [33, 36, 37], whereas, static mechanical properties like yield strength are relatively resilient to the existence of material voids [35].

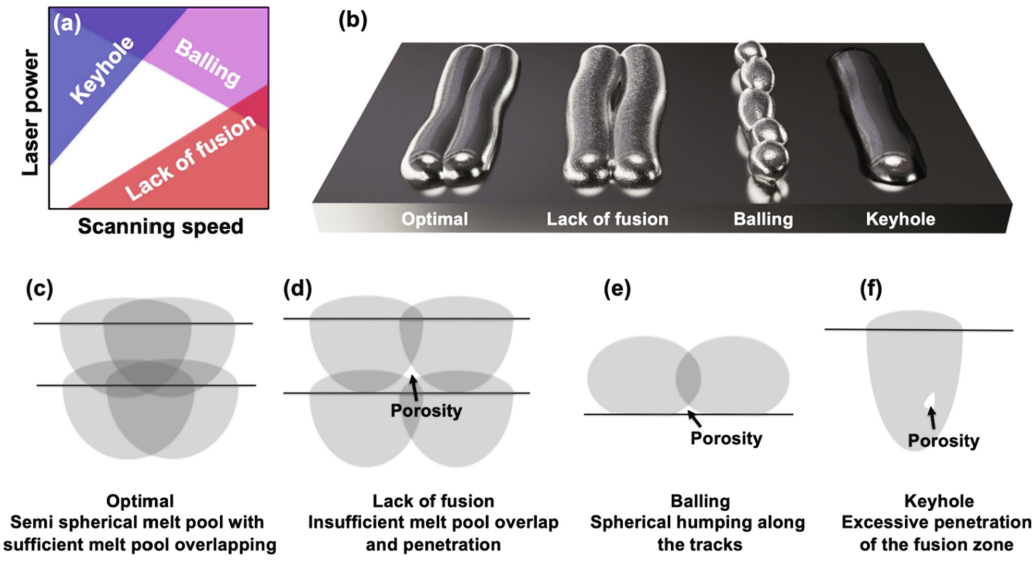

Figure 2.4: (a) PV processing map for the SLM process illustrating the regions associated with three porosity defects: keyhole, balling, and lack of fusion. (b) Simplified representation of melt pool tracks at different processing regimes of the PV maps, (c-f) Simplified cross-sections of melt pool tracks indicating the location of porosity defects [38].

Numerous studies have examined how process parameters affect the formation of defects. Important parameters include those related to the laser (such as power, spot size, pulse duration, and frequency), the scanning process (e.g., speed, spacing, rotation, and pattern), the powder used (including morphology, particle size, distribution, layer thickness, and material properties), and macroscopic factors (like powder bed temperature and uniformity, gas flow and type, and spreader bar type) [39].

High-speed x-ray visualization studies have demonstrated that the formation of vapor cavities, i.e. keyholes, is highly probable above a particular power density threshold, which results in unstable keyholes and the formation of keyhole porosity [40, 41, 42]. Increasing the scanning speed while maintaining constant laser power causes the keyhole to become shallower and more elongated [43]. Generally, an optimal process window that involves a combination of power, velocity, hatch spacing, and layer depth (P-V-H-L) exists for additive manufacturing such as the one shown in Figure 2.5. Apart from the P-V-H-L processing combination, the scan strategy also plays a critical part in the formation of defects in PBF processes. The scan strategy has an impact on heat transfer, powder melt formation, solidification rate, and grain morphology, which in turn affects the type, location, and distribution of defects. Therefore, optimizing process parameters, heat source power, and scan speed and strategy is crucial for reducing porosity caused by the process.

Numerous optimal process parameter maps [44, 32, 45] and scan strategies [46, 47, 48, 49] have been established, and in many cases part densities above 99.5 percent are reported. [50, 51].

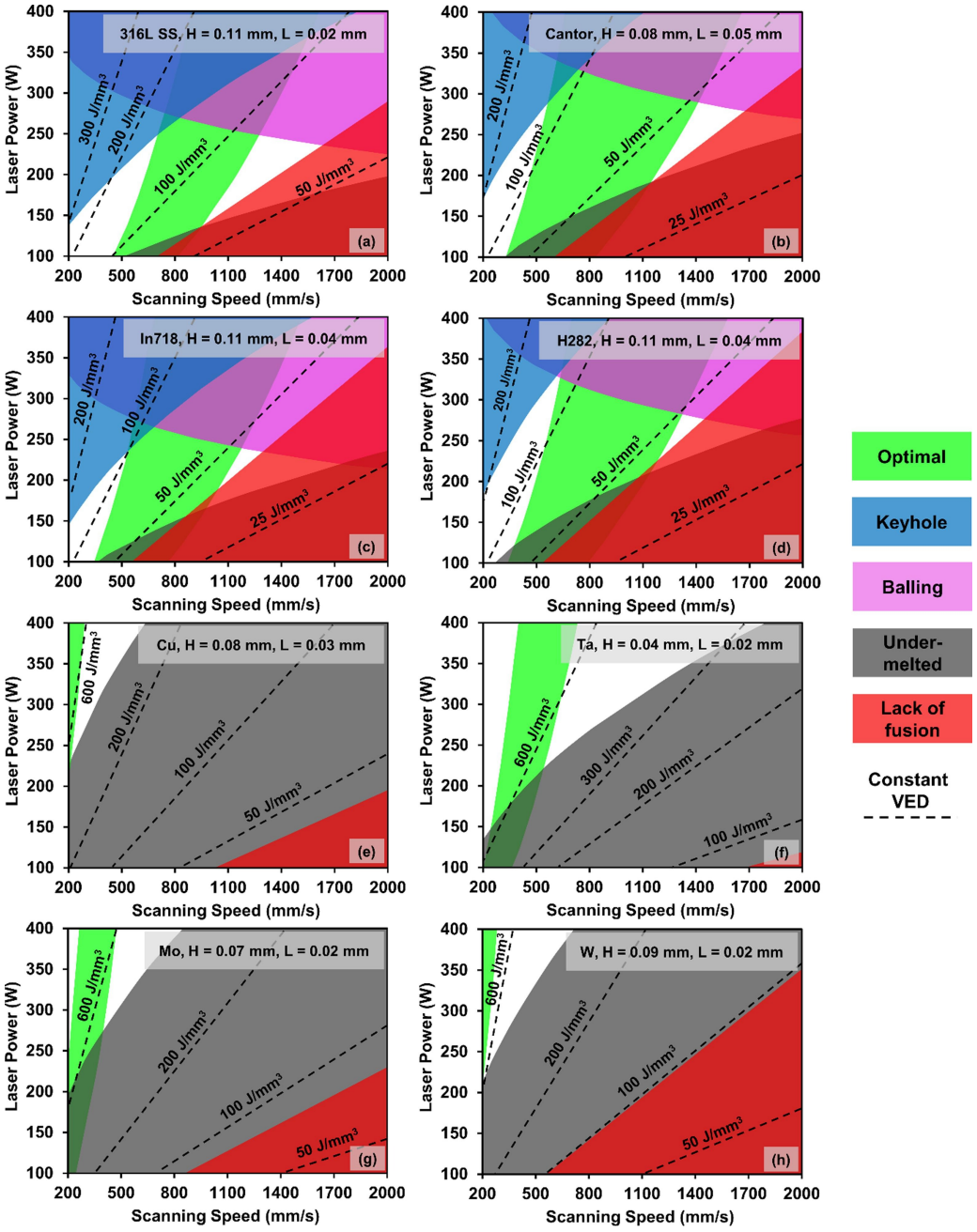

Figure 2.5: P-V-H-L (Power-Velocity- Hatch Spacing - Layer Depth) maps for (a) 316L stainless steel (b) Cantor alloy (c) Inconel 718 (d) Haynes 282 (e) Copper (f) Tantalum (g) Molybdenum, and (h) Tungsten generated using analytical models [38].

2.7 Review of Numerical Methodologies for PBF simulation

2.7.1 Finite Element Method (FEM)

FEM is mostly used to model thermomechanical behaviour during selective laser melting process. including thermal history, transient thermal stresses, residual stresses and distortions. When using FEM simulation, the user provides various inputs in the pre-processing stage, such as the shape of the object, the mesh, the starting and boundary conditions, the external forces, and the material characteristics. During processing, the system's partial differential equation is divided into individual equations for each element. These equations are then combined into a single global equation. After solving the equation, the post-processing stage can utilize the solution to display the temperature distribution on the part geometry. To estimate residual stresses and deformations, a mechanical analysis is conducted. The load applied is based on the temperature field resulting from the thermal analysis.

To assess thermal and residual stress states in parts produced through SLM using a mobile laser heat source, it is critical to understand the time-varying temperature profile [52]. Gusarov et al. [53] devised a model to determine the thermal conductivity of a powder bed based on molecular structure. They found that the conductivity is impacted by sintering effects that form and grow necks between particles, altering microstructure. In another study, Gusarov et al. [54] developed a finite element model to investigate how scanning velocity affects SLM of 316L stainless steel powder. They discovered that a specific range of scanning velocities produces uniform re-melted tracks. They determined through single-line scanning experiments that a specific scanning velocity range ensures uniform re-melted tracks, while deviations from this range lead to fractured tracks known as the balling effect. The argue that this effect, especially prominent at higher scanning velocities (typically above 20 cm/s), is associated with Plateau–Rayleigh capillary instability within the melt pool. Mashhood et al. [55, 56] proposed a numerical strategy to analyze the formation of deformations and stresses in metal additive manufacturing using FEM. They used a thermo-mechanical FEM model interfaced with AM G-code translated data to evaluate thermal deformation and residual stress in AM parts. They demonstrated how thermal conduction, convection, and radiation drive the AM process by thermally loading the deposited material.

Considering multiple layers in SLM is important because the temperature differences between the layers can have an impact on thermal distortion and residual stresses. For instance, during the solidification of liquid metal, the top layer contracts at a faster rate than the underlying layers, which can result in tensile stresses in the top layer and compressive stresses in the lower layers due to geometric constraints. Roberts et al. [52] created a finite element model to predict the

time-varying temperature field for multiple layers of Ti-6Al-4V titanium alloy powder parts. They used the element birth and death method, an inventive simulation technique, to imitate the intricacy generated by the addition of numerous powder layers. Huang and Zhang [57] used an FEM model to study transient high temperature and the complex temperature distribution in selective laser melting. Their simulation demonstrated that as the number of layers increased, the maximum temperature, heat-affected zone (HAZ), and dimensions of the molten pool also increased. However, with the exception of the first layer, the cooling rate decreased as more layers were added.

To forecast the dimensions and traits of the melt pool, it is crucial to have a precise temperature distribution. In one FEM study, Aggarangsi and Beuth [58] examined the size of the melt pool near a free edge in laser-based deposition and their findings using Rosenthal's solution. Jahn et al. [59] utilized a FEM model that accounted for heat conduction, a free melt surface, a moving phase boundary, and the Navier-Stokes equations to calculate the geometry of the melt pool during solid-liquid-solid phase transitions.

2.7.2 Finite Volume Method (FVM)

FVM, like FEM, discretizes the model domain into small elements or control volumes, and solves the physics equations in linearized forms before assembly. However FVM is known be overall faster and simpler to implement new physics [4].

In early attempts to use FVM for SLM simulation, the powder bed was treated as a continuous medium. Jamshidinia et al. [60, 61] developed a CFD model in Ansys Fluent© with a continuous powder bed to simulate the EBM process. The authors conducted a thermal analysis of the melt pool, both with and without consideration of fluid flow. Their findings indicate that the outward flow resulting from surface tension has a significant effect on the melt pool geometry when fluid flow is taken into account. Manvatkar et al. [62] used FVM to develop a melt pool model with continuous powder bed and used it to simulate a multi-layer SLM process. The model is comparatively simple, not considering free surface movements of the melt. They have used the cooling rates and solidification parameters to estimate the microstructure cell spacing and hardness in various layers.

Advancements in computational power and numerical methods have made it possible to simulate the complex powder bed behavior in detail, allowing for more accurate and comprehensive simulations of the SLM process. Megahed et al. [63, 64, 65] utilized the FVM software developed by ESI group (ESI ACE+) to conduct a simulation of the melting of powder layers and consolidation of melt pools. The software uses the discrete orientation method to model the laser heat source in the discrete particles, and incorporated the Discrete Element Method (DEM) to create powder beds with predetermined characteristics. Researchers at Lawrence Livermore National Laboratory (LNLL) used an in-house Three-Dimensional Finite Volume Arbitrary Lagrangian-Eulerian simulation code (ALE3D) [66, 67, 68, 69] to analyze the effects of process parameters on melt pool dynamics. They

have provided a rather complete modeling framework, except for excluding the mushy zone. They also have not modeled the powder spreading process, instead a rainfall model is used to generate the powder bed. Gürtler et al. [70, 71] have used an in-house OpenFOAM solver that incorporates VOF method to capture the liquid interface with gas. In their simulation they have produced a regular lattice of spherical powders as the powder bed and added that on top of the substrate geometry. Panwisawas et al. [72, 73, 74] from University of Birmingham also used a rainfall simulation to create the powder bed. They used OpenFOAM to develop a CFD model that incorporates all the physics involved including a simplified version of evaporation. They have used their model to investigate melt pool dynamics, keyhole formation, porosity and microstructure growth. Lee et al. [75, 76] used Flow-3D commercial software to model an laser melting of a Inconel 718 (IN718) powder bed and free movements of the melt pool. They extracted the solidification parameters , i.e., temperature gradient and solidification rate to study the resulting microstructure.

2.7.3 Lattice Boltzmann Method (LBM)

The Lattice Boltzmann Method (LBM), which is another method that has found application in powder bed fusion simulations, is a computational fluid dynamics (CFD) technique that is well-suited for problems featuring complex interfaces. LBM works by creating fictive fluid particles at a lattice of locations and tracking their collisions and movement to simulate realistic fluid behavior, rather than solving the Navier-Stokes equations directly. Researchers have used LBM to investigate the melting and solidification of powder beds in powder bed fusion processes, such as Selective Laser Melting (SLM) and Electron Beam Melting (EBM). Körner group at the University of Erlangen-Nuremberg [77, 78], developed a 2D LBM model to simulate the SLM process and investigated process defects like balling and discontinuous tracks. They have have a focus on EBM process and mostly use Ti6Al4V alloy for their simulations and experiments. Ammer et al. [79, 80] used a 3D thermal lattice Boltzmann method to simulate the EBM process, accounting for various physical and thermal effects. They developed an improved model that accurately captured the complex interactions between the different phases, including evaporation and backlash effects. Klassen et al. [81] used the LBM model to investigate hydrodynamics, thermodynamics, and multi-component evaporation to study the relationship between input energy, evaporation, and alloy element distribution in the EBM process for a Ti6Al4V alloy.

2.7.4 Smoothed Particle Hydrodynamics (SPH)

Another modeling and simulation approach for the selective laser melting (SLM) process involves the implementation of the meshless method of Smoothed Particle Hydrodynamics(SPH). SPH represents the domain as a set of particles, each with their own unique material properties, that move

in accordance with the conservation equations [2]. In summary, the SPH method is well-suited to model complex flows that involve free surfaces, large deformations, moving interfaces, and material splitting [82]. Shah and Volkov [83] made one of the earliest attempts to use SPH for simulating SLM. They developed a numerical method to model heat transfer in a two-dimensional powder bed system and utilized a bimodal powder distribution to investigate the impact of powder bed properties, such as powder distribution and packing density, on the effective thermal conductivity of the powder bed. Russell et al. [84] used SPH to simulate laser-based additive manufacturing processes, such as SLM. The model included Navier-Stokes equations, surface tension, and Marangoni convection, along with temperature-dependent material properties. A Gaussian 3D volumetric heat source was used, with power density defined by the Beer-Lambert law. The physics equations were similar to FEM, but the numerical implementation differed. The simulation output included temperature profiles, velocity and surface tension fields, and material states (solid, liquid, in-between). Bierwisch [85] presented a coupled model that combines SPH with Discrete Element Method (DEM). The DEM model is used to simulate the behavior of individual particles during powder spreading, while the SPH component is employed to model the fluid dynamics of the melt pool.

2.7.5 Discrete Element Method (DEM)

In SLM simulation, DEM models [86] are often used to simulate the behavior of the powder bed during raking and spreading [72, 74, 63, 87]. Le et. al [88] used a 3D CFD-DEM coupled model to analyze powder entrainment and denudation effects. The two models were coupled by exchanging energy and momentum, and the effect of vapor jet on denudation width was analyzed. However, the model does not consider the melting of particles, but instead includes a pre-defined moving melt pool. Yu and Zhao [89] have used a fully resolved coupled CFD-DEM model utilizing the Immersed Boundary (IB) method to resolve the velocity and pressure fields of the molten flow and powder grains' motion. The thermal field, including both fluid and solid grains, is solved using a two-phase CFD approach for the entire domain. Estupinan et al. [90] proposed a combined model that integrates their proprietary discrete element method (DEM) model, XDEM, with a computational fluid dynamics (CFD) model to consider the interaction of heat, mass, and momentum between the system and its environment. The model connects the discrete approach with the continuous one, which solves for the surrounding fluid phases. As explained in previous chapter, the present study develops a fully-coupled CFD-XDEM model where thermodynamics and dynamics of the particles are both considered and coupled with the CFD model.

Chapter 3

A CFD-DEM Coupled OpenFOAM Solver for Multiphysics Simulation of Additive Process: Development and Validation[1]

3.1 Abstract

Powder-based additive manufacturing technologies, specifically selective laser melting, are challenging to model due to the complex, interrelated physical phenomena present across multiple spatial scales during the process. A key element of such models will be the detailed simulation of flow and heat transfer in the melt pool that is formed when the powder particles melt. Due to the high temperature gradients that are generated inside the melt pool, the Marangoni force plays a key role in governing the flows inside the melt pool and determining its shape and dimensions. Conversely, mass and heat transfer between the melt and the powder significantly contribute to shaping the melt pool at the edges. In this study, we modified the OpenFOAM solver , icoReactingMultiphaseInterFoam, to be coupled to eXtended Discrete Element Method (XDEM) which models the dynamics and thermodynamics of the particles. By adding the Marangoni force to the momentum equation and also defining a laser model as a boundary condition for liquid-gas interface, the solver is capable of modeling the selective laser melting process from the moment of particle melting to the completion

[1]This chapter is written based on the following published paper: Navid Aminnia, Alvaro Antonio Estupinan Donoso, and Bernhard Peters. "Developing a DEM-Coupled OpenFOAM solver for multiphysics simulation of additive manufacturing process." Proceedings of ECCOMAS Congress 2022.

of the solidified track. The coupled solver was validated with an ice packed bed melting case and was used to simulate a multi-track selective laser melting process.

3.2 Introduction

In recent years, powder bed fusion technology has become more popular, leading to a variety of modeling approaches [91]. At the macroscopic scale, multiphysics models have been developed to study melting and solidification phenomena caused by a moving heat source above a powder bed [66]. Several studies have shown that the fluid flow within the melt pool, particularly Marangoni convection and recoil pressure, can lead to the development of critical defects such as porosity, spattering, denudation, and balling [66]. These studies mainly differ in the numerical methods they have used and the details of the physics incorporated into their models [4]. Some authors have implemented models such as Marangoni convection, recoil pressure [92] or evaporative [66] and convective cooling [93] of the melt pool while others may have excluded some of them.

An important part of the AM process involves the absorption of heat from the laser or electron beam and the distribution of this heat in the powder bed. Treatment of laser radiation and heat conduction in the powder is connected to the treatment of the powder bed[4]. Many studies consider the powder bed as a continuum [60, 61]. The continuum models have commonly considered laser as a spatially-varying heat flux with a Gaussian distribution. In these studies, laser heat profile is either constant in depth-direction or varies based on a correlation [94]. In continuum models, thermal conductivity is considered an effective value for the whole powder bed. For instance, Gustarov et. al [95] considered the effective thermal as a fixed small value below melting temperature and a greater value for the melt. However recently, there has been a shift towards using discrete powder bed models. Ganeriwala and Zohdi [96] used a Discrete Element Method (DEM) to model the powder bed and a finite difference method for the substrate. They considered a gaussian distribution for the laser with exponentially decaying radiation in the depth. In these models, the gas is not considered a second phase, therefore, only the contact point heat conduction is accounted for[4].

In the present work, a CFD-DEM coupled model is developed and validated for the simulation of the selective laser melting process. The CFD model is based on the VOF method and considers the gas phase between the particles and calculates its heat transfer with the powder bed. The DEM model simulates a discrete powder bed with particles subjected to convective, conductive, and radiative heat transfer.

3.3 Methodology

3.3.1 Discrete element method

The particles are treated as a discrete solid phase in an in-house DEM code known as the eXtended Discrete Element Method (XDEM [97]). XDEM predicts both dynamics and thermodynamic states of the particular system. The dynamic module calculates the particle position, velocity, and acceleration whereas the temperature, melting rate, and shrinkage of the particle is calculated within the conversion module.

3.3.1.1 Dynamic module

The discrete element method used in the dynamic module is based on the soft-sphere contact model where the particles are assumed deformable and may overlap. The magnitude of this overlap depends on the contact force calculated by the force-displacement law. The particle hardness is described by Young's modulus, and the particle kinetic energy dissipation is characterized by a dampener and/or a dashpot. Detailed descriptions of these calculations and the equations below, can be found in a previous work [98]. The translational and rotational movements of the particles are described by Newton's second law of motion and Euler's rotation equation:

$$m_i \frac{d\vec{v_i}}{dt} = m_i \frac{d^2\vec{X_i}}{dt^2} = \vec{F_i^c} + \vec{F_i^g} + \vec{F_i^{ext}} \tag{3.3.1}$$

$$I_i \frac{d\vec{\omega_i}}{dt} = \sum_{j=1}^{n} \vec{M_{i,j}} \tag{3.3.2}$$

The contact force $\vec{F_i^c}$ is the summation of all normal $\vec{F_{i,j}^{c,n}}$ and tangential $\vec{F_{i,j}^{c,t}}$ forces that are exerted by other particles when they collide. $\vec{F_i^g}$ is the gravitational force. $\vec{F_i^{ext}}$ is the summation of all external forces acting on the particle, including the drag force F_d and the buoyancy force F_B from the ambient fluid.

3.3.1.2 Conversion module

Conversion module solves the momentum, mass, energy (and species) conservation equation within the particles which are radially discretized. Mass conservation equation is solved for the fluid that is present within the particle pores:

$$\frac{\partial}{\partial t}\left(\epsilon_f \rho_f\right) + \vec{\nabla} \cdot \left(\epsilon_f \rho_f \vec{v_f}\right) = \dot{m}_{s,f} \tag{3.3.3}$$

A One-dimensional transient energy equation is solved for all the particles:

$$\frac{\partial \rho c_p T}{\partial t} = \frac{1}{r_n}\frac{\partial}{\partial r}\left(r^n \lambda_{eff}\frac{\partial T}{\partial r}\right) - r^n\left(\vec{v}\rho_f c_{p_f} T\right) + \sum_{k=1}^{l}\dot{\omega}_k H_k \tag{3.3.4}$$

These governing equation are subjected to the following boundary conditions:

$$-\lambda_{eff}\frac{\partial T}{\partial r}\bigg|_{r=0} = 0 \tag{3.3.5}$$

$$-\lambda_{eff}\frac{\partial T}{\partial r}\bigg|_{r=R} = \alpha(T_R - T_\infty) + q''_{rad} + q''_{cond} + q''_{laser} \tag{3.3.6}$$

$$-D_{i,eff}\frac{\partial \rho_i}{\partial r}\bigg|_{r=R} = \beta_i\left(\rho_{i,R} - \rho_{i,\infty}\right) \tag{3.3.7}$$

q''_{laser} is surface heat flux coming from the laser. The formulation is consistent with the laser formulation of the CFD model presented in equation 3.3.18, other than it also considers a heat profile in depth direction according to [96]. The aforementioned equations and the conversion model are described in detail in [99, 98].

The melting process involves interfacial mass transfer from the solid phase to the liquid phase. The rate of this transfer is denoted as melting rate $\dot{m}$ and can be calculated based on the energy balance relation. The melting rate is defined by the ratio of the available enthalpy above melting temperature to the latent enthalpy required for melting L_f:

$$\dot{m}_{s,f} = \begin{cases} \frac{(h-h_m)}{L_f \Delta t} & h \geq h_m \\ 0 & h < h_m \end{cases} \tag{3.3.8}$$

The melting rate ($\dot{m}_{s,f}$) is transferred to the CFD field by introducing a source term in the fluid continuity equation Eq 3.3.10.

3.3.2 Computational fluid dynamics

The motion of fluid is calculated using Volume Of Fluid (VOF) method where the continuity, momentum and energy equations are solved for two or more immiscible phases. Consequently, the resulting velocity ($\vec{v_f}$) , density (ρ) and temperature (T) are weight-averaged among all fluid phases based on the volume fraction (γ) of the phase:

Volume of fluid equation:

$$\frac{\partial \gamma}{\partial t} + \vec{\nabla}.(\gamma U) = 0 \tag{3.3.9}$$

Conservation of mass:

$$\frac{\partial}{\partial t}\left(\rho_f\right) + \vec{\nabla}\cdot\left(\rho_f \vec{v_f}\right) = \dot{m}_{s,f} \tag{3.3.10}$$

The subscript f designates the specific property of the fluid mixture. for instance, ρ_f is the density of the fluid mixture. $\dot{m}_{s,f}$ is the mass source due to the phase change of solid particles to the fluid mixture.

Conservation of momentum:

$$\frac{\partial}{\partial t}\left(\rho_f \vec{v}_f\right) + \nabla \cdot \left(\rho_f \vec{v}_f \vec{v}_f\right) = -\nabla p + \mu \nabla^2 \vec{v}_f + S_U + S_p + F_s \tag{3.3.11}$$

$$S_U = \rho \vec{g} \beta (T - Tref) - \frac{C(1-\gamma_l)}{{\gamma_l}^3 + e_0} \vec{v_f} \tag{3.3.12}$$

p, μ denote respectively the pressure field and viscosity. S_U expresses the momentum sources defined in the model. The first term (thermal buoyancy) uses the concept of Boussinesq approximation where $\vec{g}$ is the gravitational acceleration constant and β the thermal expansion coefficient. The second term (momentum sink) expresses the momentum in the mushy zone and is the function of liquid volume fraction γ_l, which represents complete liquid for $\gamma_l = 1$ and complete solid for $\gamma_l = 0$. C is a constant that is chosen to be large enough (10^8) to create a large momentum sink in solid. While e_0 is a small constant (10^{-3}) to avoid division by zero. This term acts as a large momentum sink in the solid region while in the liquid region it vanishes.

$$S_p = \rho_f \vec{A_c} - \rho_f \Omega_c \vec{v}_{f_c} \tag{3.3.13}$$

S_p denotes the source terms introduced from the particle. $\vec{A_c}$ (m/s^2) and Ω $(1/s)$ are the linear and angular acceleration exerted by the particles on the considered control volume.

$\vec{F_s}$ is the volumetric smeared surface force based on Continum Surface Force (CSF) method [100], that is applied on gas-liquid interface:

$$\vec{F_s} = \left[\sigma \kappa \vec{n} + \frac{d\sigma}{dT}(\nabla T - \vec{n}(\vec{n}.\vec{\nabla} T))\right] |\nabla \gamma| \frac{2\rho}{\rho_1 + \rho_2} \tag{3.3.14}$$

The equation is composed of a normal and a tangential component. The tangential component is created due to a high surface tension gradient on the gas-liquid interface. In the applications such as laser welding and additive manufacture where the surface of the melt may experience a high temperature gradient, this component can become the dominant term in the momentum equation. The term $(\nabla T - \vec{n}(\vec{n}.\vec{\nabla} T))$ gives the tangentional component of the temperature gradient. In this equation, σ is surface tension coefficient, κ is the curvature, $\vec{n}$ the surface normal vector. $|\nabla \gamma|$ is the gradient of volume fraction and serves as the Brackbill delta function and the term $\frac{2\rho}{\rho_1+\rho_2}$ plays a role in redistributing the forces toward the heavier phase (the liquid) so that high accelerations in air-filled cells are avoided [100] .

Conservation of energy:

$$\frac{\partial}{\partial t}\left(\rho_f c_{p_f} T\right) + \nabla \cdot \left(\rho_f c_{p_f} \vec{v}_f T\right) = \nabla \cdot \left(\lambda_f \nabla T_f\right) + S_p + S_{laser} \tag{3.3.15}$$

c_{p_f} and λ_f are the average specific heat and thermal conductivity of the fluid mixture. These physical properties along with the density are calculated as volume-weighted averages of the phases present in the control volume under consideration. S_p is the heat source introduced by the particle (XDEM) and includes the thermal convection and mass flux energy of the melt (the enthalpy that is being introduced along with $\dot{m}_{s,f}$ in Eq 3.3.8. S_{laser} is the heat source from the laser. A formulation of the CSF method [100] was used here to define the surface heat flux of the laser as a volumetric heat source on the gas-liquid interface.

$$S_{laser} = Q_{laser} \frac{\rho c_p}{\rho_1 c_{p_1} + \rho_2 c_{p_2}} \tag{3.3.16}$$

$$Q_{laser(W/m^3)} = q''_{laser(W/m^2)} \, |\nabla \gamma| \tag{3.3.17}$$

$$q_{laser} = \frac{2\eta P_{laser}}{\pi R^2} exp\left(-2\frac{(x - x_0 - \nu t)^2 + (y - y_0)^2}{R^2}\right) \tag{3.3.18}$$

Eq 3.3.16 redistributes the heat source over the phase with higher ρc_p, which is liquid at the gas-liquid interface. Eq 3.3.17 shows the adaptation of the CSF method to define the laser as a volumetric surface heat source based on the idea proposed by [101]. In Eq , η is absorption cofficient which is considered as constant. P_{laser} is the laser power and R is the laser beam radius. x_0 and y_0 are the starting coordinates of the laser beam and ν is the laser beam velocity.

3.3.3 Numerical Implementation

The CFD-DEM coupling is achieved through a conventional staggered approach. The CFD model was developed using the OpenFOAM library and is based on `icoReactingMultiphaseInterFoam` solver. The XDEM and OpenFOAM libraries are linked together and run via a single executable. The simulation starts after running the executable. First, the XDEM is initialized and the boundary conditions of the particles are defined. A volume fraction field for the particle phase is calculated by XDEM based on the location of the particle and the mesh structure of the CFD case. The particle phase would not enter the CFD conservation equations though. This information is only used for solid-to-liquid mass transfer.

At the beginning of each iteration, XDEM calculations are performed. Based on the calculations in XDEM, heat, mass and momentum sources are written as OpenFOAM fields. The OpenFOAM simulation starts its iterations considering the source terms. Heat and momentum sources are read via the `fvOptions` dictionary. However, mass source is defined as a `massTransferModel` for solid (particle phase) to liquid. The fluid governing equations are solved in the OpenFOAM solver and the new velocity, pressure, temperature, density, specific heat, and viscosity fields are calculated.

Then the simulation moves to the next time step and these updated fields are read by XDEM and used to calculate the new boundary conditions of the particles.

3.4 Results and Validations

This research was comprised of two main parts. In the first part, the CFD model capable of considering all the dominant transport phenomena that are at play in a selective laser melting process was developed. The second part was to develop a coupling of the CFD solver with XDEM which is responsible for modeling the dynamics and the thermodynamics of the powder particles in the aforementioned additive manufacturing process.

3.4.1 Continuum modeling Validation

The CFD model was developed based on an OpenFOAM ESI solver and after modifications and new implementations was named as `marangoniIcoReactingMultiphaseInterfoam`. As described in section 3.3.2 this model solves for N incompressible, non-isothermal immiscible fluids with phase change using a VOF method. This model can consider the Marangoni convection and laser heat source on the surface of liquids and solids. Therefore, in the first step, the model is validated by simulating a laser spot welding experiment by He et al. [102].

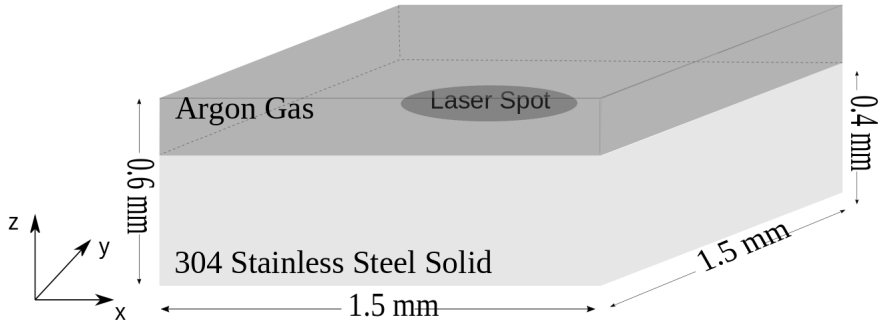

Figure 3.1: Illustration of the simulation domain. A stainless steel block and argon as shielding gas

3.4.1.1 Laser spot welding simulation

The laser welding process has many mutual physical phenomena with selective laser melting. A melt pool is created due to laser radiation on a solid surface and interacts with the laser. The Marangoni convection is a dominant force in generating a circulatory flow inside the melt pool which decides its shape and dimensions.

The physical properties that are used in the model are adapted from the values reported by He et al. [102]. A schematic of the laser welding specimen which is also the geometry for the

simulation is presented in figure 3.1. In the simulation, a $1.5mm \times 1.5mm \times 0.4mm$ stainless steel block with Argon gas on top, is exposed to laser radiation for 3ms. Due to high temperatures (e.g. about 3000K) at the laser incident point, the surface of the melt experiences strong surface tension gradients. This results in the generation of a circulatory flow inside the melt pool. Figure 3.2 shows the evolution of the melt pool over time. The isoline of $1697K$ (melting temperature) indicates the melt pool boundary. Inside the melt pool, the velocity vectors are shown. As time passes and more heat from laser radiation is accumulated on the melt surface, the temperature difference from the laser incident point to the edges of the melt pool increases. It can be observed that the ratio of this temperature difference at two consecutive time steps is greater than the ratio of the melt pool widths. This means an increase in temperature gradient on the melt surface which in turn means a stronger Marangoni convection. Therefore as time passes by, stronger Marangoni flow is observed which is characterized by larger velocity vectors and circulatory flows. The right-hand side ciculatory flow is clearly distinguishable in the melt pool of the time t = 3 ms. The flow on the surface is directed from the region with low surface tension (high temperature) to the region with high surface tension. Therefore on the right-hand side of the melt pool the circulatory flow is clockwise while on the left-hand it is anti-clockwise.

The simulation results are compared with previous studies and the experiment results are in table 3.1. The dimensions of the melt pool are commonly used as the criteria for validating the result because they are directly affected by the magnitude of the temperature gradients and Marangoni force.

Research	Scope	Half Width (mm)	Depth (mm)
He et. al [102]	Experiment	0.47	0.26
Tan et. al [103]	Simulation	0.44	0.25
This Research	Simulation	0.44	0.25

Table 3.1: Melt pool dimensions in a spot laser welding experiment. Comparison between experiment[102] and the simulation of this research

3.4.2 CFD-DEM Coupling Validation

3.4.2.1 One sphere of ice in a tank of water

Shukla et. al [104] set up a cold model experiment using ice and water to study the melting of steel straps in the high-temperature liquid iron melt. This study gives an insight into the convection melting of solid inside a pool of liquid. We have recreated this physical setup to validate the convective heat transfer and melt mass transfer in the CFD-DEM coupling which is designed for the simulation of additive manufacturing processes.

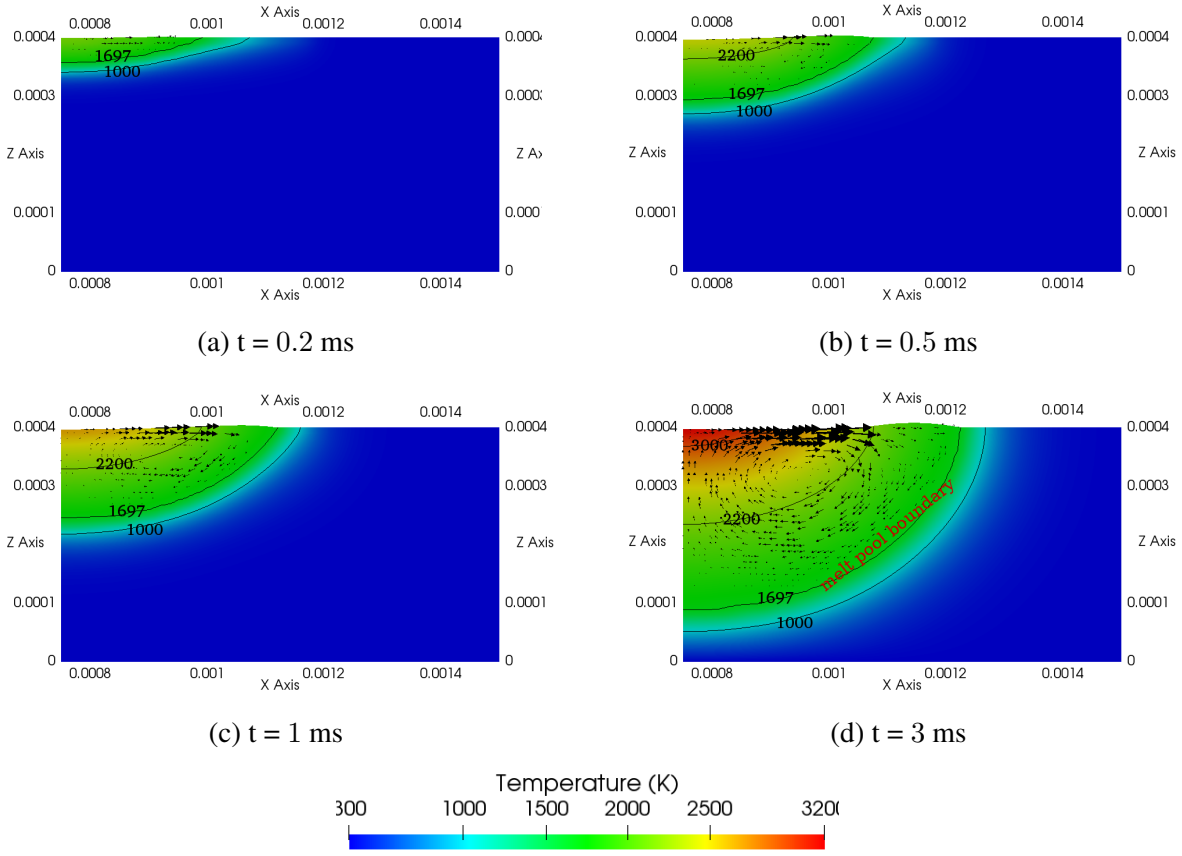

(a) t = 0.2 ms

(b) t = 0.5 ms

(c) t = 1 ms

(d) t = 3 ms

Figure 3.2: Evolution of melt pool over time. Figures show the right half of an XZ cross section of the steel block at Y = 0.75 mm which coincides with the laser incident point

In the original experiment, to study natural convection, a bulk of ice in the shape of a sphere was left floating in a tank of water at $20°C$ and the variations of the radius over time were recorded. In other experiments, they also added a gas inflow to observe the effects of forced convection. However we did not perform simulation on those experiments because they are out of the scope of our interest. Figure 3.3 (a) shows the experimental setup and figure (b) shows the simulation domain that was created based on that setup.

Figure 3.4 compares the experiment's reported ice radius over time to the simulation results. The ice radius over time characterizes the melting rate of the particle which is dominantly affected by the heat transfer of the particle. The objective of this simulation was to validate the melting model and convective heat transfer between XDEM and the CFD model.

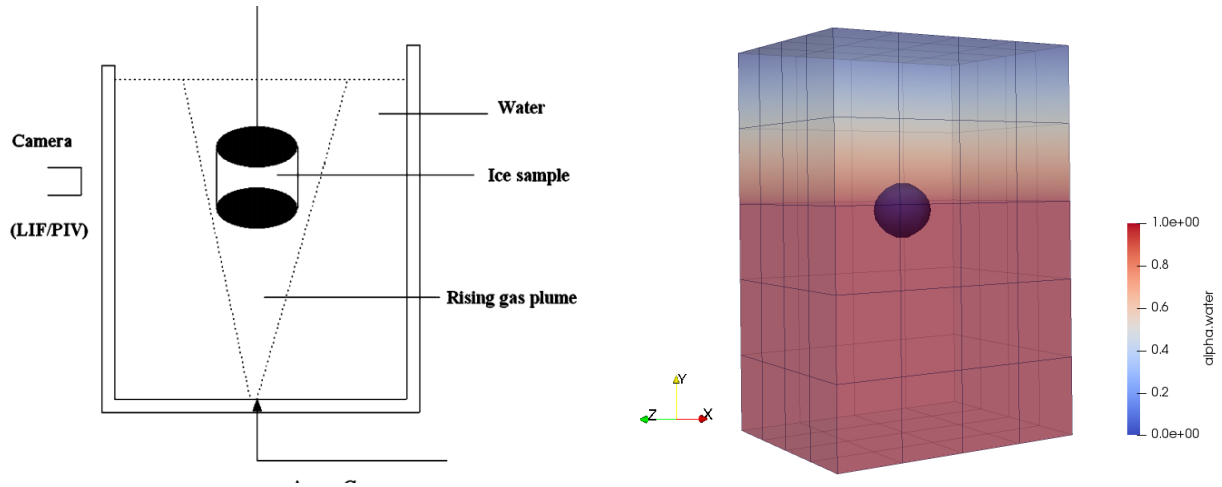

Expeimental setup [104] Simualtion setup

Figure 3.3: A schematic of the experimental setup used by Shukla et. al (left) and the simulation setup in OpenFoam (right) nearly two-thirds of the tank is filled with water and the rest with gas

3.4.2.2 Packed bed of ice in flowing water

The second validation case is based on an experiment performed by Hao and Tao [105] to study the convective melting of a granular packed bed of ice in flowing water. The objective here is to validate the heat, mass, and momentum source transfer between XDEM and the CFD model. To obtain this goal, the model is anticipated to predict the movements of the packed bed, and shrinkage in the size of the bulk of particles.

In the experiment carried out by Hao, the packed bed was placed in a water channel but restrained by two perforated plates. In our simulation, the plates are modeled as walls on the two sides of the packed bed. They repeat the experiment for three different inlet velocities and for each case, the total mass of the packed bed is calculated based on the water level rise in the channel. As can be seen in figure 3.5 a camera is installed, pointing at the ice packed bed to record the movements of the ice particles. We have used the mass variation report and camera images as the basis for our validation.

The results of the validation are shown in figure 3.6. It can be observed that for the three different velocities the degree of agreement between the simulation and experiment are different. This is because the parameters used for the heat transfer laws are sensitive to the fluid velocity. Therefore for each simulation setup, heat transfer parameters should be set based on the physical process at hand. Whereas in this simulation for the sake of comparison all the cases use Yang heat transfer law [106] to estimate the convective heat transfer between the particles and the surrounding water.

Figure 3.7 shows the evolution of the ice packed bed with time. Figures 3.7 (a) and (c) show the photos taken by the camera in the experimental setup and figures (b) and (d) show the result of the simulation. The water flow pushes the ice particles towards the right perforated plane. With time,

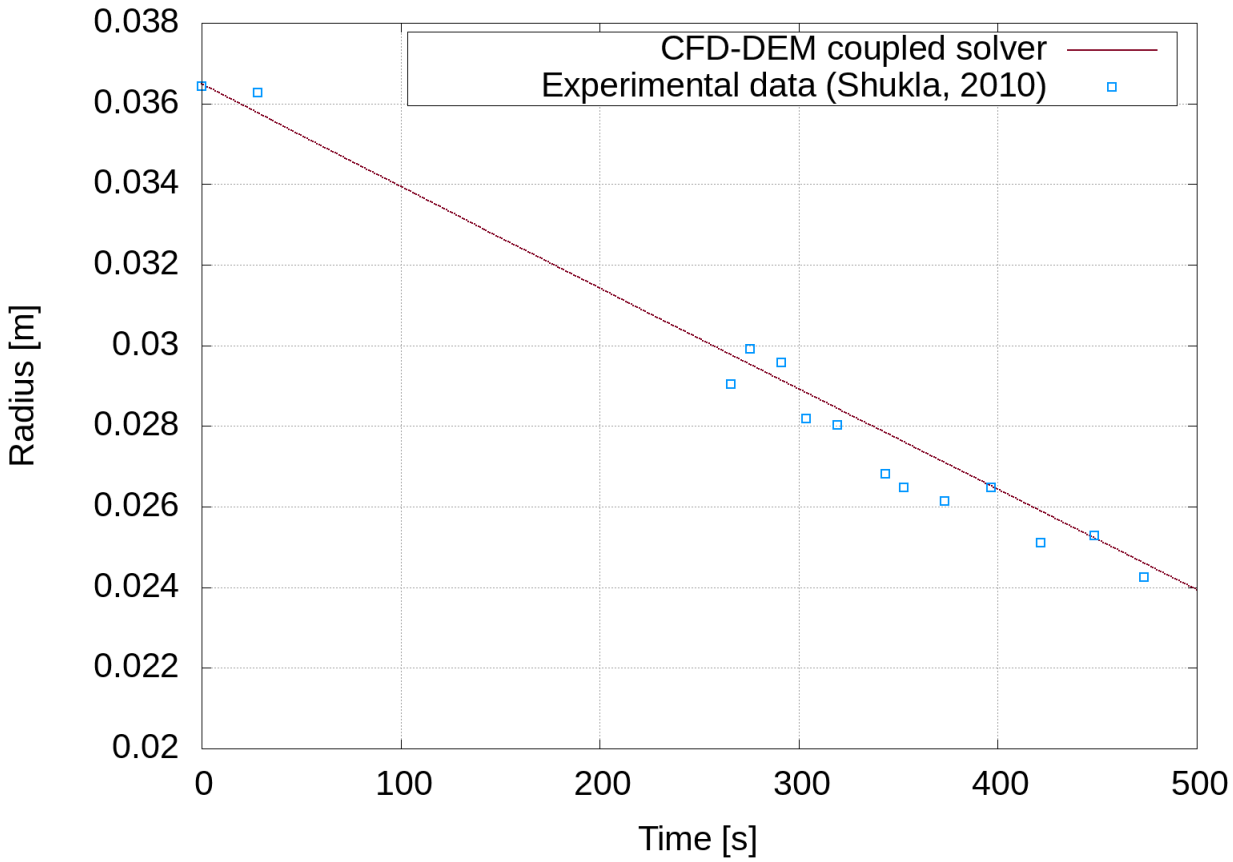

Figure 3.4: Variation of one spherical ice particle's radius in a water tank. Comparison between experiment [104] and simulation

the particles, are subjected to warm water, melt and shrink. We can see the exact same behaviour from the simulated packed bed (Figure 3.7).

3.5 Discussions

The objective of this research is to develop a CFD-DEM coupled model that includes the required features for a selective laser melting model. The focus of this article is the development and the validation of the model. Therefore the different milestones were defined for incremental development of the model. The first milestone was developing a suitable CFD model and it was carried out in the form of a new OpenFOAM solver. The next one was to couple the developed CFD solver to XDEM. The main challenge in this part of the research was to ensure that transfer and implementation of the source terms between XDEM and OpenFOAM were done properly. Therefore this article is mainly devoted to the development, method description, and the results of the validations. In future works, the CFD-DEM coupling will be applied to a selective laser melting process to predict the melt pool

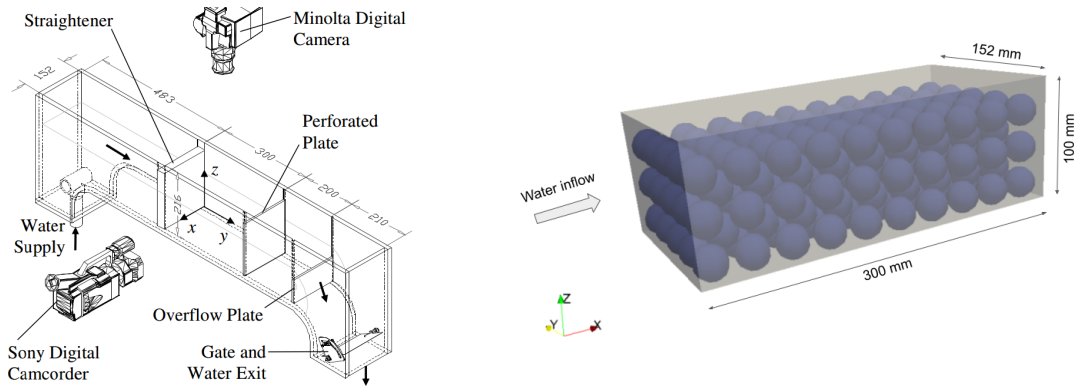

(a) Experimental setup [105] (b) Simulation setup

Figure 3.5: A schematic of the experimental setup used by Hao (left) and our simulation setup (right)

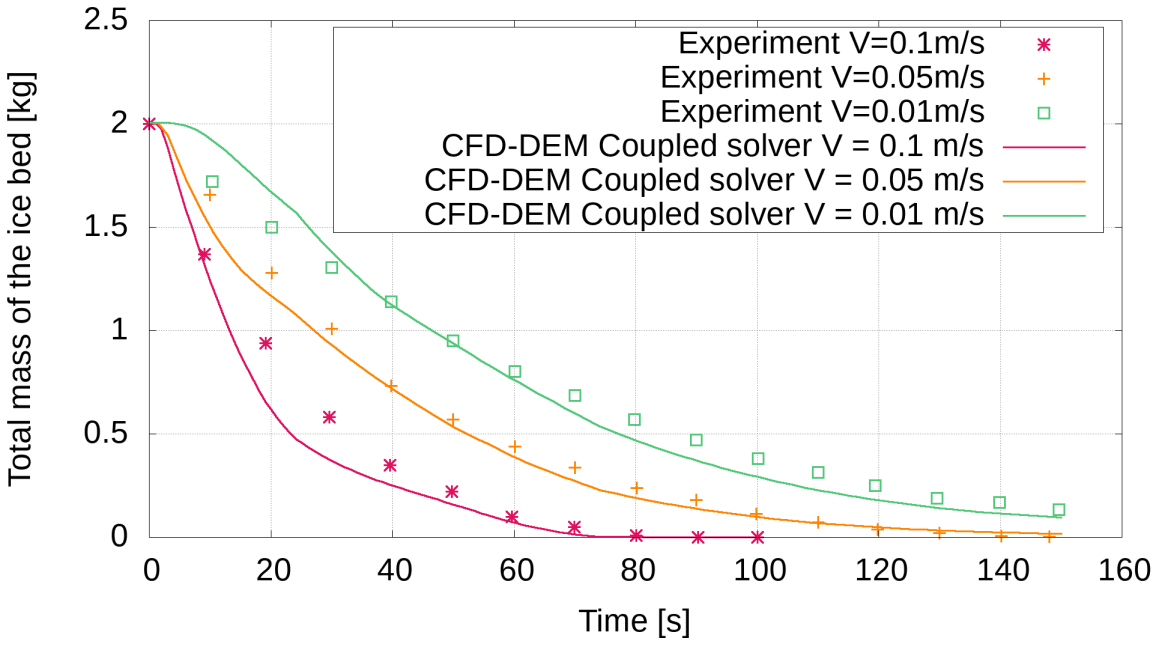

Figure 3.6: Comparison of total mass of the ice packed bed through time for three different inlet velocities

transport phenomena and investigate the effect of different parameters.

3.6 Conclusions

In this study the preliminary steps to develop a Lagrangian-Eulerian model for an additive manufacturing process, more specifically, the selective melting process was described and discussed.

The CFD model was developed in OpenFOAM, in the form of a new solver, *marangoniIcoReact-*

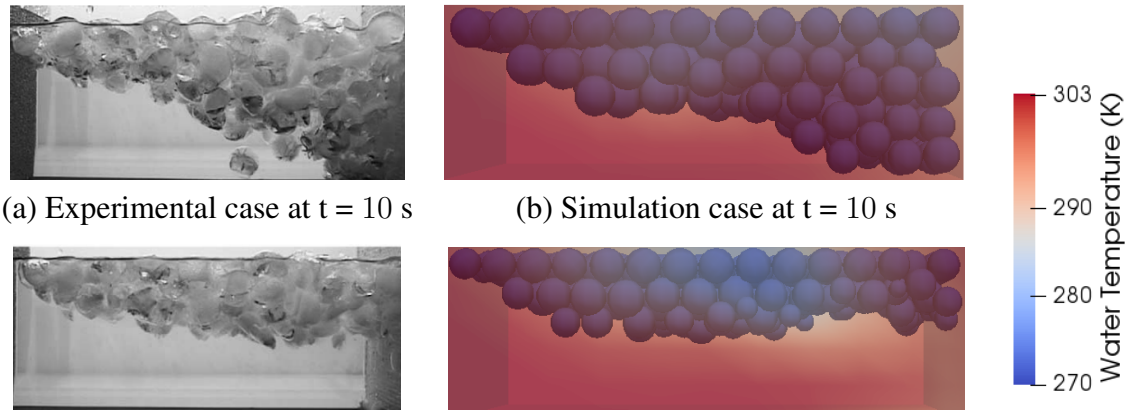

(a) Experimental case at t = 10 s (b) Simulation case at t = 10 s

(c) Experimental case at t = 30 s (d) Simulation case at t = 30 s

Figure 3.7: Floating packed packed subjected to a warm inflowing water. (a) experimental result [105] (b) simulation result. $T_{in} = 303$ K, $V_{in} = 0.07$ m/s

ingMultiphaseInterFoam which is a VOF incompressible solver of N phases with phase-change and considers the Marangoni convection and has a laser model implemented. The solution was validated and compared to a laser spot welding experiment and the results showed agreement with the values reported by the experiment.

Based on the newly developed solver a DEM-coupled solver was developed that couples the solver to XDEM. XDEM reads the physical properties and field data (temperature, velocity, etc.) from OpenFOAM, solves the dynamics and thermodynamics of the particles, and transfers the resulting heat, mass, and momentum sources to the OpenFOAM solver. The coupled solver was validated against two experiments. The first experiment involved a single ice particle subjected to natural convection in a tank of water, and the second involved a packed bed of ice flowing through a channel. The results ensured us that the model is ready and reliable to be applied to an additive manufacturing process.

Chapter 4

A CFD-DEM Coupled OpenFOAM Solver for Multiphysics Simulation of Additive Process: Simulation Results[1]

4.1 Abstract

This study presents a 6-way coupling (mass ,energy, momentum) of computational fluid dynamics and discrete element method (CFD-DEM) for simulating selective laser melting (SLM) processes in a Lagrangian-Eulerian approach. The model incorporates thermodynamics of particles, including phase change and mass transfer, and takes into account the solid-fluid-air mass and heat transfer during the melting of a layer of powder particles using a moving laser beam. The DEM model considers 1D particles discretized in the radial direction and is capable of predicting species and energy distribution along the particle radius. Moreover, convective heat transfer between the particles and the melt is comprehensively investigated and shown to have a significant effect similar to laser heating. The CFD model is used to predict the melt pool evolution and analyze the effect of different parameters on melt pool characteristics. Marangoni and surface tension forces are implemented into the model and interfacial pheomena such as Plateau-Rayleigh instability is captured. In conclusion,

[1]This chapter is written based on the following submitted manuscript: Navid Aminnia, Alvaro Antonio Estupinan Donoso, and Bernhard Peters. "Multi-Scale Modeling of Melt Pool Formation and Solidification in Powder Bed Fusion: A Fully Coupled Computational Fluid Dynamics-extended Discrete Element Method Approach.", Additive Manufacturing, under review, 2023

the model can be used to understand the melt pool dynamics and investigate its interactions with the powder particles, providing insights into how the powder bed and melt pool influence each other during the melting process.

4.2 Introduction

Additive manufacturing (AM) is a method that uses material deposition to create parts layer by layer without the need for specialized tools, based on a 3D representation of the part [107]. Powder Bed Fusion (PBF) is regarded as one of the most promising additive manufacturing (AM) methods for producing complex metal parts, with applications in aerospace, automotive, marine, and biomedical industries [108, 109, 110, 111]. The two most common PBF technologies are Selective Laser Melting (SLM) and Electron Beam Melting (EBM). In these technologies, the powder material is applied on a build platform, and an energy source (laser or electron beam) is used to fuse the powder particles as per the desired geometry. The build platform is then lowered by the prescribed powder layer thickness, the next layer is deposited and the process is repeated until the part is completed (Figure 4.1).

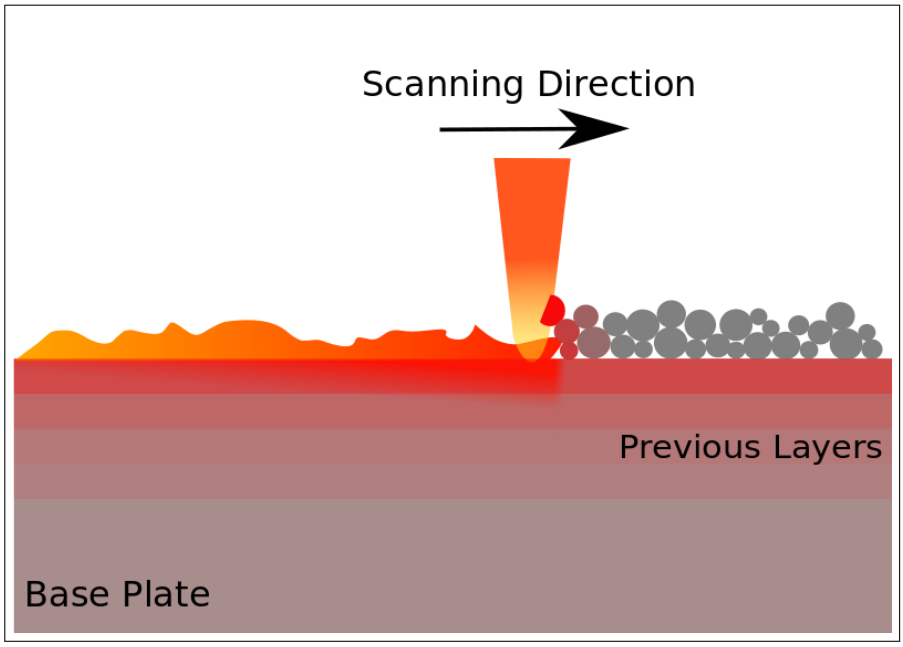

Figure 4.1: A schematic depiction of the Laser Powder Bed Fusion Process is presented.

Parts produced with PBF often exhibit common defects, including balling, cracks, and pores. These defects diminish their reliability, repeatability, and overall quality [112, 5, 113, 114]. These defects are typically caused by the complex dynamics of melt flow and its interaction with the powder particles [66, 73]. Numerous experimental studies have explored the connection between

melt pool characteristics and part defects using both ex-situ and in-situ methods [115, 116, 117, 118, 119]. Nonetheless, experimental setup and measurements can be incredibly time-consuming and labor-intensive. Therefore, physics-based numerical models are ideal for exploring how process parameters and material properties impact the quality of products produced by PBF methods.

Recently there has been a significant rise in interest regarding numerical investigations of metal additive manufacturing, particularly the melt pool behavior in SLM. Researchers have used various numerical methods to address the modeling problem. One of these methods is a pure Eulerian approach to model the powder bed and the melt pool. Ladani et al. [120] developed a 3D FEM model of the powder bed and the melt pool and derived an effective conductive transport mode to account for the conductivity in the continuum bed and the melt pool. Debroy et al. [62] have used an in-house CFD model to investigate SLM. They have applied the data from their cooling rates to estimate dendrite spacing and hardness in different layers of the structure. Dai et al. [121] used Ansys Fluent to simulate the selective laser melting (SLM) of aluminum matrix composites containing AlN particles. They have also analyzed surface morphology variations in keyhole mode and the movement of individual AlN particles and agglomeration effects on the quality of the final part [122]. The AM group from Lawrence Livermore National Laboratory (LLNL) developed a Lagrangian model for the movement of particles. They have explored the effects of process parameters on many defect mechanisms including porosity [66, 123], denudation [66, 67], balling [69] and spatter [66, 124]. Megahed et al. have used the DEM model for the spreading of powder bed and used CFD software to model the radiation, melting, and solidification processes [63, 125, 126].

Researchers have recently explored the capabilities of coupled CFD-DEM to study the powder dynamics such as denudation and spattering in laser melting. Le et al. [88] used a 3D CFD-DEM coupled model to analyze powder entrapment and denudation. The model excludes powder melting and solidification. Yu and Zhao [89] have used a semi-coupled CFD-DEM model in which they have incorporated an Immersed Boundary method for solving the viscous fluid model and a factious CFD domain occupied by the actual positions of the particles in the DEM model. They used the model to study the effects of laser parameters on melting. Zhang et al. [127] have utilized a bi-directionally coupled CFD-DEM model to study the effects of reinforced solid particles on the size and characteristics of the melt pool. Their model incorporates momentum and heat exchange between the DEM and CFD models. However, the details of the heat exchange are not provided.

In their research, Estupinan et al. (2018) suggested employing a coupled model that combines a CFD model with their proprietary DEM model, XDEM. This approach considers the interaction of heat, mass, and momentum between the system and its environment. It connects the discrete approach with the continuous one, which solves for the surrounding fluid phases. In a follow-up research Aminnia et al. [128] proposed an improved model by coupling XDEM to a Volume of Fluid (VOF) solver and incorporating Marangoni force and solidification to the model.

Melting a layer of powder particles with a moving laser beam is a complex process involving multi-phase and multi-physical phenomena, such as thermal transfer, phase transformation, and interactions between solids, fluids, and air. This study aims to comprehend the dynamics of the melt pool and explore its interactions with the powder, determining how the powder bed and melt pool mutually influence each other during the melting process. To achieve this goal, a fully coupled CFD-DEM model (two-way couplings of mass, momentum and heat transfer) is presented that takes into account the phase changes of solid and liquid and the thermal exchange between solid particles, the substrate, the melt, and the ambient gas. The Lagrangian-Eulerian approach with coupled thermodynamics is utilized to account for the thermodynamic behavior of individual particles and obtain a more detailed understanding of the interactions between the powder particles and the melt pool. The eXtended Discrete Element Method (XDEM) method is used as the Lagrangian method and a multiphase CFD solver named icoReactingMultiphaseInterFoam in OpenFOAM is modified and used as the Eulerian method to model the fluid mixture, including the melt, ambient gas, and the solid. The resulting coupled CFD-DEM approach predicts the melt pool evolution and is used to analyze the effect of different parameters on melt pool characteristics.

4.3 Method

XDEM software[97] is used in the current work. This software uses Lagrangian-Eulerian approach to for CFD-DEM coupling. This multi-scale and multi-physics framework considers particles as discrete entities while fluid as a continuous medium.

4.3.1 Governing equations in fluid

4.3.1.1 VOF Model

The Volume Of Fluid (VOF) [129] is a numerical method used in multiphase-flow simulations to capture the interface of phases. In selective laser melting, the evolution of the melt pool is dominantly governed by the deformations of the surface. To fully predict the melt pool deformations, the interface between melt-solid and melt-gas should be captured with acceptable precision. In the VOF method, a conservation equation governs the volume fractions of all the phases. In this study, there are four phases involved: gas, liquid, solid, and particles. The conservation of volume fraction for phase i is solved according to

$$\frac{\partial \alpha_i}{\partial t} + \nabla(\alpha_i . u_i) = \sum_{k=1}^{N} \frac{\dot{m_{net}}}{\rho_i} - \alpha_i \dot{m_{net}} (\frac{1}{\rho_i} - \frac{1}{\rho_k}) \tag{4.3.1}$$

where α_i is the volume fraction of phase i. $\dot{m_{net}}$ is the net mass rate transferred from phase k to phase i. The terms on RHS of equation 4.3.1 are the source terms for volume fraction. The first term

calculates the volume fraction equivalent of the mass rate for phase i and the second term accounts for the density difference between the two phases.

4.3.1.2 Continuity equation

The conservation equations are solved for a single volume-fraction-averaged phase. All the phases are considered incompressible, therefore the continuity equation is simplified as

$$\nabla . \boldsymbol{u} = 0 \tag{4.3.2}$$

where $\boldsymbol{u}$ is the velocity vector field.

4.3.1.3 Navier-Stokes equations

The conservation of momentum is satisfied by the equation

$$\frac{\partial}{\partial t}(\rho \boldsymbol{u}) + \nabla \cdot (\rho \boldsymbol{u}\boldsymbol{u}) = -\nabla p + \rho \boldsymbol{g} + \nabla \cdot \left[\mu \left(\nabla \boldsymbol{u} + \nabla (\boldsymbol{u})^T\right)\right] + \boldsymbol{S}_m \tag{4.3.3}$$

where ρ is density of the fluid mixture, p pressure, $\boldsymbol{g}$ the gravity acceleration vector and μ is the average kinematic viscosity of the fluid mixture. The last term, $\boldsymbol{S}_m$ represents all the additional momentum source terms that will follow.

Mushy zone flow resistance

A mushy zone [130], as illustrated in figure 4.2, is a region of partially solidified liquid within a solid-liquid mixture. This zone is considered a porous region where solid and liquid are in equilibrium and both maintain a volume fraction between 0 and 1. The mushy zone exerts a drag on the flow which is directly proportional to the flow velocity. To account for this drag force Brent et al.[131] recommended a term in the form of the Carman-Kozeny equation,

$$S_m(\text{mushy zone}) = -C\frac{(1-\alpha_l)^2}{{\alpha_l}^3 + \epsilon}\boldsymbol{u} \tag{4.3.4}$$

where the constant C is a parameter that controls the extent to which the convection field penetrates the mushy region[131]. It is set to a value sufficiently large to ensure that as the liquid solidifies, the region becomes static. Equation 4.3.4 indicates that the mushy zone source term equals zero for fully liquid cells and maintains a large value for a solidified cell.

Surface forces

Surface forces at the interface between a liquid and a solid or a gas play a significant role in the behavior of melt pool flows. These forces include surface tension force and Marangoni force.

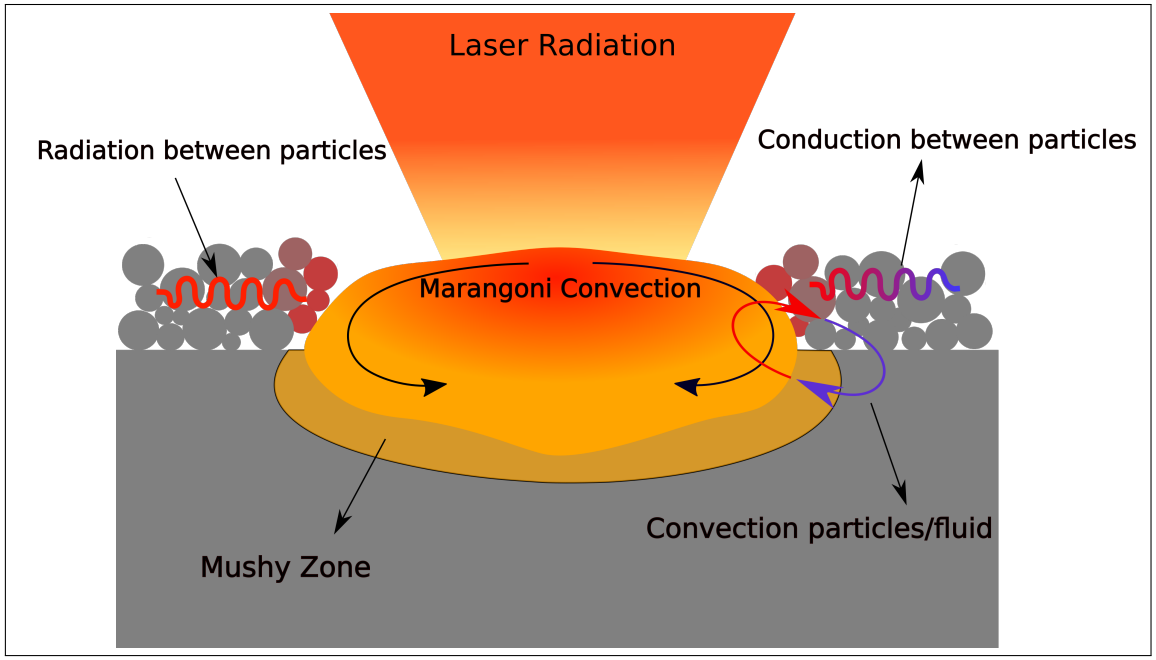

Figure 4.2: The heat and mass transfer mechanisms of the melt pool

Surface tension force arises due to the cohesive forces between the molecules at the surface of a liquid. These forces act to minimize the surface area of the liquid and cause it to form a spherical ball at the surface of the solid substrate as described by the Plateau-Rayleigh instability theory[54]. This phenomenon is called the balling effect which can cause the molten metal to splatter and form droplets, which can lead to surface roughness and defects in the finished part[66]. The surface tension force acts as a normal force at the interface between the liquid phase and gas or solid, defined by the equation

$$S_m(\text{surface tension}) = \sigma\kappa\boldsymbol{n}|\nabla\alpha| \tag{4.3.5}$$

where σ is the surface tension coefficient between the two phases at the interface and is dependent on material properties, κ is the curvature of the interface and $\boldsymbol{n}$ is the interface normal vector. $|\nabla\alpha|$ represents the gradient of the volume fraction of the liquid, which serves as the Delta function that converts the surface force to a volumetric force according to the Continuum Surface Force(CSF) method proposed by Brackbill et al.[100].

The Marangoni effect involves the fluid flow being influenced by a change in surface tension. This change can be caused by a gradient in temperature or concentration, and it creates a force that drives the fluid from areas of high surface tension to areas of low surface tension. For example, when a liquid is heated by a laser, the high temperature at the point of impact may lead to high surface tension. This high surface tension creates a Marangoni force that pushes the liquid away from the heat source and towards the cooler regions at the edges of the liquid (Figure 4.2).

$$S_m(\text{Marangoni force}) = \frac{\mathrm{d}\sigma}{\mathrm{d}T}(\boldsymbol{\nabla T} - \boldsymbol{n}(\boldsymbol{n}.\boldsymbol{\nabla} T)) \tag{4.3.6}$$

The derivative of surface tension with respect to temperature, denoted as $\frac{\partial \sigma}{\partial T}$, is a measure of how the surface tension of a metal material changes with temperature. The term in parentheses extracts the component of the temperature gradient that is tangent to the curvature of the melt surface.

4.3.1.4 Energy equation

The equation for energy conservation is defined as

$$\frac{\partial(\rho C_p T)}{\partial t} + \nabla.(\rho C_p T \boldsymbol{u}) = \nabla.(\kappa \nabla T) - L_f(\dot{m}_{sl} - \dot{m}_{ls}) + S_h \tag{4.3.7}$$

where the specific heat of the mixture is represented by C_p, the temperature is represented by T, the heat conduction coefficient is represented by κ, and the latent heat for melting/solidification is represented by L_f. The term $L_f(\dot{m}_{sl} - \dot{m}_{ls})$ indicates the change in enthalpy during the process of solidification or melting. It is important to note that, in this model, the melting of particles is solely handled by XDEM. As a result, the fluid model only considers the melting of the solid substrate or the solidified melt. S_h denotes the energy equation source terms described in section 4.3.3.

4.3.2 Governing equations for discrete particles

XDEM predicts both dynamics and thermodynamics of the powder particles. The particle position, velocity, and acceleration are calculated with the dynamics module of XDEM, whereas the temperature and processes like heat transfer, radiation, and melting are calculated within the conversion module.

4.3.2.1 Dynamics Module

The XDEM dynamics module employs the Discrete Element Method (DEM) that is based on the soft sphere model. This method assumes that the particles are flexible and can overlap, with the extent of overlap determined by the contact force based on the force-displacement law. The particle rigidity is expressed through Young's Modulus, and the energy dissipation of the particle is accounted for through the use of a dashpot. The movement of each particle, both translationally and rotationally, is monitored using classical mechanics equations. Further information on these terms can be found in a previous study by Baniasadi et al. [98]. A brief overview of the equations for both translational and rotational motion is provided below: Equations of particle motion are described by

$$m_i \frac{d\boldsymbol{v_i}}{dt} = m_i \frac{d^2 \boldsymbol{X_i}}{dt^2} = \boldsymbol{F_{c,i}} + \boldsymbol{F_{g,i}} + \boldsymbol{F_{ext,i}}, \tag{4.3.8}$$

and

$$I_i \frac{d\boldsymbol{\omega_i}}{dt} = \sum_{j=1}^{n} \boldsymbol{M_{i,j}}, \tag{4.3.9}$$

where $\boldsymbol{F_{c,i}}$ is the contact forces with neighbor particles and $\boldsymbol{F_{g,i}}$ is the gravity force. $\boldsymbol{F_{ext,i}}$ is the sum of all the external forces acting on the particle, such as buoyancy and drag forces. The details of these source terms are further explained in [128].

4.3.2.2 Conversion module

The conversion module resolves the conservation equations for momentum, mass, energy (and species) within the radially discretized particles. The equation for mass conservation is also solved for the fluid entrained within the particle pores according to

$$\frac{\partial}{\partial t}\left(\epsilon_f \rho_f\right) + \boldsymbol{\nabla} \cdot \left(\epsilon_f \rho_f \boldsymbol{v_f}\right) = \dot{m}_{s,f} \tag{4.3.10}$$

and one-dimensional transient energy equation is solved for all the particles by

$$\frac{\partial \rho c_p T}{\partial t} = \frac{1}{r_n}\frac{\partial}{\partial r}\left(r^n \lambda_{eff}\frac{\partial T}{\partial r}\right) - r^n\left(\boldsymbol{v}\rho_f c_{p_f} T\right) \tag{4.3.11}$$

These governing equations are subjected to the following boundary conditions:

$$-\lambda_{eff}\frac{\partial T}{\partial r}\bigg|_{r=0} = 0, \tag{4.3.12}$$

$$-\lambda_{eff}\frac{\partial T}{\partial r}\bigg|_{r=R} = \alpha(T_R - T_\infty) + q''_{rad} + q''_{cond} + q''_{laser}, \tag{4.3.13}$$

and

$$-D_{i,eff}\,\frac{\partial \rho_i}{\partial r}\bigg|_{r=R} = \beta_i\left(\rho_{i,R} - \rho_{i,\infty}\right) \tag{4.3.14}$$

λ_{eff} is the effective thermal conductivity of the metal powder particles that may be defined as time-dependent. $\alpha(T_R - T_\infty)$ denotes the convective heat transfer between the particle (the element at $r = R$) and the fluid (the melt and the surrounding gas) and is directly corresponding to the heat source presented in 4.3.18. q''_{laser} is consistent with the laser formulation of the CFD model presented in equation 4.3.19 except it also considers a depth-dependent heat profile according to [96]. q''_{rad} and q''_{cond} represent conduction and radiation heat flux between the particle and the neighbor particles. Equation 4.3.14 describes the diffusivity of the entrained particle gas to the ambient. The aforementioned equations and the conversion model are described more in detail in [99, 98]. In equation 4.3.13, α is the convective heat transfer coefficient that is calculated based on the Reynolds and Prandtl numbers of the fluid according to a experimental correlation from Yang et al. [132] for convective heat transfer in packed beds:

$$\alpha = \frac{Nu.\lambda}{d_p} \tag{4.3.15}$$

Where Nu is Nusselt number and d_p is the particle diameter. Nusselt number is calculated by:

$$Nu = a_1 + a_2 Pr^{1/3} Re^n \left(\frac{d_p}{d_h} \phi \right) \tag{4.3.16}$$

Where $a_1 = 1.73$ and $a_2 = 0.2$ and $n = 0.7$ are heat transfer model constants. d_p and d_h is pore scale hydraulic diameter and ϕ is the porosity or the fraction of the cell that is not occupied by a particle.

4.3.3 CFD-DEM Coupling

The coupling of CFD and DEM is accomplished through a common staggered approach. This method involves utilizing the output from one simulation as input for the other. For this discussion, let us assume that one simulation is a fluid solver, and the other simulation is a DEM solver. The fluid solver solves for various quantities such as momentum, mass, and energy for the fluid. These quantities, such as fluid velocity, temperature, viscosity of the mixture, etc., are then utilized as boundary conditions for the particles in the DEM solver.

The DEM solver uses the output from the fluid solver to calculate different source terms such as melt mass source and convective heat source, by solving for momentum and energy equations for the particles. In the following time step, these source terms are shared with the fluid solver, which then uses the solution from the previous time step to obtain a new solution for the current time step. The source term is link the energy and mass equations in the two solvers are as follows:

Imported melt enthalpy

The phase transition of particles from solid to liquid is comprehensively simulated within XDEM. The resulting molten material is promptly conveyed to the fluid mixture using the "immediateLiquidTransfer" mechanism in XDEM. This transfer of mass is replicated in the CFD simulation by moving mass from a fictitious particle phase to the liquid phase. This special particle phase in the CFD simulation is structured to influence solely the conservation of volume fraction equation, without affecting the momentum and energy equations. Thus, when the particles melt in XDEM, the volume fraction corresponding to the mass of the melted particles is calculated, and this fraction is then converted into the liquid phase.

However, it's important to note that the melt introduced from XDEM carries the temperature of the melting point. The fictitious particle phase, on the other hand, exists within a fluid mixture that might be at a higher temperature (in cases where the majority of the cell is occupied by liquid melt) or a lower temperature (if the surrounding phase is predominantly composed of gas). To adjust the cell's temperature to the incoming melt temperature, it becomes necessary to calculate the difference

in enthalpy between the incoming melt and the fictitious particles (which are at the temperature of the fluid mixture).

Thus, it is essential to consider the difference in enthalpy between the melt and the particles. This is implemented by the source term,

$$S_h\,(\text{melt enthalpy difference}) = h_{imported\ melt}\,(T_m, p) - h_{fictitious\ particles}\,(T, p) \tag{4.3.17}$$

where $h_{imported\ melt}$ and $h_{fictious\ particles}$ are the enthalpy of melt and particles at their respective temperatures and pressures. The melt is at melting temperature, T_m, while the fictitious particles have the temperature as that of the fluid mixture in the model.

Convective heat transfer with particles

The fluids in the CFD model are subjected to convective heat transfer with the particles that are modeled in XDEM. This heat transfer is implemented as a heat source in both XDEM and CFD models on the right-hand side of the energy equation and is calculated according to the following equation:

$$S_h(\text{Convection}) = \alpha(T_{fluid} - T_{particle\ surface}) \tag{4.3.18}$$

α is the convective heat transfer coefficient and is calculated according to equation 4.3.16.

Laser heat source

In this model, the laser heat source is coupled between XDEM and the CFD model. In XDEM, the laser is calculated as a prescribed surface heat flux applied to all the particles. Based on the laser power consumption in XDEM, the available laser power in the CFD model is determined. In the CFD model, the laser is represented as a volumetric heat source located at the interface of the melt pool and the surrounding gas. In both models, the laser is defined as a moving Gaussian distribution according to the following equation:

$$q''_{laser} = \frac{g\eta P_{laser}}{\pi R^2} exp\left(-2\frac{(x - x_0 - \nu t)^2 + (y - y_0)^2}{R^2}\right) f(z) \tag{4.3.19}$$

q'' is the laser surface heat flux that radiates on the top surface of the melt pool. P_{laser} is a measure of the beam power such that the area integral of the equation 4.3.19 over the radiated surface should be equal to the total power that is available for the CFD model. g is a constant geometric factor that completes the Gaussian profile. It defines the concentration of the profile over the center. Mostly, for simulation of powder bed fusion laser, $g = 2$ is used [133, 134]. The numerator of the exponential term calculates the distance from the laser center at each time. R is the beam diameter, x_0 and y_0 are the coordinates of the laser center, ν is the laser velocity and t is elapsed time. $f(z)$ is the depth dependence of the laser radiation. In formulation of the laser in CFD this term would be omitted

because the laser is implemented on the top surface of the melt. However, in XDEM the surface heat flux of each particle is dependent on its depth [135]:

$$f(z) = exp(-\beta z) \tag{4.3.20}$$

The heat source for the laser in CFD is calculated according to the following equation:

$$S_h(laser) = \frac{q''_{laser}}{\delta z} \tag{4.3.21}$$

δz is the dimension of the CFD mesh cell in the laser direction. The equation 4.3.21 converts the surface heat flux, $q''_{laser}(W/m^2)$ to a volumetric heat source (W/m^3)

In the present study, the coupling does not consider the laser radiation transmission between the particles and the melt because as explained in section 4.5.3, the surface radiation has an insignificant impact on the transport phenomena of the melt pool and powder bed.

4.3.4 Simulation setup

In the present study the results for two different geometry and case setups are presented. The first case is the *validation case* which is set up based on an experimental study [136]. The second case, named *Deposited Powder Bed Case* is using similar physical properties as the validation case, but a larger powder bed with random arrangement and size of the powder particles. The powder is generated by dropping powders in the XDEM model on the substrate and letting them settle.

The simulation time step in both of the cases is constantly 10^{-7} s. The material properties of the substrate and the particles are set as that of Ti-64Al-4V alloy [137]. The properties of the material and other case parameters are listed in Table 4.1. At the initial state, particles in the XDEM and the fluid mixture and substrate in the fluid model are at an initial temperature of $300K$. The boundary condition for the temperature at the bottom of the substrate is at fixed temperature $(300K)$ and other boundaries are set as zero heat flux. The top surface is considered as open air and *inletOutlet* boundary condition.

Validation Case

To conduct the simulations for this study the experimental work conducted by Wu et al. [136] was numerically reproduced. The simulation geometry consists of a single layer of spherical powder with a particle diameter of 35 μm, which is deposited onto a 1 mm long substrate. The simulations are divided into four different scenarios with a similar laser power scanned at different velocities: 850 mm/s, 1050 mm/s, 1250 mm/s, and 1450 mm/s.

A uniform, single-layer powder bed is generated by XDEM and placed on top of the solid substrate in the CFD model to establish the initial state of the simulation. The volume fraction of

particles in the CFD model represents the corresponding particle phase in the XDEM model. To achieve this representation, the mapping of particles to CFD cell volume fractions is carried out following Xiao et al. [138]. According to the limitations of this method, the mesh size of the fluid model can not exceed the particle size. for this case, a mesh size equal to the diameter of each particle (35 μm) is used.

Deposited Powder Bed Case

A layer of powder that is 60 μm thick is placed onto a solid substrate that is 130 μm thick. The powder bed is generated with particles following a normal size distribution with an average particle diameter of 35 μm and a standard deviation of 0.3. After generation they are deposited on top of the substrate by letting them fall freely. The overall geometry is shown in figure 4.4. The size of each mesh cell used for the CFD model is equal to the average particle diameter (35 μm).

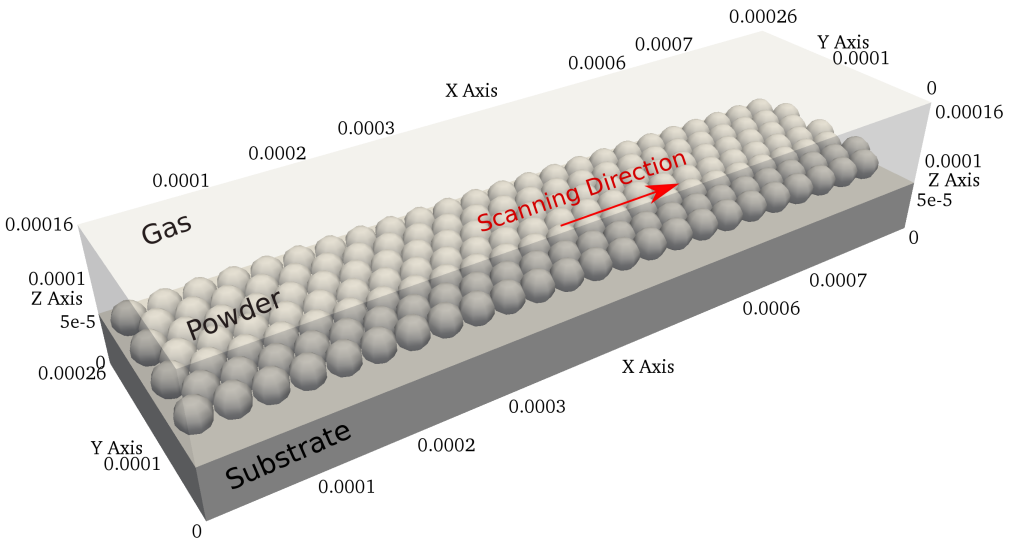

Figure 4.3: 3D Geometry of the validation case. A layer of powder on top of a solid substrate surrounded by ambient gas.

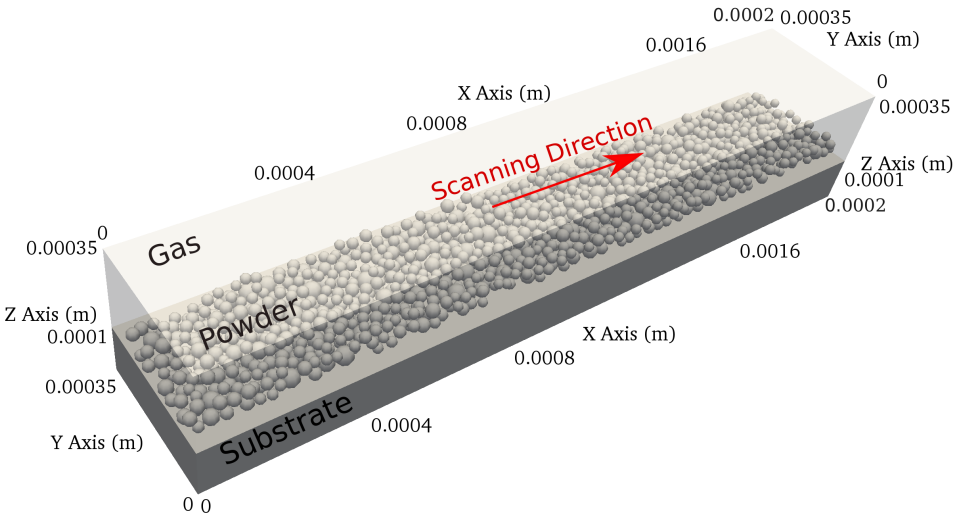

Figure 4.4: 3D Geometry of the Deposited bed case. A layer of powder with 60 μm thickness, deposited on top of a solid substrate surrounded by ambient gas.

Table 4.1: Material properties and setup parameters used

Parameters	**Values**
Density of Solid/Particle (ρ_s)	4420 $\mathrm{kg\ m^{-3}}$
Density of Liquid (ρ_l)	3682 $\mathrm{kg\ m^{-3}}$
Density of Gas (ρ_g)	1.78 $\mathrm{kg\ m^{-3}}$
Specific Heat Capacity of Solid (C_{p_s})	670 $\mathrm{J\ kg^{-1}\ K^{-1}}$
Specific Heat Capacity of Liquid (C_{p_l})	831 $\mathrm{J\ kg^{-1}\ K^{-1}}$
Specific heat capacity of gas (C_{p_g})	520 $\mathrm{J\ kg^{-1}\ K^{-1}}$
Thermal Conductivity of Solid (k_s)	10.6 $\mathrm{W\ m^{-1}\ K^{-1}}$
Thermal Conductivity of Liquid (k_l)	33.4 $\mathrm{W\ m^{-1}\ K^{-1}}$
Thermal conductivity of gas (k_g)	1.77×10^{-2} $\mathrm{W\ m^{-1}\ K^{-1}}$
Dynamic Viscosity of Liquid (μ_l)	0.00254 $\mathrm{kg\ m^{-1}\ s^{-1}}$
Dynamic viscosity of gas (μ_g)	2.2×10^{-5} $\mathrm{kg\ m^{-1}\ s^{-1}}$
Latent Heat of Fusion (L_f)	2.86×10^5 $\mathrm{J\ kg^{-1}}$
Liquidus temperature (T_l)	1923 K
Solidus temperature (T_s)	1877 K
Solidification coefficient (β_{ls})	2×10^3 $\mathrm{s^{-1}}$
Melting coefficient (β_{sl})	1×10^6 $\mathrm{s^{-1}}$
Surface tension (σ)	1.5 $\mathrm{kg\ s^{-2}}$
Thermal expansion coefficient ($\frac{\mathrm{d}\sigma}{\mathrm{d}T}$)	-2.6 $\times 10^{-4}$ $\mathrm{kg\ s^{-2}\ K^{-1}}$
Mushy zone constant (C)	10^8 $\mathrm{kg\ m^{-3}\ s^{-1}}$
Ambient pressure (P_0)	10^5 Pa
Stefan-Boltzmann constant (σ_{sb})	5.67×10^{-8} $\mathrm{W\ m^{-2}\ K^{-4}}$
Convective heat transfer coefficient (h_c)	Correlation [132]
Laser power (P_{laser})	175 W
Laser beam radius (R)	70 μm
Absorptivity of solid (η_s)	0.6
Absorptivity of liquid (η_l)	0.3

4.4 Results

4.5 Model validation

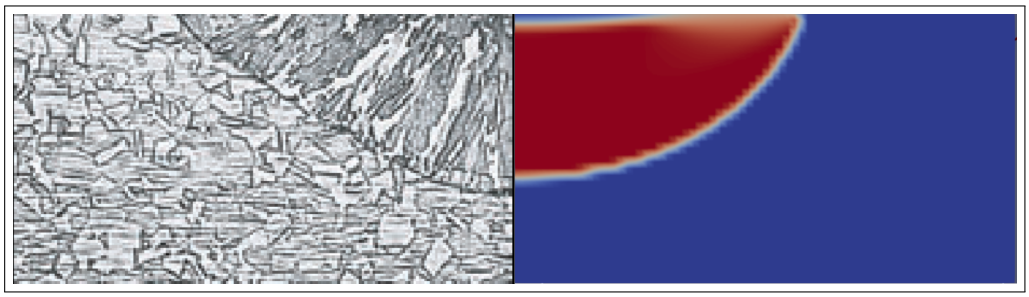

Figure 4.5: Comparison of the melt pool dimension of spot laser welding experiment [102] (left) against the results from the pure CFD model (right)

The study is divided into stages, with each stage containing distinct elements of the model that were constructed step by step and tested against an experiment to ensure the quality, dependability, and precision of the results. The validation results of the Marangoni model, laser melting and the CFD-DEM coupling's heat and mass transfer is presented in a previous article [128]. Figure 4.5 shows the agreement of the melt pool prediction by the CFD solver against the experimental results by He et. al [102].

4.5.1 Validation for selective laser melting process

The simulation setup described in 4.3.4 is used as the base case of the present study. Similarly to the original experimental study, four different cases are simulated for four different velocities and the melt pool width is validated against the reported experimental results [136].

The comparison of the simulation results against the experiments are depicted in figure 4.6. The results indicate that the melt pool width gradually decreases as laser scan velocity increases. This is because decreasing scan velocity results in an increased laser residence time at each point in the melt pool, leading to higher radiation heat for both the melt pool and substrate. This results in two related consequences. Firstly, the temperature difference between the laser impact point and the edges of the melt pool is greater, causing an increase in Marangoni convection within the melt pool which expands the width of the pool. Secondly, the stronger convection within the melt pool causes more of the substrate to melt, increasing the melt pool depth and also the melt volume in circulation which in turn causes a further increase in melt pool width.

As explained in 4.3.4, the discrepancy between the simulation results and the experimental data at lower velocities can be attributed to the constraints of the mesh size. Large mesh size in the

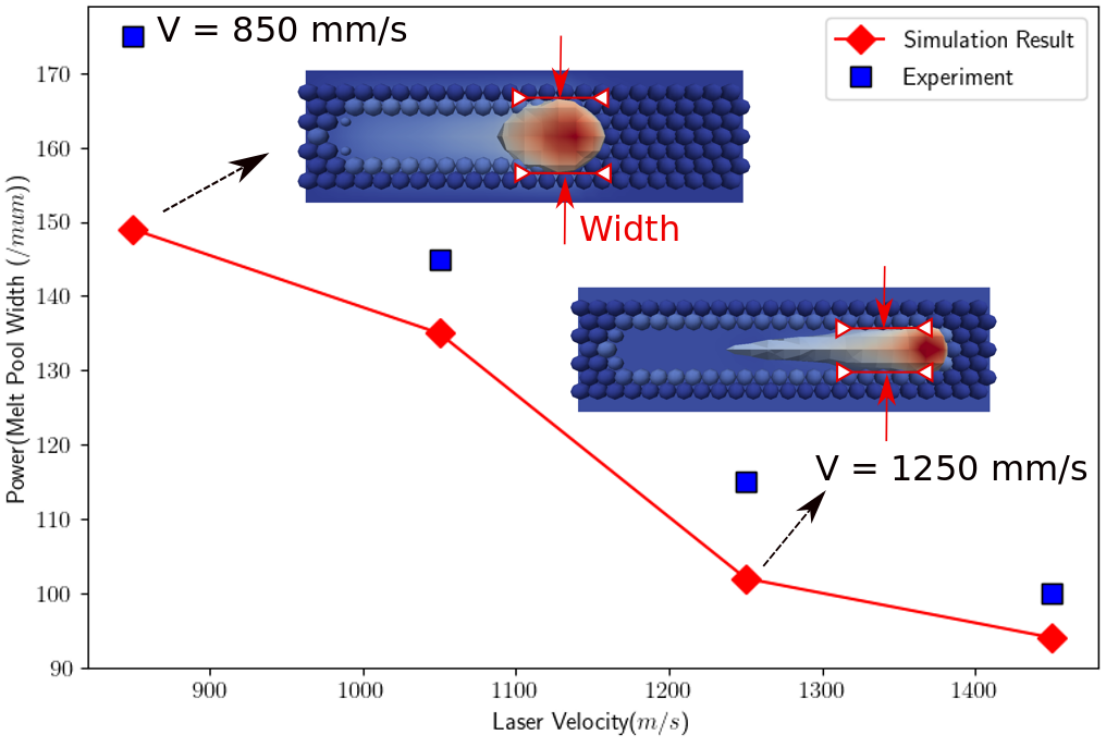

Figure 4.6: Comparison of the melt pool width of a selective laser melting experiment [136] against the results from a 3D CFD-DEM coupled simulation

CFD domain results in an underestimation of the Marangoni flow in the melt pool. The temperature profile within the melt pool naturally exhibits a non-linear variation from the laser incident point to the pool edges. However, using a larger mesh size to estimate the temperature gradient will assume a linear profile instead, resulting in an underestimation of the intense Marangoni force near the laser center. In the case with lower velocity where the width of the melt pool is more strongly governed by the Marangoni convection compared to other cases, the simulation's margin of error is larger.

As previously stated, the laser radiation heat source is defined for both the XDEM and CFD solvers. One crucial aspect of the developed CFD-DEM coupling is the laser coupling which ensures that the total laser power is conserved. The laser heat source is defined as a surface heat flux for the particles in XDEM. The laser heat source in the CFD solver is defined as a surface heat flux on the top surface of the melt pool. This heat source has a Gaussian distribution exactly similar to the XDEM laser heat source. Its maximum value however is the remnant of the total laser power after it is consumed by XDEM particles. Figure 4.7 shows the laser power conservation in the coupling for the four cases. The orange curve represents the total power absorbed by the XDEM particles, while the blue curve represents the total power absorption by the CFD cells. The red curve, on the other hand, depicts the combined absorbed power in the two models to the total available laser power. This curve indicates that 100% of the total laser power (175 W) is consumed at all times for the four

scan velocities.

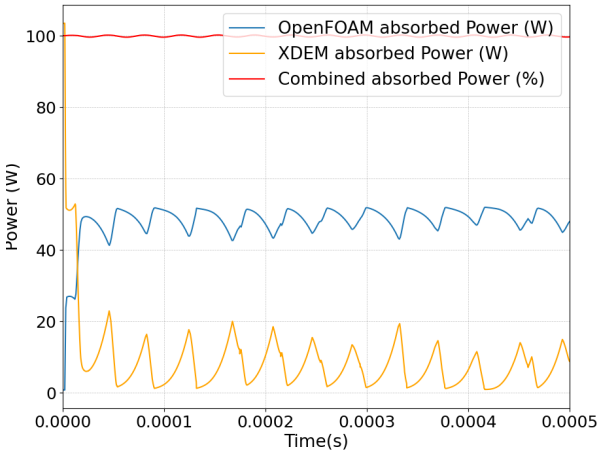

(a) Laser scan velocity = 850 mm/s

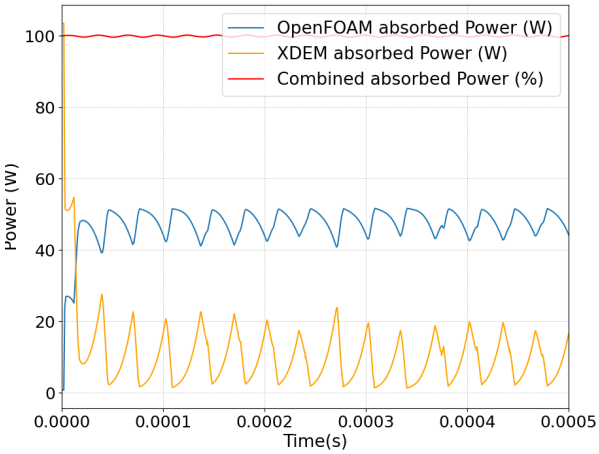

(b) Laser scan velocity = 1050 mm/s

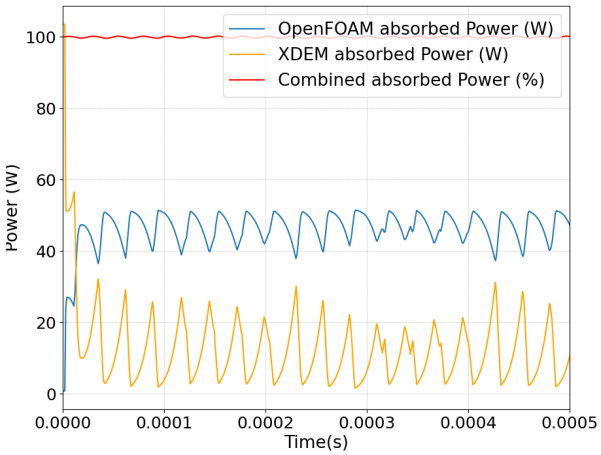

(c) Laser scan velocity = 1250 mm/s

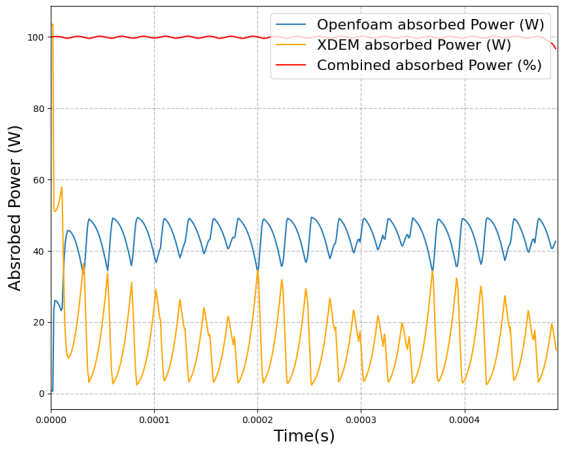

(d) Laser scan velocity = 1450 mm/s

Figure 4.7: Validation of laser power conservation in the laser coupling between XDEM and CFD solvers for four different laser scan velocities

As the laser scan velocity increases, the powder bed experiences a higher heat input from the laser. Within a few time steps of exposure to laser radiation, the particles melt and disappear from the simulation domain. Therefore, there are no remaining particles in the laser sweeping area to absorb heat. Instead, the excess heat is transferred to the CFD cells, including both the substrate and the melt pool. In other words, during most of the process, except for an initial short period of time, the laser interacts primarily with the melt pool. This is coherent with experimental observations [139].

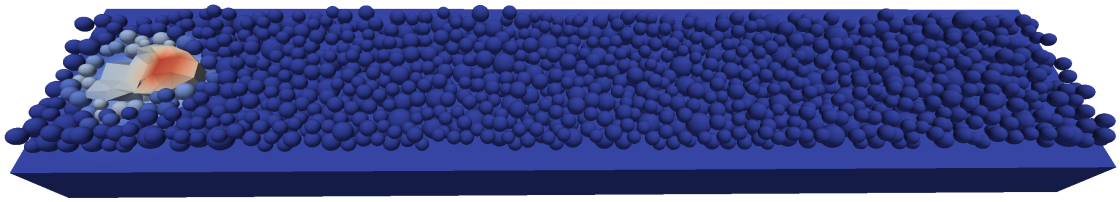

(a) Laser scan velocity = 1050 m/s at t = 150 μs

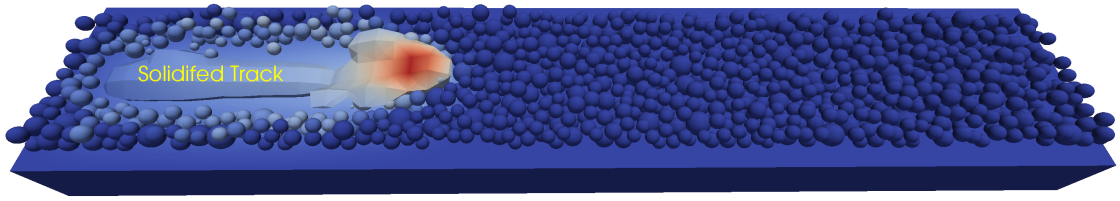

(b) Laser scan velocity = 1050 m/s at t = 600 μs

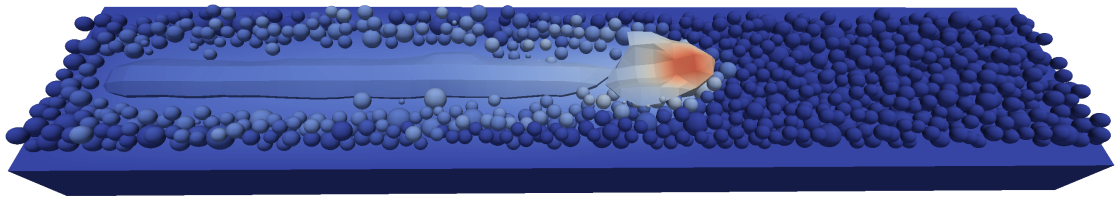

(c) Laser scan velocity = 1050 m/s at t = 1100 μs

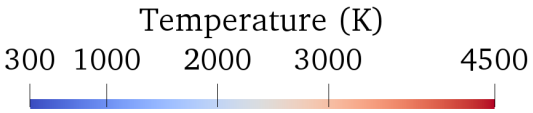

Figure 4.8: Evolution of melt pool in selective laser melting process at laser scan velocity of 1050 mm/s (a, c, e) and 1250 mm/s (b, d, f)

4.5.2 Formation and evolution of the melt pool

Figure 4.8 shows the evolution of the melt pool at the first 1100 microseconds of the simulation for scan velocity of 1050 mm/s. The laser beam scans the powder bed from left to the right. As soon as 20 microseconds, the powder particles at the laser incident point already reach the melting temperature. From this point onward, the powder particles in the laser path start to melt and gradually the melt pool starts to expand in the laser scanning direction. As shown in figure 4.8a, after 150 microseconds. the colder end of the melt pool starts to cool down to solidus temperature and thereafter a solidification track starts forming at the back of the melt pool. The solidified track is annotated in figure 4.8b. The visual representation of the melt pools depicted in figure 4.8 is achieved by delineating the contours for the liquid volume fraction (α_{liquid}) at a threshold value of

0.16. The justification for the chosen threshold values is based on a comparison between the liquid volume within the demonstrated melt pool, the amount of imported liquid volume from XDEM, and the volume of the solid substrate that has melted. The threshold for visualization of the solidified track is calculated by dividing 0.16 by the ratio of solid density to liquid density, 1.2. The division results in 0.133.

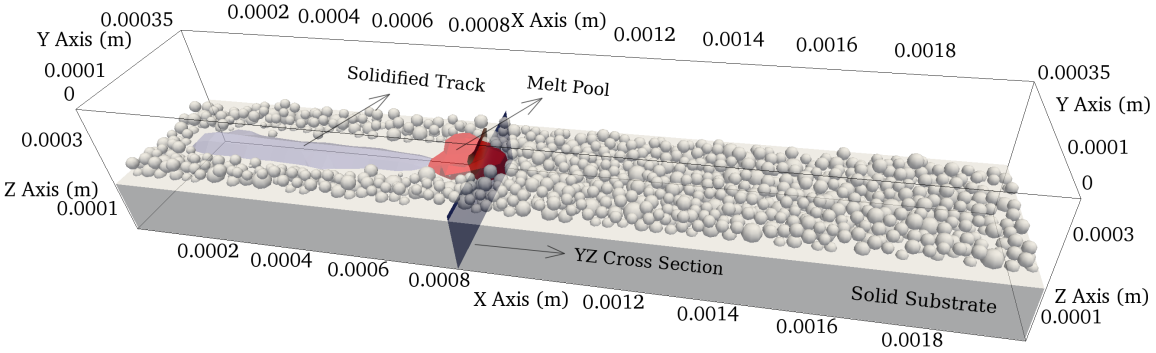

(a) The investigated YZ cross-section is located at X=0.0008 m

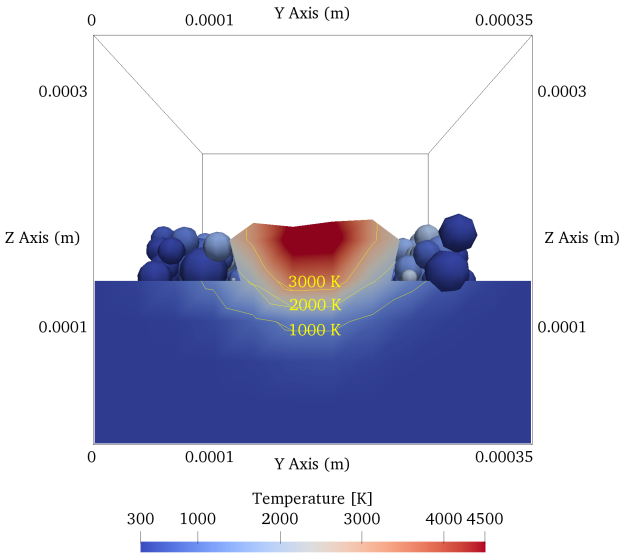

(b) Temperature contours

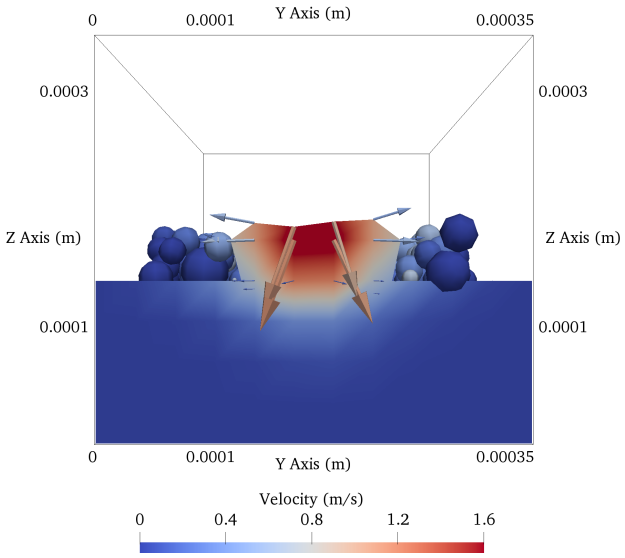

(c) Velocity vectors

Figure 4.9: Temperature contours and velocity vectors at a YZ plane cross section located at X=0.0008 m at the time of t = 750 μs. In all images the simulation domain (melt, solid, particles) is colored by temperature

The melt pool reaches the maximum temperature of about 4500 K at the laser incident point. Due to the high temperature gradients at the this point, the Marangoni force is rather large and creates a flow of melt in the directions away from the laser center and thus expanding the melt pool in width, length, and depth. Figure 4.9 shows a cross-section of the simulation domain at the location X = 0.0008 m at the the time of t = 750 μs. It can be seen that the melt pool (the

region with a temperature above 1923 K, the melting temperature) has penetrated in depth and fused into the solid substrate. The depth of the melt pool is dependent on the laser power and scanning velocity as well as the thermophysical properties of all phases. The Marangoni force also plays a significant role in increasing the depth of the melt pool. This is due to the induced circular flow, which facilitates the transfer of heat to the solid-liquid interface and pushes the mushy zone deeper into the solid substrate, ultimately contributing to the overall depth of the melt pool. Figure 4.9c shows the velocity vectors in the depicted XZ plane. It can be seen that at the edges of the melt pool, the velocity has a rather strong tangential component which indicates the presence of Marangoni force due to the temperature gradient. Closer to the center of the melt pool the velocity vectors are mostly in the radial direction which indicates the dominance of gravity and surface tension that are pulling the liquid surface down.

Figure 4.10 depicts an XZ cross-section of the simulation domain located at Y = 0.0001875 m, i. e., the middle cross-section of the geometry in the Y-direction. Figure 4.10a demonstrates the temperature distribution in the melt pool, the solid substrate and the solidified track which is marked by the white contour and an annotation. This contour is representing the part of the CFD domain which is resolidified and has a solid fraction of 0.133 (the value is explained in section 4.5.2). It can be seen the interface of the solidified track and the melt coincides with the region associated with mushy zone, i.e., the region with temperature at about melting temperature (1923 K).

It can be seen that as the laser moves forward to the right and fuses more particles into the melt, the length of the melt increases on the leading edge. However on the trailing edge the temperature of the melt falls below melting temperature and the melt joins into the solidified track. The length of the melt pool is dependent on the scan velocity, solidification coefficient, and surface tension of the gas-liquid interface, as explained in the following analysis of the relevant thermal and fluid dynamic phenomena.

The laser scanning velocity is a crucial parameter that determines the length of the melt pool. Increasing the scanning velocity results in more material being melted at the leading edge before the same volume of material at the trailing edge has enough time to solidify. As a result, the length of the melt pool increases. The solidification coefficient is a simulation parameter (Table 4.1) in the phase change model [140] which should be fine-tuned according to the problem. Increasing this value leads to faster solidification of the cooled-down liquid and therefore smaller melt pool. Increasing this value would result in a larger melt pool and a wider mushy zone. Surface tension coefficient (σ in equation 4.3.5) plays a significant role in the shaping of the melt pool mostly because of the Plateau-Rayleigh instability phenomenon [141]. According to this theory, when the length-to-width ratio of a melt pool exceeds π, the instabilities on the surface of the pool can become significant enough to overcome the surface tension, causing the pool to break up into droplets [142]. Such behavior is observed in the simulation result for higher scan velocities. Figure 4.11 shows two

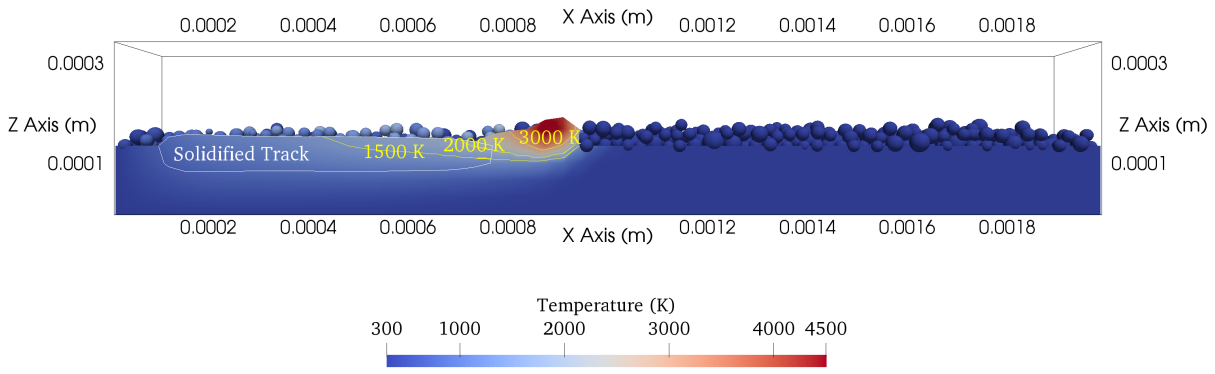

(a) Temperature contours

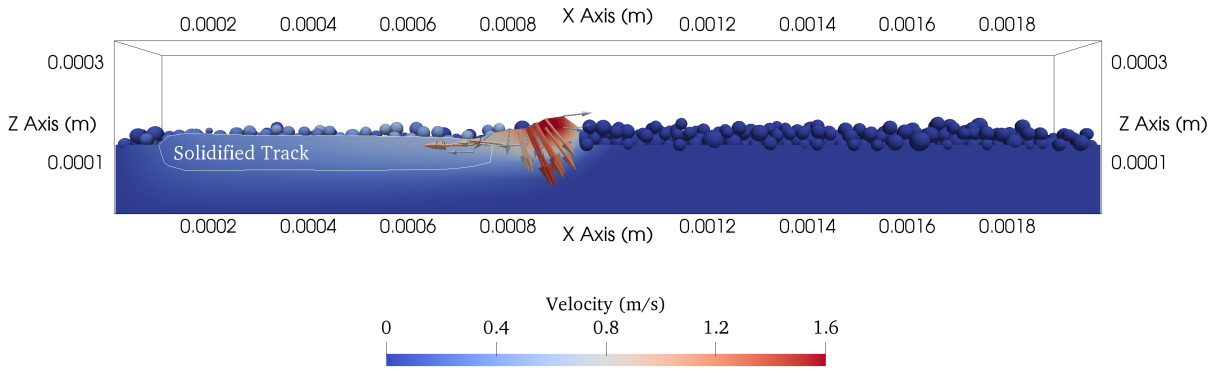

(b) Velocity vectors

Figure 4.10: Temperature contours and velocity vectors at an XZ middle cross-section for scanning velocity of 1050 mm/s. In both images the simulation domain (melt, solid, particles) is colored by temperature

instances of such occurrences. In figure 4.11a, the melt pool is shown at a laser scan velocity of 1250 mm/s and a length-to-width ratio of 3.5, where a small droplet of melt begins to separate from the pool. Likewise, in figure 4.11c, the melt pool is shown at a laser scan velocity of 1450 mm/s and a length-to-width ratio of 3.75, which is close to breaking into a small and a large portion.

4.5.3 Particles heat transfer

The XDEM conversion module predicts various processes such as particle melting, laser radiation acting on the particles, convective heat transfer between the particles and the surrounding fluids, as well as conduction and radiation between the particles themselves. Of all these mechanisms, laser radiation is the most dominant in terms of heat transfer. However, once the initial phase of the process is complete and a fully formed melt pool is present, the majority of laser radiation is directed toward the melt pool, with only a small portion being absorbed by the powder particles at in front of the melt pool. At this point, the convective heat from the melt pool becomes a major

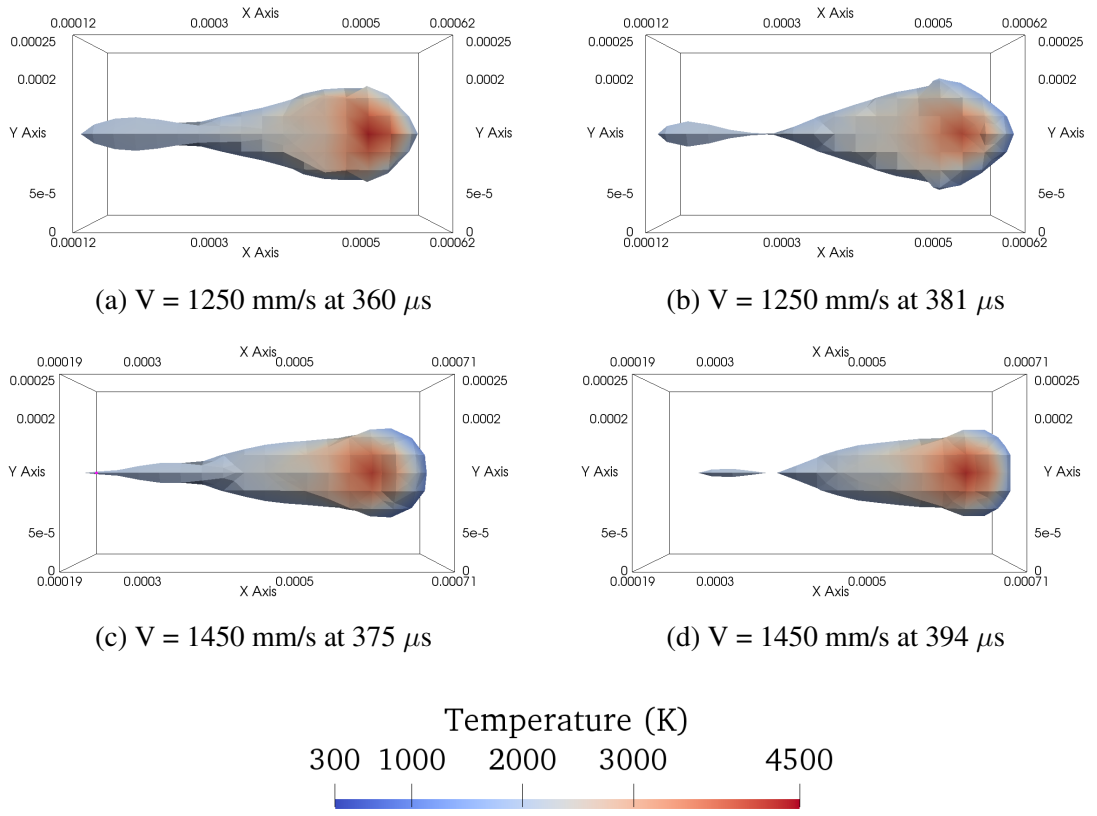

(a) V = 1250 mm/s at 360 μs

(b) V = 1250 mm/s at 381 μs

(c) V = 1450 mm/s at 375 μs

(d) V = 1450 mm/s at 394 μs

Figure 4.11: Demonstration of Plateau-Rayleigh instability in the melt pool with laser scan velocities of 1250 mm/s (a and b) and 1450 mm/s (c and d) for the validation case

heat source for the powder bed. Figure 4.12 shows the variation of convective heat and the laser heat absorbed by the powder bed during the simulation. As described in section 4.5.1, when the scan velocity of the laser is increased (V = 1450 mm/s), the powder bed experiences a higher heat input from the laser. Nevertheless, the convective heat transfer between the melt pool and powder particles remains nearly constant. The rate of convective heat transfer is directly linked to the size of the melt pool. At higher scan velocities, the melt pool becomes longer but narrower. Hence, overall, the convective heat transfer rate is almost equal in the two scenarios.

Figure 4.13 shows the temperature distribution (4.13a) and convective heat transfer (4.13b) of the particles in the powder bed. The melt pool is shown as an opaque red region. The laser beam is located at the front edge of the melt pool. A distinct difference can be observed when comparing the width of the melt track immediately behind the laser beam spot with its width further back. This variation in melt track width can be attributed to convective melting of the powders due to the heat transferred from the back edge of the melt pool, which is still hotter than the particles. Although the region immediately behind the laser is depleted due to laser radiation, the area adjacent to the back of the melt pool continues to receive heat from the melt. Therefore some of these particles also melt and add to the melt track width. This shows the significance of melt pool shape on powder melting.

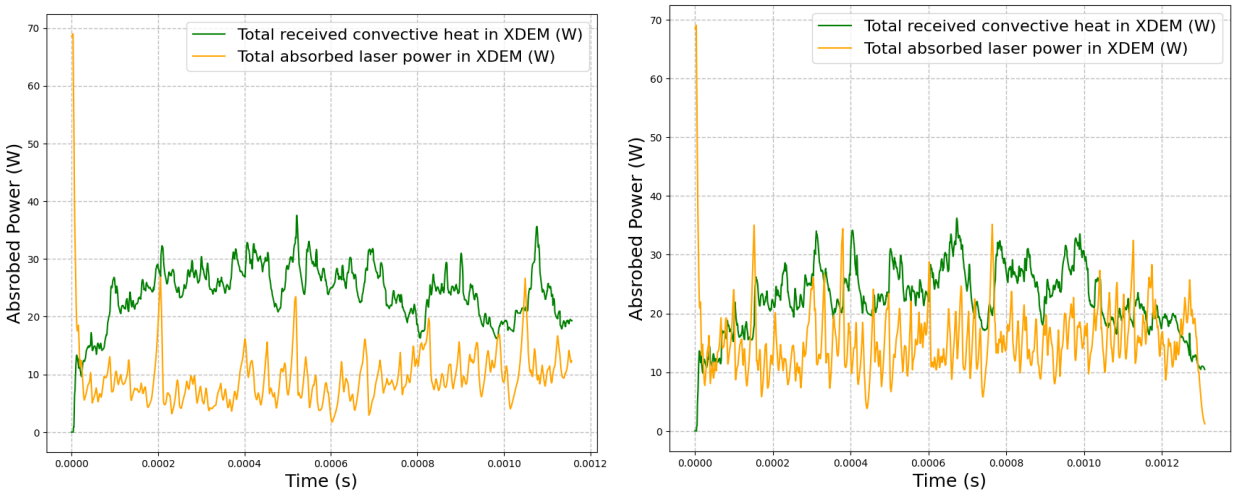

(a) V = 1050 mm/s

(b) V = 1450 mm/s

Figure 4.12: Variations of total convective heat transfer between the powder bed and the melt pool and the total absorbed laser power by the powder bed at two different scanning velocities

Expanding the melt pool to the sides, whether due to undulations or external forces like Marangoni, heats up particles on the sides. This increases the chance of uniform fusion between adjacent tracks.

The convective heat flow rate of particles is illustrated in Figure 4.13b. The figure demonstrates that particles in direct contact with the melt pool display a positive rate of convective heat, which indicates that they are being heated up by the melt pool. At the front edge of the melt pool, one or two particles exhibit a negative convective flow rate, indicating that they are losing heat to the CFD cells. This suggests that the center of the particle is positioned outside the melt, resulting in the heating of the surrounding gas. The particles located further back in the melt track are in thermal equilibrium with their surrounding gas and solid, and therefore they only receive or lose a negligible amount of heat.

Figure 4.14 demonstrates the temperature distribution over the powder bed for two different laser scan velocities at a certain time of simulation. It is is observable that melt pool in the case with higher scan velocity is longer (280 μm vs 230 μm) but narrower (119 μm vs 150μm) compared to scan velocity of 1050 mm/s. It is evident that the narrower melt width has led to a narrower melt track. However, the higher instabilities of the melt pool at higher scan velocities, as discussed in section 4.5.2, have resulted in less consistency of the melt pool, causing it to expand disproportionately wider than usual at certain points, such as near x = 0.0008 m and x = 0.0005 m. At these locations respectively the left (at x = 0.0008 m) and right (x = 0.0005 m)of the melt track has dented into the powder bed for about 2 to 3 powder diameters. Whereas such sudden dents in the melt track is not observed at scan velocity of 1050 mm/s (Figure 4.14a).

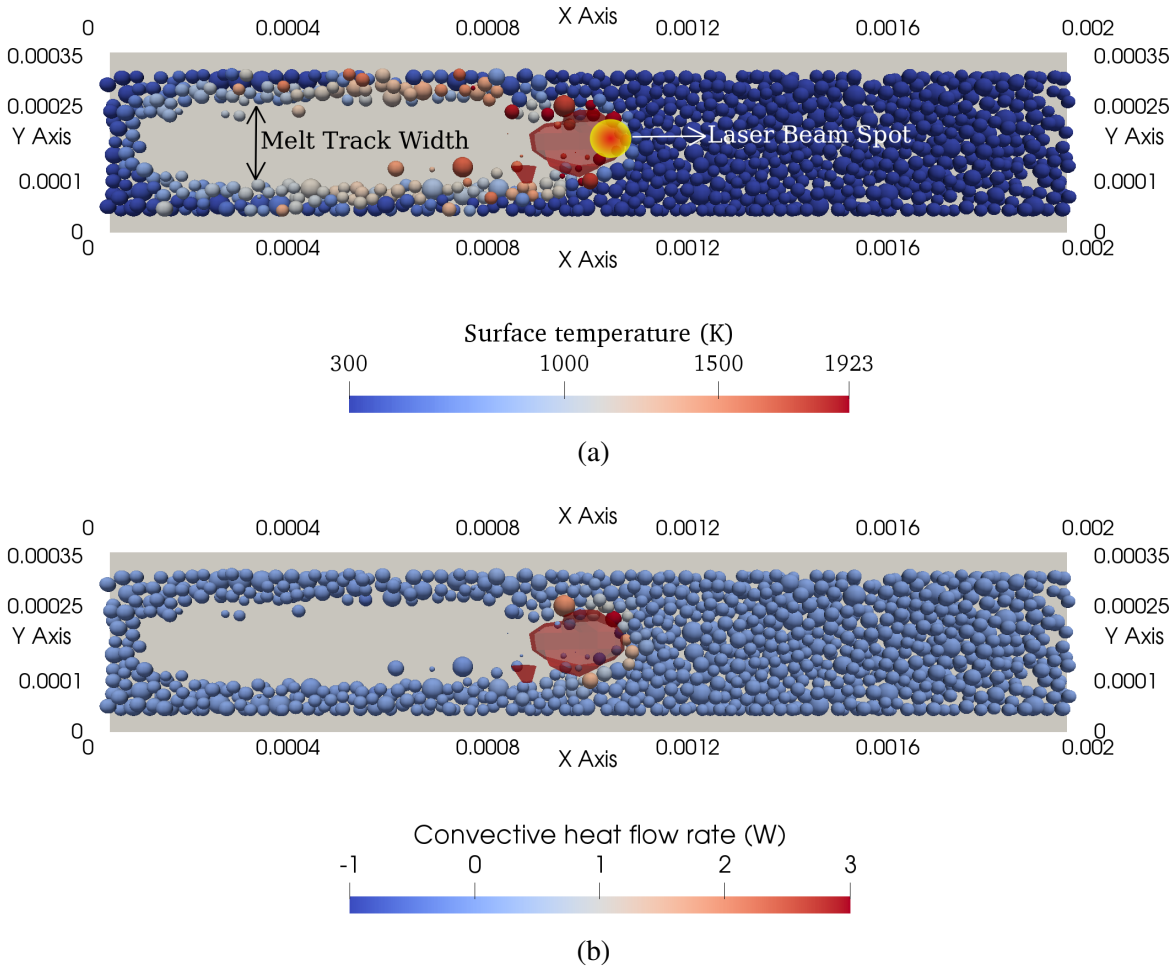

Figure 4.13: Temperature distribution (a) and convective heat rate distribution (b) over the powder layer in the simulation with laser scan velocity of 1050 mm/s at t = 900 μs. The melt pool is shown a an opaque red region.

4.6 Conclusion

In this study, a thermally coupled computational fluid dynamics-discrete element method (CFD-DEM) model for SLM process was developed. The model incorporated the VOF method to predict the formation and morphology of the melt pool. The accuracy of the numerical model was verified against experiments and lumped simulations, demonstrating good agreement with them. The formation and morphology of the melt pool were investigated for four different laser scan velocities, and the results indicated that higher scan velocities resulted in thinner and longer melt pools. Furthermore, it was demonstrated that at higher scan velocities, the Plateau-Rayleigh instability became dominant and caused stronger undulations in shape of the melt pool.

One novel contribution of this research was providing close insights into the heat transfer among the particles. Temperature distribution and convective heat transfer rate over the powder layer for all

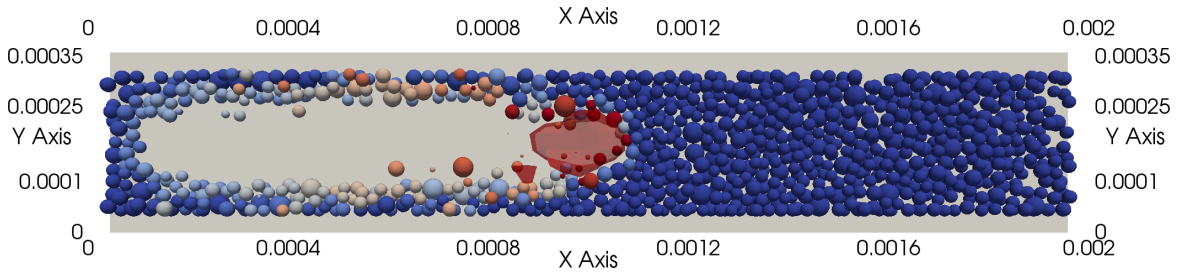

(a) Laser scan velocity of 1050 mm/s

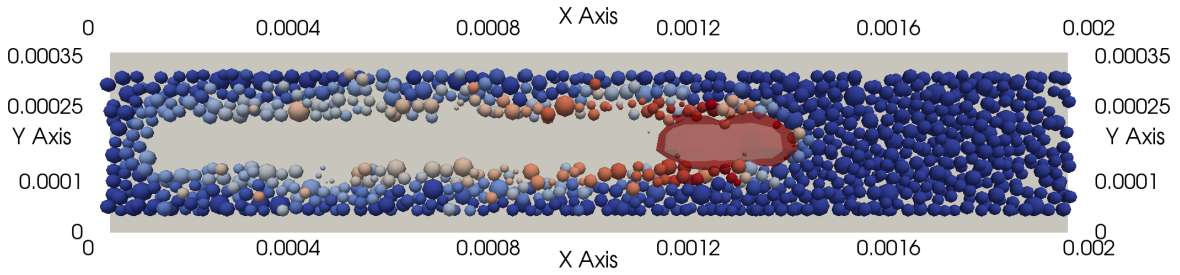

(b) Laser scan velocity of 1450 mm/s

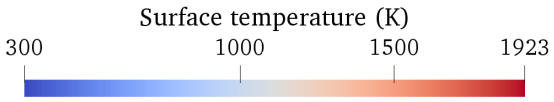

Figure 4.14: Temperature distribution over the scanned powder layer at t = 900 μs for two different scan velocities

the cases were presented and discussed. It was shown that the total convective heat transfer of the powder layer with the melt pool was at the same order of magnitude as the heat received from the laser by the powder layer, suggesting its significant effect on the evolution of the melt pool. These insights can help in the optimization of the SLM process by controlling the heat transfer mechanisms and improving the quality of the printed parts. Overall the thermally coupled CFD-DEM approach towards simulation of selective laser melting demonstrates promising potential for achieving precise outcomes and providing valuable insights into the process.

Chapter 5

Three-dimensional CFD-DEM Simulation of Raceway Transport Phenomena in a Blast Furnace[1]

5.1 Abstract

Improving energy efficiency in a blast furnace (BF) has a significant effect on energy consumption and pollutant emission in a steel plant. In the BF, the blast injection creates a cavity, the so-called raceway, near the inlet. On the periphery of the raceway, a ring-type zone is formed which is associated with the highest coke combustion rate and temperatures in the raceway. Therefore, predicting the raceway size or in other words, the periphery of the ring-type zone with accuracy is important for estimating the BF's energy and coke consumption. In the present study, Computational Fluid Dynamics (CFD) is coupled to Discrete Element Method (DEM) to develop a three-dimensional (3D) model featuring a gas-solid reacting flow, to study the transport phenomena inside the raceway. The model is compared to a previously developed two-dimensional (2D) model and it is shown that the assumptions associated with a 2D model, result in an overestimation of the size of the raceway. The 3D model is then used to investigate the coke particles' combustion and heat generation and distribution in the raceway. It is shown that a higher blast flow rate is associated with a higher reaction

[1]This chapter is written based on the following published paper: Aminnia, N., Adhav, P., Darlik, F., Mashhood, M., Saraei, S.H., Besseron, X. and Peters, B., 2023. Three-dimensional CFD-DEM simulation of raceway transport phenomena in a blast furnace. Fuel, 334, p.126574.

rate and a larger raceway. A 10% increase in the inlet velocity (from 200 m/s to 220 m/s) caused the raceway volume to grow by almost 40%. The DEM model considers a radial discretization over the particle, therefore the heat and mass distributions over the particle are analyzed as well.

5.2 Introduction

The ironmaking industry produces 7% of the world's total carbon dioxide emissions [143]. The most frequent ironmaking process is the blast furnace (BF), accounting for more than 70% of total energy consumption in the ironmaking industry [144] and 90% of the $CO2$ emission [145]. As a result, lowering energy usage and gas pollution in the BF ironmaking operations has received a lot of attention [146].

The region inside the furnace which is created by injecting hot blast air into the coke bed is called the raceway. Its shape is affected by different parameters such as blast velocity, the geometry of the nozzles, and operational circumstances [147]. Therefore, the study of the raceway is vital to analyze the gas species distributions and heat supplies which, directly have an impact on the furnace's productivity and efficiency. As a result, the raceway has been comprehensively studied, especially the principles of the particle scale. Experimental and computational methods have been used extensively to study raceway phenomena over the past few decades. As a consequence of the severe operating circumstances within the actual BF process (e.g., high temperature and pressure situations), measurement during an experimental test is difficult to undertake and only a few studies have worked on this with very limited data, such as gas species distributions [148]. For example, Matsui et al. [149] used microwave reflection gunned via a tuyere to study the BF raceway formation under heavy coal injection rate circumstances. Sastry et al. [150] studied the particle system in a two-dimensional (2D) cold model. In another study, Sastry et al. [151] conducted experimental research in a packed bed and found that the characteristics of coke particles had a significant impact on cavity development and breakdown. Zhang et al.[152] used an image-based flame detection approach to investigate the combustion characteristics of a BF raceway and discovered that the raceway temperature profile could fluctuate considerably. These experimental studies despite helping us gain a better picture of how raceways work can only explain BF functioning at the macro-scale information such as pressure and temperature in the local spots and are not able to obtain the micro-scale information such as inter-particle/phase interactions, raceway shape/size, heat transfer, coke combustion.

In light of the limitations of experimental research and the difficulty of performing accurate measurements, numerical simulations are generally employed to study raceway phenomena. Numerical simulations are divided into two common categories: Eulerian-Eulerian and Eulerian-Lagrangian. Mondal et al. [153] studied the influences of the air blast velocity on the shape and size of the

raceway zone in a BF by using the Eulerian-Eulerian model. However, the Eulerian-Eulerian model has no capacity of obtaining information such as particle and phase interactions, particle residence time, and particle trajectory [154]. Besides the simple assumptions of inter-particle collisions in this method make it difficult to adequately capture numerous interparticle collisions near the tuyere and the quasi-static-regime in the deadman region and the associated flow features[155]. Such difficulties can be overcome by one of the important Eulerian-Lagrangian methods, the discrete element method (DEM) coupled with Computational Fluid Dynamics (CFD) named CFD-DEM. In recent years, many studies have applied CFD-DEM methods to investigate the raceway's information. For example, Xu et al. [156] proposed CFD-DEM methods to study gas fluidization on fixed and fluidized beds. To comprehend raceway formation, they illustrated that this method can capture gas-solid flow characteristics ranging from large scale (such as processing equipment) to little scale features (such as each particle). Feng et al. [157] developed a 2-dimensional model to study the particle flow in the modeling of BF, finding that both solid and gas phases flow are changed spatially and temporally, in particular in the cohesive zone, which is affected by the layered ore and coke particle structure. Yuu et al. [158] compared the characteristics of the raceway such as depth and heights with experimental data and additionally reported dynamic characteristics such as the flow of solid particles, and the airflow around the raceway. Hilton and Cleary [159] used a discrete approach and observed the effect of injection velocity and bed pressure on the formation of raceway and investigate those non-spherical particles, as opposed to spherical particles, can form the raceways at higher gas input velocities. Wang and Shen [160] developed a reacting model to study raceway formation at the particle scale and discussed the impacts of several factors on raceway combustion (such as inlet velocity, temperature, and oxygen mass fraction). To examine raceway formation, Miao et al. [161] published a 2D CFD-DEM model for full-scale BF conditions and showed that in comparison to the studies in the laboratory circumstance, the raceway parameters are substantially more complicated in full-scale BF. Cui et al. [162] used a particle scale CFD-DEM method to study the raceway cavity shape and its parameters such as heat source, mass source, and chemical reactions and additionally the effect of the gas inlet velocity, size of particles, and particle discharge rate on the raceway formation. Dianyu et al. [163] also developed a 2D CFD-DEM model to analyze the effect of parameters such as particle size and oxygen enrichment on raceway formation and gasification rate. Recently, there has been an increasing interest in operating furnaces using renewable fuels, such as hydrogen, and many researchers have used CFD simulations to prove their efficiency[164, 165, 166]. Though this study does not consider renewable fuels, its findings can be applied to such endeavors.

The present study emphasizes the superior ability of 3D models over 2D models to predict the behavior of raceways. Therefore a 3D particle-scale CFD-DEM model of a BF raceway is developed. Using radial discretization, heat and mass transfers within particles are solved, therefore the internal

gradients of particles are seen. The developed model incorporates oxidation reactions within the particles and heat and mass transfer between particles and the gas. Additionally, the impact of parameters such as inlet velocity and particle mesh on raceway size and temperature distribution is discussed. In section 5.3 the governing equations of CFD and DEM models are presented along with the details of coupling techniques. In section 5.4 the results of the validation of the 3D model is presented. Then, using the comparisons between the 2D and 3D models it is argued that the inherent assumptions associated with 2D models make it unable to predict the raceway dynamics with precision. In the same section the results from the 3D model are presented and discussed. It is also shown that the discretization of the particles in the DEM model can have significant effect on the predicted size of the raceway and the gas temperature.

5.3 Method

XDEM software[97] is used in the current work. This software uses Lagrangian-Eulerian approach to for CFD-DEM coupling. Its multi-scale and multi-physics framework considers particles as discrete entities while fluid as a continuous medium.

5.3.1 Governing equations for discrete particles

XDEM predicts both dynamics and thermodynamics of the particulate system. The particle position, velocity and acceleration are calculated with the dynamics module of the XDEM, where as the temperature, and processes like combustion, gasification, drying etc are calculated with the conversion module of the XDEM.

5.3.1.1 Dynamics module

The Discrete Element Method (DEM) used in the dynamics module of XDEM is based on the soft sphere model. In this method, it is assumed that the particles are deformable and can overlap each other, where the magnitude of overlap is decided by the contact force using the force-displacement law. The hardness of the particle is expressed via Young's Modulus, while the particle energy dissipation is described with dampener and/or dashpot. The translational and rotational movements of individual particles are tracked using the classical mechanics equations. A detailed description of all the terms mentioned below could be found in previous work [98]. A summary of the translational and rotational motion equations is given below: Equations of particle motion:

$$m_i \frac{d\vec{v_i}}{dt} = m_i \frac{d^2\vec{X}_i}{dt^2} = \vec{F_i^c} + \vec{F_i^g} + \vec{F_i^{ext}} \tag{5.3.1}$$

Physical constants/Greek symbols

α	Heat transfer coefficient ($W/(m^2.K)$)
β	Interphase momentum exchange ($kg/(m^3.s)$)
ϵ	Porosity
λ_f	Thermal conductivity ($W/(m.K)$)
μ	Dynamic viscosity ($Pa.s$)
η	Weight of particle for porosity calculation
Ω_c	Implicitly treated drag term ($1/s$)
ρ	Density (kg/m^3)

Operators

∂	Differential operator (-)
Δ	Difference (-)
∇	Nabla operator (-)

Scalars

A	Surface Area
c_p	Specific Heat ($J/kg.K$)
C_d	Drag Coefficient (-)
d	Particle diameter (m)
h	Convective heat transfer coefficient ($W/(m^2.K)$)
I_i	Moment of inertia ($kg.m^2$)
m	Mass (kg)
m'	Mass source ($kg/(m^3.s)$)
p	Pressure (Pa)
q'	Heat source (W/m^2)
q''	Heat flux (W/m^2)
r, R	Radius (m)
Re	Reynolds number (-)
t	Time (s)
T	Temperature (K)
T_{final}	Length of simulation (s)
V	Volume (m^3)

Subscripts

c	Cell
$cond$	Conduction
d	Drag
eff	Effective values
f	Fluid
i, j	Particle
n	Normal direction
p, P	Particle
s	Solid
rad	Radiation
t	Tangential direction

Superscripts

n	Geometry exponent
(n)	n^{th} (time) step
$(n+1)$	n^{th} (time) step $+1$

First order tensors (vectors)

$\vec{A}_c$	Acceleration on fluid cell due to explicitly treated drag term (m/s^2)
$\vec{g}$	Gravitational acceleration (m/s)
$\vec{F^c}$	Contact Forces (N)
$\vec{F^g}$	Gravitational Force (N)
$\vec{F^{ext}}$	External Forces (N)
$\vec{F_B}$	Buoyancy Force (N)
$\vec{F_D}$	Drag Force (N)
$\vec{M}_{i,j}$	Torque generated by inter-particle forces ($N.m$)
$\vec{v}_f$	Fluid velocity field
$\vec{X}_i$	Positional vector (m)
$\vec{\omega}$	Rotational velocity (rad/s)

Table 5.1: Nomenclature

where $\vec{F_i^{ext}}$ is the sum of all the external forces acting on the particle, such as buoyancy forces $\vec{F_B}$ (Eq 5.3.25) and drag forces $\vec{F_D}$ (Eq 5.3.26).

$$I_i \frac{d\vec{\omega_i}}{dt} = \sum_{j=1}^{n} \vec{M_{i,j}} \tag{5.3.2}$$

5.3.1.2 Conversion module

The particles a modelled with pores/voids. These pores are modelled to have a gaseous mixture of different chemical species. Mass conservation equation for fluid within particles pores:

$$\frac{\partial}{\partial t}\left(\alpha_f \rho_f\right) + \vec{\nabla} \cdot \left(\alpha_f \rho_f \vec{v_f}\right) = m'_{s,f} \tag{5.3.3}$$

One dimensional transient energy conservation equations for particles:

$$\frac{\partial \rho c_p T}{\partial t} = \frac{1}{r_n}\frac{\partial}{\partial r}\left(r^n \lambda_{eff}\frac{\partial T}{\partial r}\right) - r^n\left(\vec{v}\rho_f c_{p_f} T\right) + \sum_{k=1}^{l} \dot{\omega_k} H_k \tag{5.3.4}$$

The mass balance and transport equation of individual fluid species within the particle pores:

$$\frac{\partial}{\partial t}\left(\alpha_f \rho_{f,i}\right) + \nabla \cdot \left(\alpha_f \rho_{f,i} \cdot \vec{v_f}\right) = \frac{1}{r_n}\frac{\partial}{\partial r}\left(r^n \alpha_f D \frac{\partial \rho_{f,i}}{\partial t}\right) + m'_{s,f,i} \tag{5.3.5}$$

Following boundary conditions are applicable to the governing equations mentioned above:

$$-\lambda_{eff}\frac{\partial T}{\partial r}\bigg|_{r=0} = 0 \tag{5.3.6}$$

$$-\lambda_{eff}\frac{\partial T}{\partial r}\bigg|_{r=R} = \alpha(T_R - T_\infty) + q''_{rad} + q''_{cond} \tag{5.3.7}$$

$$-D_{i,eff}\frac{\partial \rho_i}{\partial r}\bigg|_{r=R} = \beta_i\left(\rho_{i,R} - \rho_{i,\infty}\right) \tag{5.3.8}$$

In the Eq 5.3.7, q''_{cond} and q''_{rad} are conduction and radiation heat source respectively from the neighbouring particles. The detailed description of the conduction and radiation between particles is given in B. Peters [167].

In the conversion module of XDEM, a radial discretization is considered to solve for heat & mass transfer within the particle. This radial discretization can be uniform or non-uniform, as shown in fig 5.1. In the current work, non-uniform radial discretization is utilized. The non-uniform radial discretisation allows to have smaller cell length near the particle surface that allows the model to capture the sharp temperature and mass flow gradients.

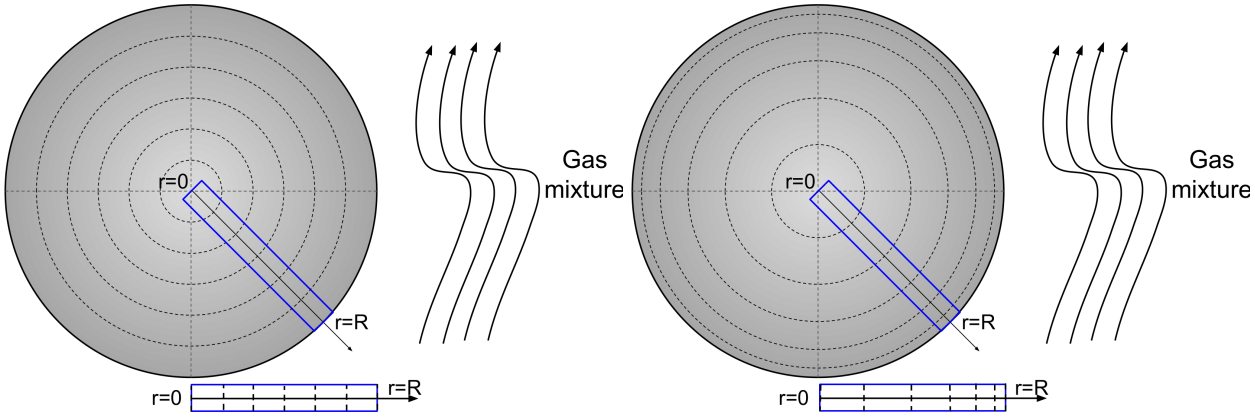

(a) Uniform discretization

(b) Non-Uniform discretization

Figure 5.1: Radial discretization for heat & mass transfer within a particle

5.3.2 Governing equations for fluid

In Eulerian volumetric average method, the conservation equation of mass (Eq 5.3.10), momentum (Eq 5.3.11) and energy (Eq 5.3.12) are written over a representative volume, where porosity (ϵ Eq 5.3.9) refers to the interstitial solid space particles. These governing equations for fluids are given below. Detailed description of the porosity calculation can be found in [98], the porosity calculation in brief is as follows, where V_c is CFD cell volume, V_i is the particle volume of i^{th} particle in the CFD cell and η is weight for porosity calculation:

$$\epsilon = 1 - \frac{1}{V_c}\sum_{i}^{n} \eta_i V_i \tag{5.3.9}$$

Conservation of mass

$$\frac{\partial}{\partial t}(\alpha\rho_f) + \nabla \cdot (\alpha\rho_f \vec{v}_f) = m' \tag{5.3.10}$$

Conservation of momentum

$$\frac{\partial}{\partial t}(\rho_f \vec{v}_f) + \nabla \cdot (\rho_f \vec{v}_f \vec{v}_f) = -\nabla p + \rho_f \vec{g} + \rho_f \vec{A}_c + \mu\nabla^2 \vec{v}_f - \rho_f \Omega_c \vec{v}_{f_c} \tag{5.3.11}$$

Conservation of energy

$$\frac{\partial}{\partial t}(\rho_f h_f) + \nabla \cdot (\rho_f \vec{v}_f h_f) = \frac{\partial p}{\partial t} + \vec{v}_f \cdot \nabla p + q' \tag{5.3.12}$$

Chemical reactions are also considered in the CFD solver. In a multispecies gas mixture, the mass conservation equation for a species i, is given in Eq 5.3.13:

$$\frac{\partial}{\partial t}\rho_{f,i} + \nabla \cdot (\rho_{f,i} \cdot \vec{v}_f) = m_i' \tag{5.3.13}$$

5.3.3 Chemical reactions

The current study focuses on the raceway and areas immediately next to raceway. In this region mainly gasification and combustion reactions are observed in the particles, the (solid phase) reactions are presented in Eq 5.3.14, 5.3.15, and 5.3.16. Considering the temperatures in and near raceway, the reaction 5.3.14 producing CO is mainly observed. Some small amount CO_2 is produced as shown in reaction 5.3.15, but due to high temperatures ($\geq$ 1073 K [168]) it quickly decomposes to CO as shown in gas phase reaction 5.3.16.
The gasification reactions are as follows:

$$\mathrm{C} + 0.5\,\mathrm{O_2} \rightarrow \mathrm{CO} \tag{5.3.14}$$

$$\mathrm{C} + \mathrm{O_2} \rightarrow \mathrm{CO_2} \tag{5.3.15}$$

$$\mathrm{C} + \mathrm{CO_2} \rightarrow 2\,\mathrm{CO} \quad \text{(Boudard's reaction)} \tag{5.3.16}$$

As opposed to the previous reactions, reaction 5.3.17 is taking place in purely gaseous state (handled by CFD solver). Due to the high temperatures in the region of interest, it is observed that the CO_2 produced from the following chemical reactions, converts back to CO according to reaction 5.3.16.

$$\mathrm{CO} + 0.5\,\mathrm{O_2} \rightarrow \mathrm{CO_2} \tag{5.3.17}$$

Generally reactions can be written as follows:

$$\sum_{i=1}^{N} \nu_i' R_i \rightleftharpoons \sum_{j=1}^{M} \nu_j'' P_j \tag{5.3.18}$$

where N denotes the number of reactants R_i, M denotes the number of products P_j and $\nu_{i/j}$ represents the absolute values of the corresponding stoichiometric coefficient.

$$\dot{\omega} = -\frac{1}{\nu_i'}\frac{dc_i}{dt} = \frac{1}{\nu_j''}\frac{dc_j}{dt} \tag{5.3.19}$$

The actual reaction rate $\dot{\omega}$ may depend on species concentrations, the available reactive surface O_{sp} and the temperature; so that in general $\dot{\omega} = f(c_i, c_j, O_{sp}, T, \ldots)$. Thus, an Arrhenius law is employed to describe the temperature dependency of the reaction rate as

$$k(T) = k_0\, e^{\left(\frac{-E_a}{RT}\right)} \tag{5.3.20}$$

where $k(T)$ represents the temperature dependent rate coefficient, k_0 referred to as frequency factor and E_a denotes the activation energy.

If thermodynamic equilibrium is reached, then an equilibrium constant $K_{\text{eq,c}}$, representing the thermodynamically equilibrium state, can be obtained as

$$K_{\text{eq,c}}(T) = \frac{k_f(T)}{k_b(T)} = \frac{\prod_{j=1}^{M} c_{\text{eq},P_j}^{\nu''_j}}{\prod_{i=1}^{N} c_{\text{eq},R_i}^{\nu'_i}} \tag{5.3.21}$$

In the XDEM software, the equilibrium constant $K_{\text{eq,c}}(T)$ is calculated as

$$K_{\text{eq,c}}(T) = e^{\frac{A_{eq}}{T} + B_{eq}} \tag{5.3.22}$$

where A_{eq} and B_{eq} are constant values that may come from existing tables or from equilibrium diagrams of phase diagrams.

Variable	Reaction 5.3.14	Reaction 5.3.17
E_a	$149,000$	$20,129$
A_{eq}	0	$2.24e+08$
B_{eq}	0	0
Temperature Range	$273K$ to $1500K$	

Table 5.2: Chemical reaction rates

5.3.4 CFD-DEM Coupling

The CFD-DEM coupling is achieved through conventional staggered approach. In this approach, the output from one simulation (solver) is used as an input for the other. Considering current work, assume that solver S_1 is the CFD solver, and the solver S_2 is DEM solver. The fluid solver S_1 solves the momentum, mass, reactions and energy equations for the fluid. The fluid solver output such as the fluid velocity, temperature, species mass fraction etc., are then used as boundary conditions for the particles in DEM solver S_2. The DEM solver S_2 uses solution from CFD solver, to compute various source terms by computing the momentum and energy equations for particles. In the next time step, these source terms are communicated to the fluid solver S_1, which then uses the solution from n^{th} time step to get a new solution for the $(n+1)$ time step.

$$x_2^{(n+1)} = S_1^{(n)}\left(x_1^{(n)}\right) \tag{5.3.23}$$

In Eq 5.3.23, CFD solver S_1 uses old time step's boundary value (or in case of first time step it can be the boundary conditions or an initial guess), $x_1^{(n)}$to compute the values of x_2 for next time step

$x_2^{(n+1)}$. During this time, DEM solver S_2 waits for CFD solver S_1 to compute solution and exchange the updated solution $x_2^{(n+1)}$.

$$x_1^{(n+1)} = S_2^{(n)}\left(x_2^{(n+1)}\right) \tag{5.3.24}$$

In Eq 5.3.24, the updated solution x_2 is used to update the solution for x_1 for the next time step. This can also be seen graphically in Fig 5.2.

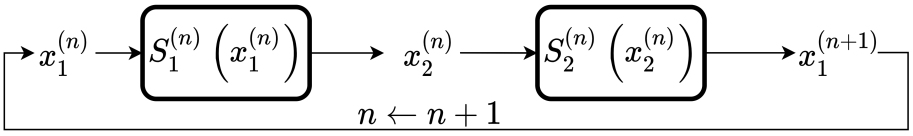

Figure 5.2: Serial Staggered Coupling Scheme

5.3.4.1 Fluid forces on particles

There are two types of fluid forces acting on the particles, namely hydrostatic force and hydrodynamic force. The hydrostatic force is the buoyancy force which accounts for the pressure gradient around an individual particle [169].

$$\vec{F_B} = -V_{p_i}\nabla p \tag{5.3.25}$$

In the Eulerian-Lagrangian approach, the hydrodynamic force corresponds to the fluid-particle interaction. This force depends on the relative velocity of the solid particle and fluid along with the forces acting due to presence of neighbouring particles. The drag force acting on the particle due the fluid for CFD-DEM approach is given as follows:

$$\vec{F_D} = \frac{\beta V_p}{(1-\epsilon)}\left(\vec{v}_f - \vec{v}_p\right) \tag{5.3.26}$$

The interphase momentum exchange β is predicted according to Gidsaw [170]. Although to cover all range of void fraction (ϵ), Wen and Yu [171] ($\epsilon \geq 0.8$) and Ergun and Orning [172] ($\epsilon < 0.8$) equations are included.

$$\beta = \begin{cases} 150\dfrac{(1-\epsilon)^2}{\epsilon}\dfrac{\mu_f}{d_p^2} + 1.75(1-\epsilon)\dfrac{\rho_f}{d_p}|\vec{v}_f - \vec{v}_p|, & \text{if} \quad \epsilon < 0.8 \\ \dfrac{3}{2}C_d\dfrac{\epsilon(1-\epsilon)^2}{d_p}\rho_f|\vec{v}_f - \vec{v}_p|\epsilon^{-2.65}, & \text{if} \quad \epsilon \geq 0.8 \end{cases} \tag{5.3.27}$$

where the drag coefficient C_d is given as:

$$C_d = \begin{cases} \dfrac{24}{Re}\left[1 + 0.15(Re)^{0.687}\right], & \text{if} \quad \text{Re} < 1000 \\ 0.44, & \text{if} \quad \text{Re} \geq 1000 \end{cases} \tag{5.3.28}$$

and the Reynolds number for the particle is given as:

$$Re = \frac{\epsilon \rho_f |\vec{v}_f - \vec{v}_p| d_p}{\mu_f} \tag{5.3.29}$$

5.3.4.2 Particle momentum source terms

In the fluid, the drag exerted by the solid particles is treated in semi-implicit way according to the method proposed by Xiao and Sun[138]. The explicit momentum source term $\vec{A}_c$ and implicit momentum source term Ω_c are as given in Eq 5.3.30

$$\vec{A}_c = \frac{1}{\rho_f V_c} \widetilde{\sum\sum}_i B_i \vec{u_{p_i}}, \quad \Omega_c = \frac{1}{\rho_f V_c} \sum_{i=1}^{c_n} B_i \tag{5.3.30}$$

5.3.4.3 Particle heat and mass source terms

Fluid flow conditions such as fluid temperature, specific heat, thermal conductivity, species mass fractions are exchanged from CFD to DEM. These are used as boundary conditions for solving energy balance, mass balance and reaction equations for particles.

Based on the energy balance equations, heat loss/gain due convection or due to change in composition of particles is computed. This is used as the (explicit) heat source in fluid energy equation. Similarly, mass source and species mass fraction source are computed.

$$q'_i = h_i A_i (T_{p_i} - T_f) \tag{5.3.31}$$

where h_i is the heat transfer coefficient for a given particle i, which is a function of Re, Pr, λ_f, d_p and cell porosity.

As there are different phenomenon driving mass transfer, such as evaporation, mass flux due to the gradient of species concentration, species production due to chemical reactions, a generalised way to represent individual species mass source is as follows:

$$m'_{s,f,i} = (\text{Area of Mass Transfer}) \times (\text{Mass Transfer Coefficient}) \times (\text{Driving Force}) \tag{5.3.32}$$

The total mass transfer is summation of all the species mass transfer terms.

$$m' = \sum_i m'_{s,f,i} \tag{5.3.33}$$

5.3.5 Computational Procedure

A schematic for the CFD-DEM coupling is shown in fig 5.3. For the , XDEM and OpenFOAM libraries are linked together as a single executable. The simulations starts after running the executable.

In the first step, DEM is initialized, where all the particles, walls, domain and XDEM mesh are created. After creating the mentioned assets, initial boundary conditions for the particles are applied. An initial porosity (ϵ) field is computed. Next CFD is initialized, where geometry and mesh is generated, boundary conditions on the fluid domain are applied, as well as porosity is made available to CFD solver, so that CFD solver takes into account the presence of particles from the first time step itself. But, these particles do not contribute to any heat or mass source terms of the fluid governing equations at the first time step. After all the required initializations, the time loop starts. The fluid governing equations are solved by the CFD solver developed with the assistance of OpenFOAM. The data transfer between DEM and CFD is done via direct read/write in memory. All the data is stored on the OpenFOAM mesh. After exchanging the data from CFD to DEM, the CFD data is used as boundary conditions for the particles. XDEM then solves the governing equations for the particles, and writes output fields such as porosity, momentum, heat, mass and species mass fraction source. After writing the data, the time loop proceeds to next time step ($T + dT$). In this time step, the data written by XDEM i.e various source terms, are injected in fluid governing equations. In this way the simulation continues until the specified end time T_{final}.

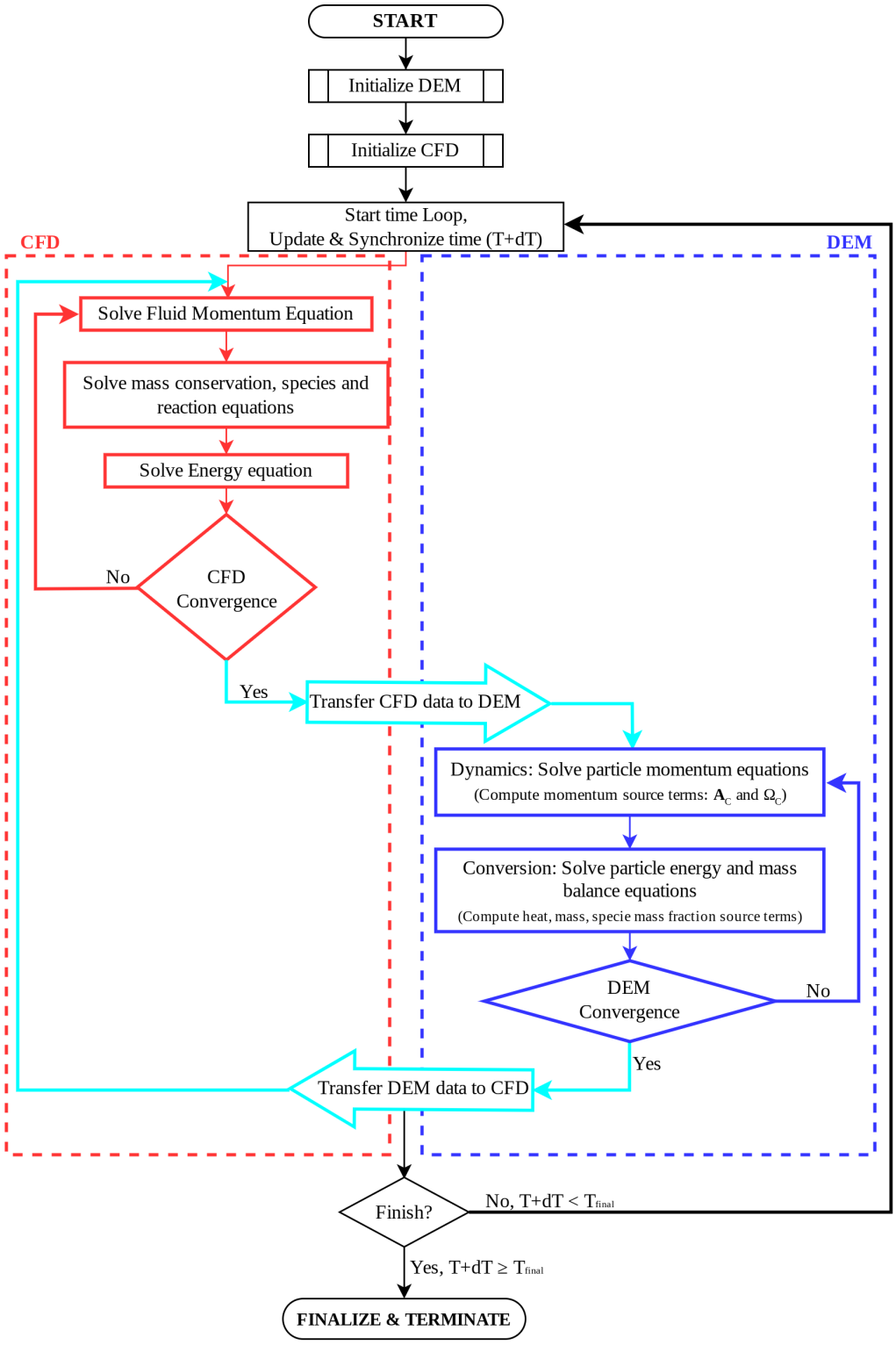

Figure 5.3: Flow chart of coupled OpenFOAM-XDEM solver showing calculation steps and exchange of data

5.3.6 Simulation setup

For the simulations presented, the region of interest is only the raceway, and not the whole BF. The raceway is modelled as a 3D box of dimension $0.6m \times 0.6m \times 1.5m$. For the 2D case the cross-section dimensions remain the same ($0.6m \times 1.5m$).

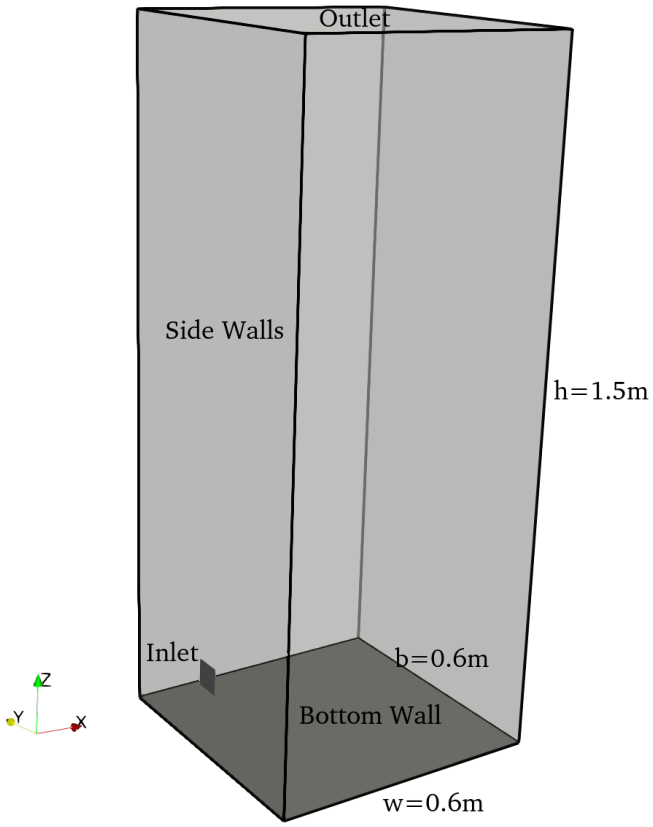

Figure 5.4: Simulation geometry and Boundaries

The boundary conditions for the CFD and DEM are described in the Table 5.3 and 5.4 respectively. It is assumed that the particles are preheated to 1300 K and the inlet air enters at a temperature of 1500 K. Since the primary purpose of this research is to demonstrate the effects of 3D simulations and particle discretization, the particles are spherical and of the same size to eliminate particle shape and size effects.

Variable	Value
2D grid	20×50 1000 Hex elements
3D grid	$20 \times 20 \times 50$ $20,000$ Hex elements
Inlet Specie Mass fraction	
CO	$0.00\,[-]$
CO2	$0.00\,[-]$
N2	$0.79\,[-]$
O2	$0.21\,[-]$
Specie Mass fraction inside simulation domain	
CO	$0.0\,[-]$
CO2	$0.0\,[-]$
N2	$0.79\,[-]$
O2	$0.21\,[-]$
Time step length	$0.005\,s$
Simulated Time	$20.0\,s$
Temperature	
Inlet	$1500\,K$
Internal Domain	$1500\,K$
Turbulence Model	$k-\epsilon$ Reynold's Averaged Simulation (RAS)

Table 5.3: Simulation conditions for CFD

5.4 Results and Discussions

5.4.1 Model validation

As it was explained in section 5.3, the CFD-DEM model used in this study is developed by coupling a CFD model in OpenFOAM and a particle system model in XDEM. The validations of the coupling have been presented in previous studies [97, 173]. For verifying the particle-scale reaction models and gas-solid reactive interactions, the resulting gas composition from the 3D model is validated against an experimental hot model[174].

Figure 5.5 shows the comparison of the simulation results for oxygen, nitrogen, and carbon monoxide against the experimental measurements. The results show that the model can predict the trend in coke combustion (oxygen consumption and carbon monoxide production) to an acceptable degree. However, there is a deviation between the predicted and measured values for oxygen and carbon monoxide which suggests and underestimated reaction rate for the coke combustion. The same level of deviation was also observed in previous studies [174, 163]. This deviation is rendered as acceptable considering the harsh measurement conditions inside the furnace and thus

Variable	Value
Particle Shape	Spherical
Particle Diameter	$0.01\,m$
Particle Density	$1111.1\,kg/m^3$
Particle Initial Temperature	$1300K$
Particle Composition	
Char (Solid)	$0.97\,[-]$
Light Ash (Solid)	$0.03\,[-]$
Number of particles	$10,000$
Particle radial discretization	5 uniform cells
Time step length	$0.005\,s$
Simulated Time	$20.0\,s$
Mechanical Properties	
Contact Model	Hertz Mindlin
Spring Constant	$100.0\,kN/m$
Viscous Contact Damping	$2420000.0\,N.s/m$
Friction Coefficient	$0.8\,[-]$
Poisson's Ratio	$0.45\,[-]$
Young's Modulus	$500000.0\,Pa/MPa$
Thermal Properties	
Thermal Conductivity	$0.47\,W/m.K$
Specific Heat	$1500\,J/kg.K$
Molar Mass	$30\,[-]$

Table 5.4: Simulation conditions for DEM

the uncertainty associated with the measurements.

5.4.2 Comparison of 2D and 3D simulations of raceway

First, we propose to study the differences between 2D and 3D simulations of the raceway. The 2D model is presented in a previous work [173]. As mentioned before, there have already been a lot of efforts in developing 2D models of the raceway and the BF. Simulations in 2D have the advantage of lower computational cost, but they come at the expense of numerical accuracy. Undoubtedly there should be a reasonable trade-off between the advantages and disadvantages. In the present work, 2D and 3D simulations are compared and the results reveal a significant discrepancy in raceway behavior. In order to make a valid comparison, the 2D and 3D cases were similar in size and mesh in the x and z direction. There are also similar initial conditions, including packed bed height and particle size.

Figure 5.6 shows the comparison of the raceway cavity in 2D and 3D simulations of the dynamics of a BF raceway. It can be observed that in 2D, the raceway cavity has larger dimensions compared

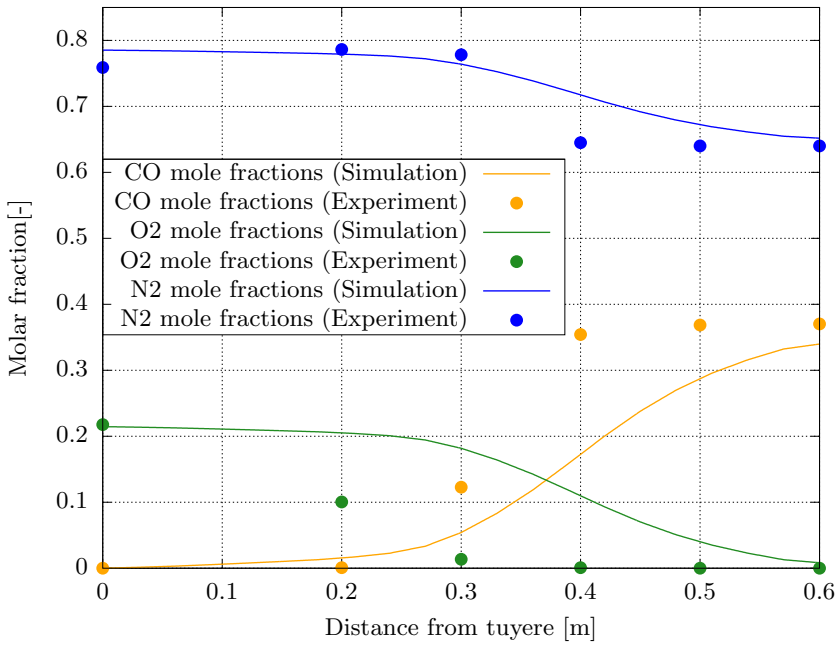

Figure 5.5: comparison of the measured and predicted gas compositions along the central axis of the tuyere

to the 3D results. The height and width of the raceway in the 2D case are respectively 100 cm and 38 cm, while in 3D they are respectively 30 cm and 12 cm. This notable discrepancy between the 2D and the 3D simulations can be explained by the fact that in 3D, the momentum of the inlet flow is partly consumed to expand the raceway in the third direction, depth (which reaches up to 24 cm). Whereas in 2D simulation the momentum of the inlet air is wholly saved to expanding the raceway height and width, thus resulting in an unjustifiably large raceway. The result is that in the 2D simulation, the packed bed is expanded to fill the whole available domain whereas in reality the top of the packed bed is just raised a fraction of the packed bed height. This behavior can be observed in the previous study as well [163]. This phenomenon can be confronted by defining different initial or boundary conditions to constrain the packed bed height or fill the whole domain from the beginning but nevertheless, it would not change the fact that the dynamics of the packed bed and the raceway are misrepresented.

Moreover, the implicit assumption made for the 2D model by itself leads to a significant gap between the model and actual physics. The 2D simulation of the raceway assumes a symmetrical placement of the raceway in the BF. For 2D simulation to represent the real BF raceway, either the BF should be a thin slice with two raceways on the opposite sides, which is naturally far from the reality, where we have a cylindrical furnace with multiple injection inlets located on the periphery; or, the inlet of the raceway should be an open slit covering the periphery which would lead to a torus raceway in the whole furnace. None of these two cases mimick the actual physical geometry

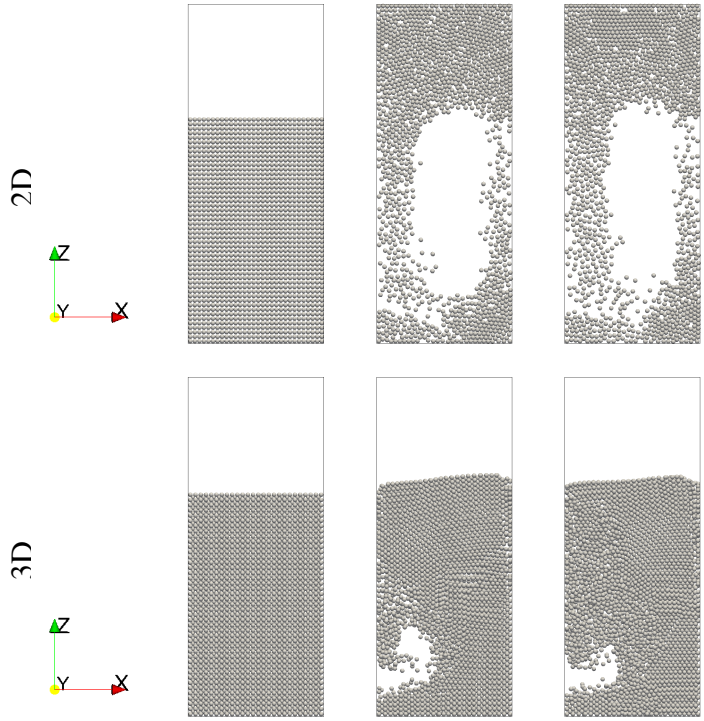

(a) t=0s (b) t=1s (c) t=5s

Figure 5.6: The 2D and 3D dynamics simulation of a blast furnase raceway at three different time steps. The 3D results are slices from the 3D packed bed cut between two XZ planes on the two sides of the inlet

to a good approximation. Due to such observations, the previous studies have noted [155] that there should be special boundary conditions defined on the domain for the 2D or quasi-3D model to represent the physics better.

However, in a 3D simulation, the actual physics of the problem is represented more accurately. As is presented in the following sections, the raceway enlargement is more confined and the packed bed movement is very limited compared to a 2D simulation. Therefore, the significant difference between the two cases led to the conclusion that 3D simulations, despite their computational costs, provide a much more reliable insight into the physics of the raceway. Additionally, with the increasing trend in computational power and thanks to parallelization, 3D simulations are becoming more affordable.

5.4.3 Typical transport phenomena of the raceway

Figure 5.7 provides a series of snapshots from the 3D simulation of a raceway section in an operating BF. The pictures depict the raceway formation as a hot air blast is injected horizontally into the furnace via the tuyeres. Following the blast, the raceway forms in the early time steps. It

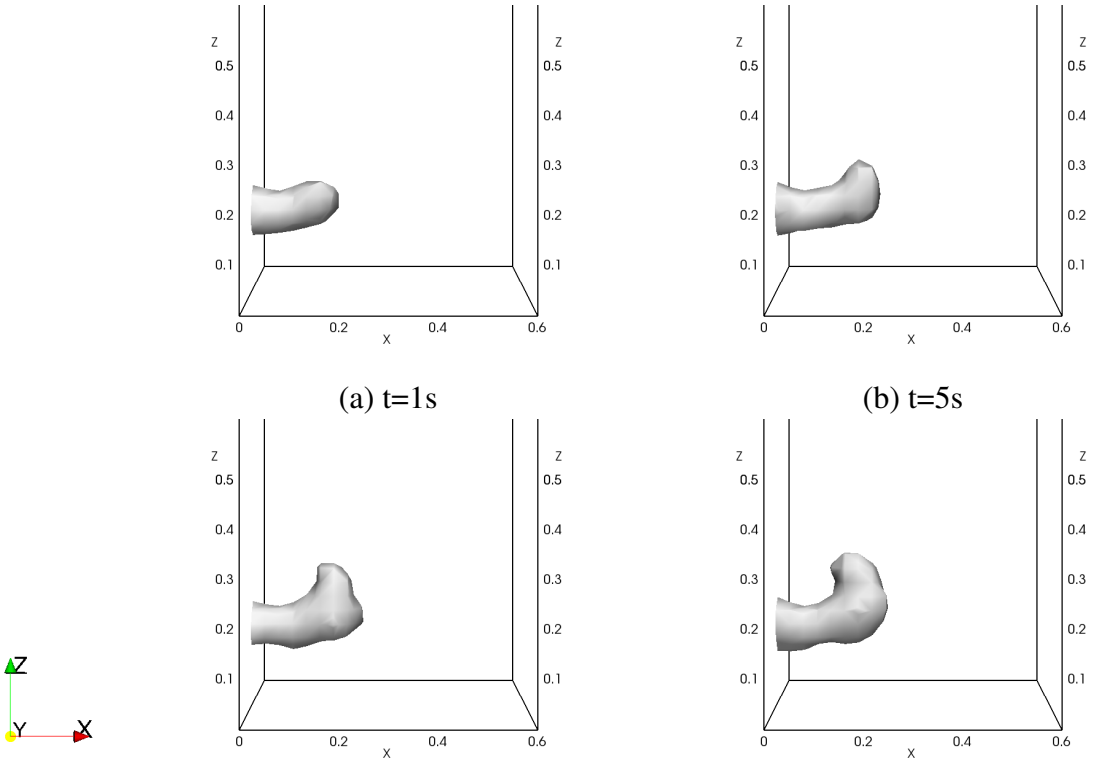

(a) t=1s (b) t=5s

(c) t=10s (d) t=20s

Figure 5.7: Topological evolution of the raceway cavity at different time steps in the 3D simulation of a BF raceway with a blast velocity of 200 m/s

first penetrates the packed bed to the maximum possible depth in a horizontal direction which is approximately 24 cm, then adopts an upward anti-clockwise direction to develop further in height and eventually reach a maximum height of 33 cm from the bottom of the furnace. As can be seen in the figures, by the time of 20 s the raceway has already adopted a respectively steady shape and dimensions. Figure 5.8 shows the penetration profiles of the raceway through time in X-direction (depth), Z-direction (height) and Y-direction (width). This plot supports the observations in figure 5.7, by showing that the raceway dimensions achieve stability in all directions by 20 s, despite abrupt fluctuations in the beginning. However, the width of the raceway shows less stability because it is comparatively confined by the walls.

As a more clear depiction of the 3D case, figure 5.9 shows the location of the raceway and the gas flow streamlines that start from the inlet and spread all through the raceway. As can be seen in the figure, the gas flow has a high velocity inside the raceway (more than 50m/s) and as it penetrates into the packed bed, loses its momentum and its velocity decreases drastically.

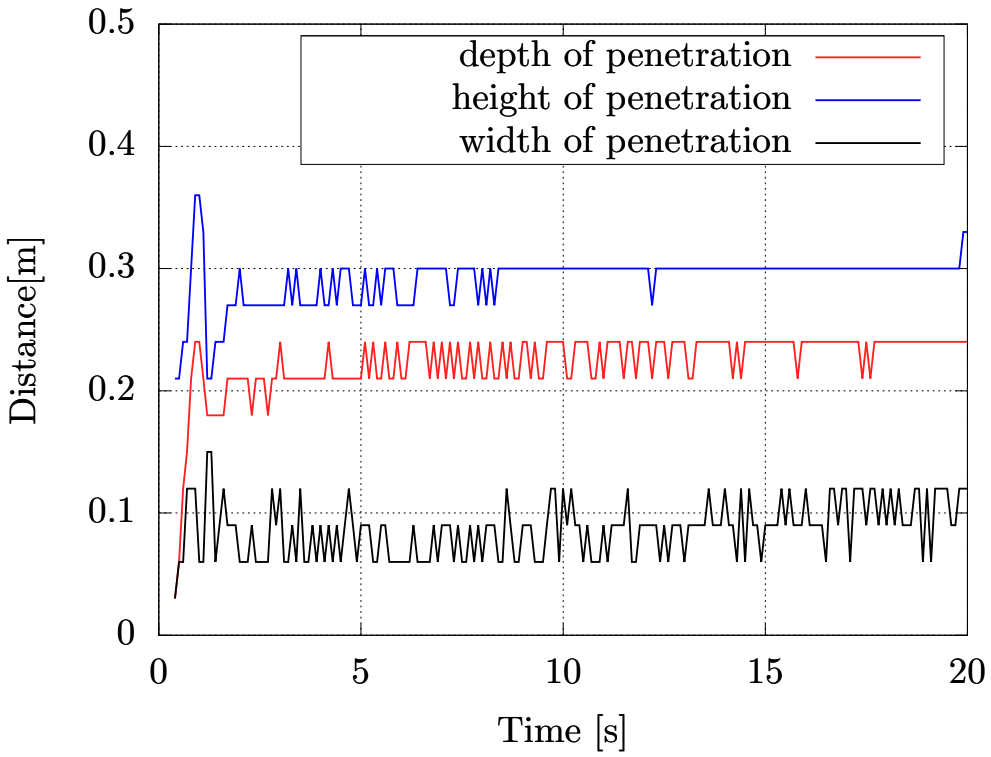

Figure 5.8: Temporal variation in depth (starting from tuyere tip in the direction of inlet flow, i.e., inlet central line) , height (starting from the bottom of the furnace in the positive z-direction) and width (starting from inlet center line in the positive y-direction) of the raceway cavity calculated based on the porosity isoline of 0.7

5.4.4 Heat and mass distribution in the packed bed

Figure 5.10 demonstrates the particles and their respective temperature at three different time steps on horizontal and vertical slices. These horizontal and vertical slices are cut between two XY and XZ planes respectively located at Z=0.15 cm, Z=0.21 cm, and Y=0.27 cm, Y=0.33 cm. As can be seen in the XZ slices (subfigures a-c), the packed bed has increased in height because of the minor fluidization caused by the flow inside the raceway. The packed bed's top surface shows a downward slope from right to left, representing a general anti-clockwise flow flowing through the packed bed.

The particles preheated to an inital temperature of 1300 K. Figure 5.10 shows that as the raceway forms, the temperature of particles around the ring-type zone rises. The ring-type zone is the boundary of the raceway and the location where the incoming air meets the coke particles. The oxygen concentration in this zone is high, causing a high rate of the exothermic oxidation reaction with coke. Heat is produced at a faster rate when the reaction rate is higher, therefore the temperature is raised faster in the areas close to the ring-type zone.

The distribution of O_2 and CO at t=0.1 s , t=1 s and t=20 s can be seen in figure 5.11. In the initial time step (t=0 s) the mass fraction of both O_2 and CO is zero and only Nitrogen (N_2) is

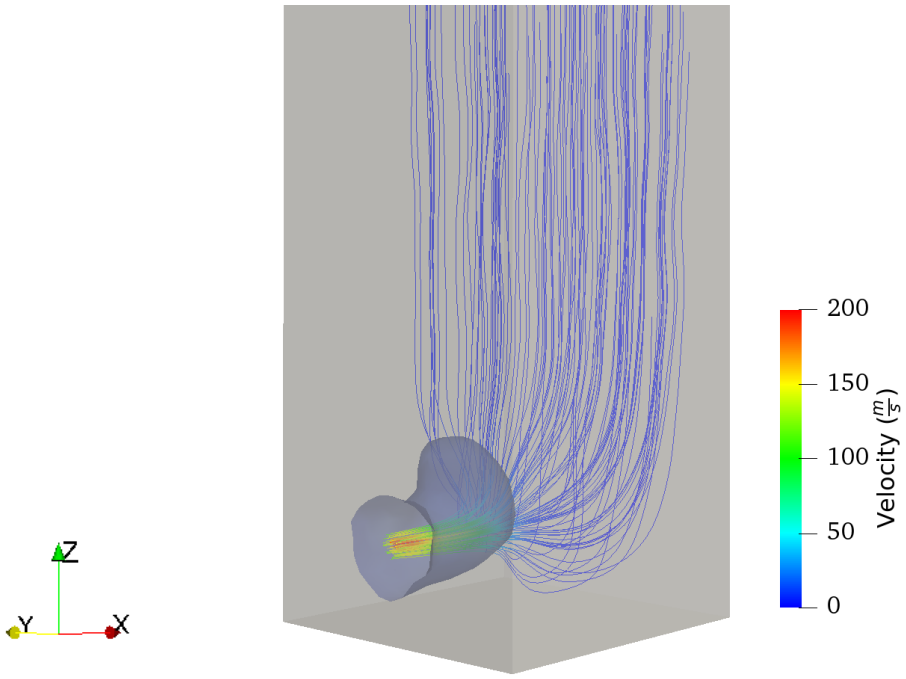

Figure 5.9: Streamlines of the flow passing through raceway for the 3D case with an inlet velocity of 200 m/s. The streamlines are colored by the flow velocity.

present(which is not shown here for the sake of brevity). As the simulation process starts, O_2 is blasted into the furnace and CO is produced. It can be observed that the raceway region is the source of O_2 and distributes it around the packed bed. This explains the correspondence of the O_2 distribution with the raceway shape. However this correspondence is very rough because some O_2 distributs into the packed bed via diffusion and convection and therefore go beyond the raceway perimeter. The O_2 concentration is maximum in the raceway and zero beyond the ring-type zone because the coke particles in the zone consume the O_2 and produce CO. Consequently, due to the outward flow direction around the raceway, CO transports away from the raceway. As a result, CO concentrations inside the raceway are lower than outside.

5.4.5 Influence of blast flow rate

Inlet velocity is a physical parameter that can be manipulated to achieve the desired outcome in the raceway. It directly affects the size of the raceway and thus the distribution of temperature and gas species. In this study, three test cases with inlet velocities of 180 m/s, 200 m/s, and 220 m/s are used to examine the effects of inlet velocity on raceway transport phenomena.

In all the cases, the initial inlet velocity is 10 m/s and it increases linearly with time, up to the desired inlet velocity (180, 200, or 220 m/s) at t=0.5 s. This gradual velocity increase was done both

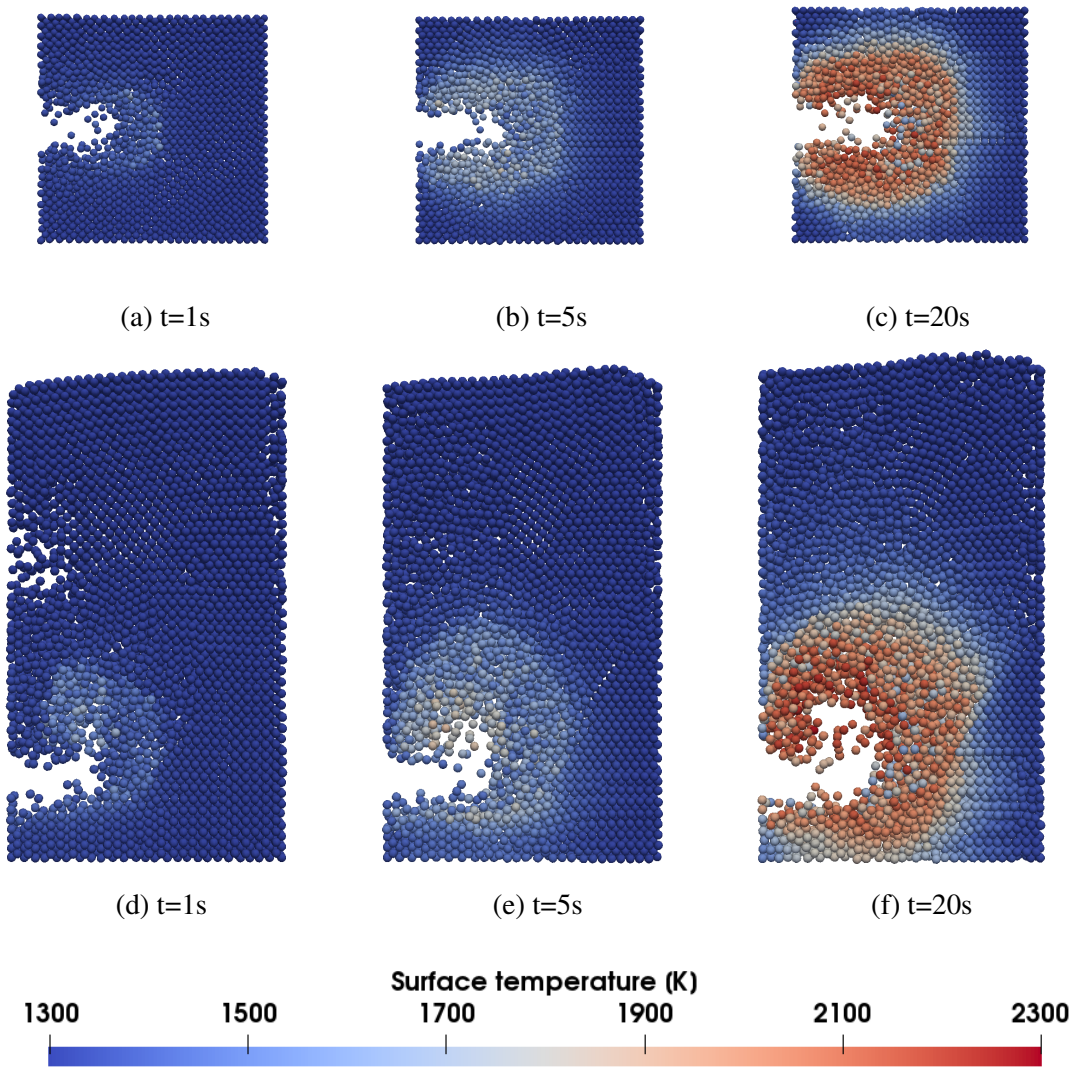

Figure 5.10: Spatial distributions of coke particles in the raceway packed bed at different time steps in a horizontal slice cut from the 3D packed bad, between two XY planes on the opposite sides of the inlet (a,b,c) and a vertical cut between two XZ planes on the opposite sides of the inlet (d,e,f). Particles are colored by the surface temperature of the particles.

for the sake of stability and imitating the actual process. As can be seen in figure 5.12, increasing the inlet velocity results in a larger raceway, thus pushing the ring-type zone outward. As the raceway approaches proximate stability, the volumes of the raceway cavity for 180 m/s, 200 m/s, and 220 m/s are respectively 4.24, 4.72 and 6.56 cubic decimeters. These values are calculated based on considering the raceway as the region with a porosity equal to or larger than 0.7.

Figure 5.12b shows the variation of temperature along the horizontal line starting from the tuyere tip. In all three cases, somewhere in the middle of the horizontal line, there is a temperature peak. The high combustion rate of the particles and the resulting heat causes the temperature to rise. Based

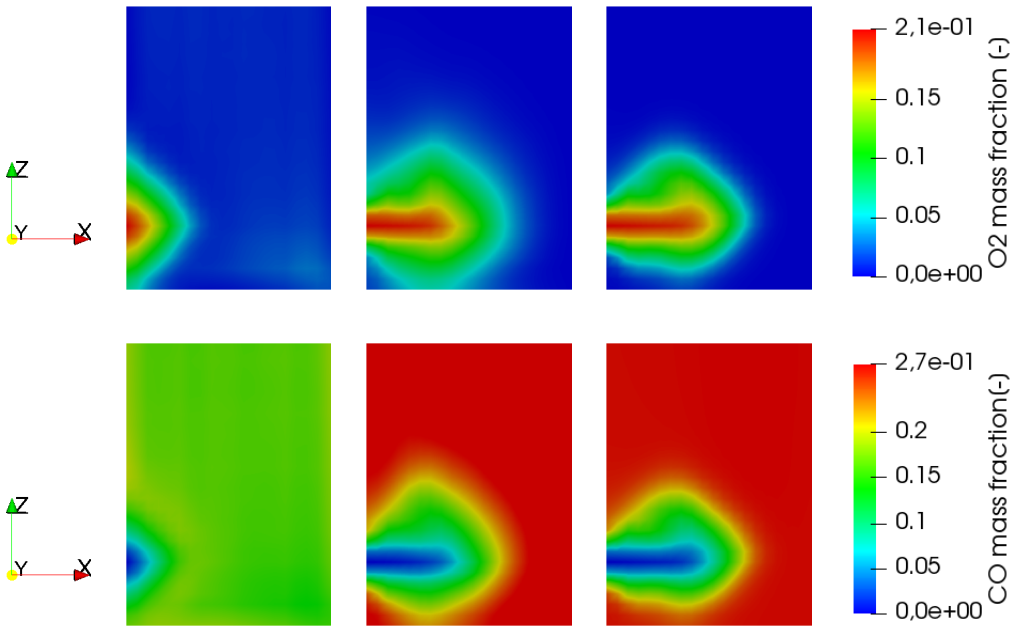

(a) t=0.1s (b) t=1s (c) t=20s

Figure 5.11: O_2 and CO mass fraction distribution in the gas (CFD) at different time steps of the 3D simulation on an XZ slice located on Y=0.3 m which passes the inlet

on the raceway profiles in figure 5.12a these peaks occur in the ring-type zone which is located just outside the raceway perimeter. The same behavior can be observed in O_2 and CO concentration profiles in figure 5.12. As is expected, at the ring-type zone (for instance, between 0.2 m- 0.4 m for 180m/s case), there is a rapid consumption of oxygen, concurrent with the formation of carbon monoxide, which reaches its maximum concentration at the end of the probe line. This consistency of the temperature and concentration profiles with the raceway profile can be observed for all three inlet velocities. However, as the blast inlet velocity is increased, the ring-type zone is pushed further outward therefore the temperature peak and correspondingly the concentration profiles' inclination, occur at a further distance from the tuyere tip.

5.4.6 Heat and mass distribution within the particles

As described in section 5.3.1.2, the DEM model used in this study considers discretized particles. Therefore the heat and mass distributions inside the particles are considered, featuring the internal gradients of temeprature and species concentration within the particles.

Figure 5.13 compares the results between a case with 1-cell particles and a case with 5-cell particles to demonstrate the significance of particle discretization. The primary difference between a 1-cell and a 5-cell particle is that in the 5-cell case there is a gradient of species and temperature

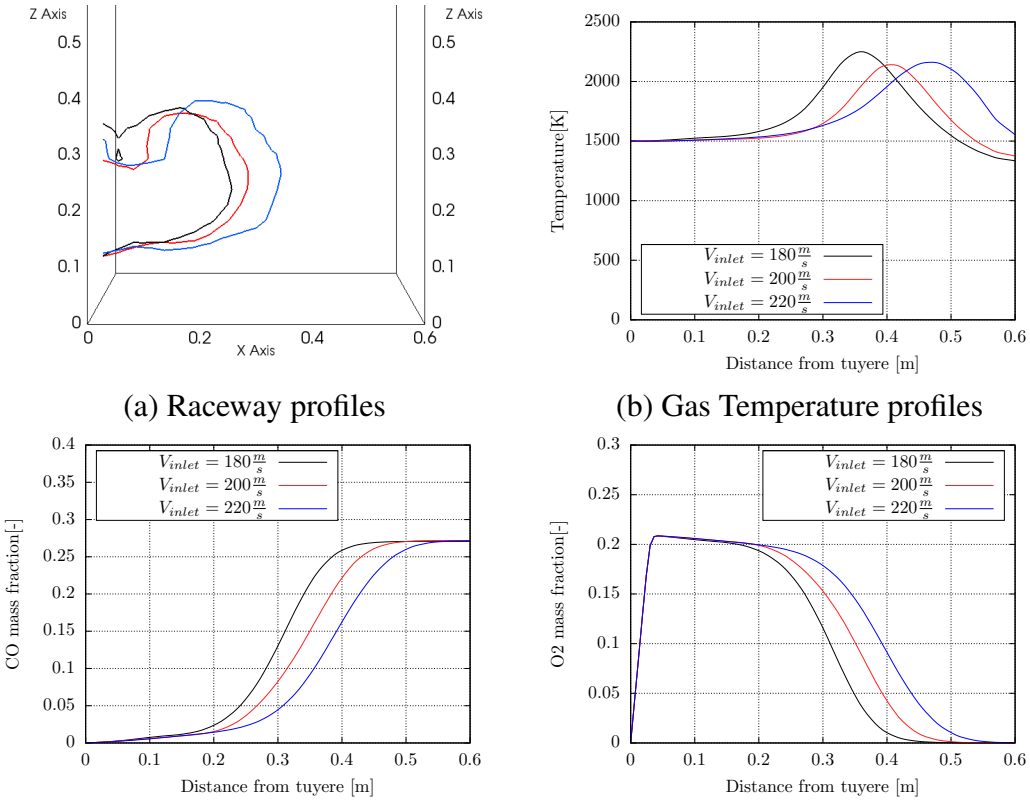

(a) Raceway profiles

(b) Gas Temperature profiles

(c) CO concentration profiles

(d) O_2 concentration profiles

Figure 5.12: Comparison of racewy profile, temperature, CO concentration and O_2 concentration along the horizontal line from the tuyere tip for three differenet velocities 180 m/s (black), 200 m/s (red) and 220 m/s (blue)

within the particle. Coke combustion is driven by oxygen which diffuses into the particle from the ambient gas. Therefore the oxygen concentration has a profile within the particle, decreasing from the surface to the center. The available oxygen concentration determines the rate of coke combustion. Therefore the combustion reaction rate will have a negative gradient from the surface to the center, resulting in more heat generation (due to the exothermic reaction of coke combustion) in the cells near to the surface. Since the particle surface temperature is higher in the 5-cell case, there is a stronger heat convection with the surrounding ambient gas and the gas is thus hotter. This anticipation is clearly demonstrated by figure 5.13(b). The case with 5-cell particles shows a higher gas temperature peak in the ring-type zone. This higher gas temperature creates a higher pressure inside the raceway which pushes the raceway ceiling upward (as there is less resistance to vertical expansion compared to horizontal expansion which is limited by the right wall). This explains the larger raceway cavity for 5-cell particles as illustrated in figure 5.13(a).

However, it is important to note that although in the 5-cell case there is a gradient in reaction rate through the cell, the average reaction rate, or in other words the coke and oxygen consumption is

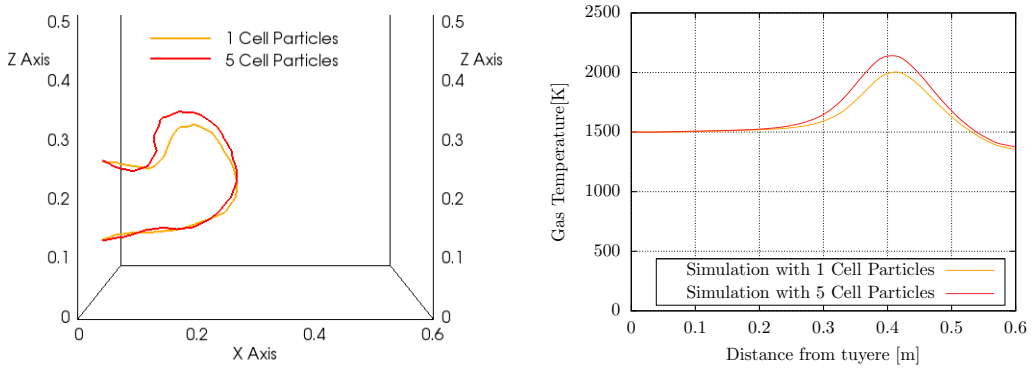

(a) Raceway profiles

(b) Gas Temperature profiles

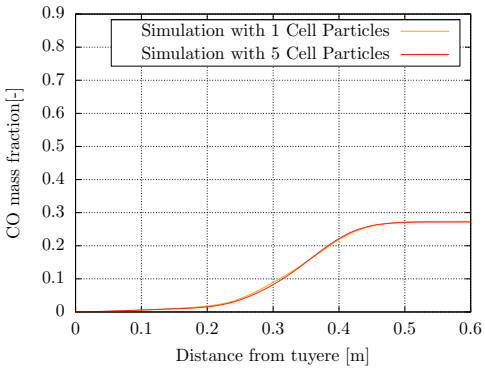

(c) CO concentration profiles

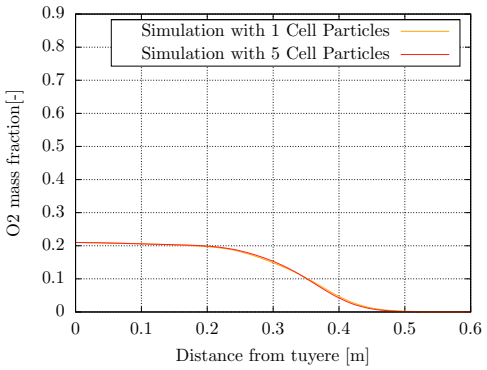

(d) O_2 concentration profiles

Figure 5.13: Comparison of racewy profile, gas temperature, gas CO concentration and gas O_2 concentration along the horizontal line from the tuyere tip for two cases: particles with one internal cell and thus no discretization(Orange) and particles with 5 cells (Red)

almost the same in the two cases. Figures 5.13 (c) and (d) show respectively CO and O_2 concentration along the horizontal line from the tuyere tip. It can be observed that there is almost no difference between the two cases in O_2 consumption and CO production.

The aforementioned gradient of temperature can be significant in some particles that are subject to higher O_2 concentration. Figure 5.14 shows the temperature distribution over the particle radius for two different particles located at different points in the packed bed. Both of these two cases include particles with 20 cells so that this gradient is expressed more clearly. One is inside the ring-type zone, undergoing higher reaction rates and higher temperatures. The other particle, particularly in the second half of simulation, experiences lower temperatures, suggesting that it evaded being trapped in the ring-type zone and maintained a position where heat loss and heat gain by the particle are in equilibrium.

The figures demonstrate the particle discretization which is non-uniform as it was explained in section 5.3.1.2. The cell adjacent to the particle surface adopts a minimum size and towards the center of the particle the cell size increases according to a geometric progression. It can be

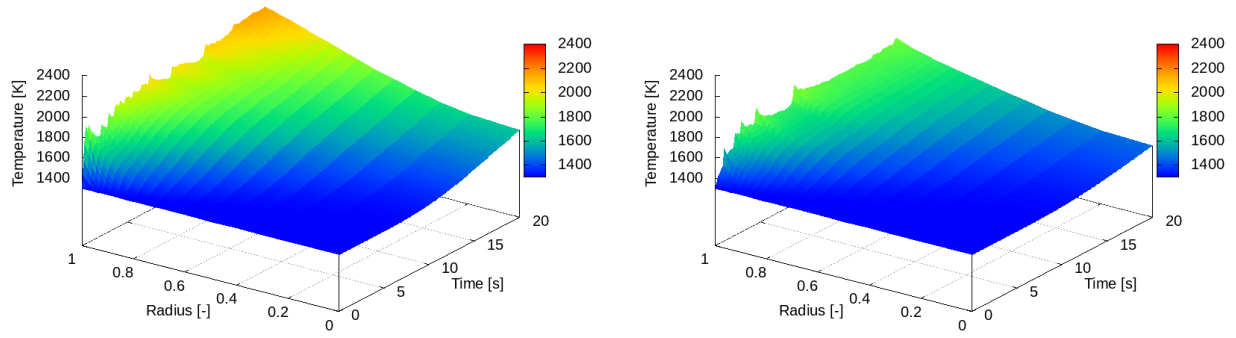

(a) inside the ring-type zone

(b) off the ring-type zone

Figure 5.14: Temporal and spatial distribution of temperature in two coke particles:(a) one, positioned inside the ring-type zone and (b) the other, further away from the ring-type zone

observed that in both cases there is a high gradient of temperature near the surface and this gradient increases over time, because of the low conductivity of coke. This sharp gradient would not be captured in a particle with no discretization [160, 162]. Therefore such models in which the whole particle is considered as a single element with a uniform temperature all over it, incorporate a rough temperature in the Arrhenius model and thus underestimate the reaction rates at the surface of the particle. As demonstrated in previous sections, in an application such as a BF where there is a complex interdependency between the heat transfer, reactions and the dynamics of the system, such gaps in the model will introduce noticeable and unacceptable errors.

5.5 Conclusion

A CFD-DEM model was developed to analyze the raceway transport phenomena in an iron-making blast furnace. The study proposed the significance of simulating the raceway in 3D. Based on the provided results, it was argued that the 2D model, due to the implicit assumptions associated with it, overestimates the raceway size. Therefore the 3D model was used to simulate the raceway and analyze the dynamical evolution of the raceway, combustion of the coke particles, and heat and species distribution in the gas flow.

It was shown that the coke combustion rate is the highest in the periphery of the raceway, known as the ring-type zone. Therefore almost all of the incoming oxygen is consumed near the ring-type zone and the particles in this region experience the highest temperatures. The discretization of the particles made it possible to analyze the heat distribution within the particles. It was shown that for the particles exposed to high oxygen concentration and high combustion rate, the surface of

the particle is subjected to a relatively high temperature gradient. Therefore, in a blast furnace where thermal conductivity of coke particles is low but temperature levels are high, using a DEM model with discretized particles is an effective strategy for preventing the underestimation of particle temperatures.

The influence of the gas inlet velocity was also investigated. It was shown that higher inlet velocity results in larger raceway cavities and more penetration into the path of the packed bed. However, the temperature ranges of the raceway and reaction rates do not follow a clear correlation with the inlet blast flow rate. These findings offer insight into the complex correlations between the dynamics and thermodynamics of the raceway.

Chapter 6

Conclusions and Outlooks

The aim of the present study was to develop a simulation framework capable of modeling the intricate transport phenomena during selective laser melting, particularly the formation and evolution of melt pool, at both multiscale and multi-physics levels.

Selective laser melting (SLM) and electron beam melting (EBM) are additive manufacturing processes used to create metal parts from metal powders. SLM-manufactured parts have found various applications such as in automative, aerospace and medical industries. Researchers continue to grow their application range and resolve the issues associate with their conventional applications.

Among the issues associated with SLM-manufactured parts are the defects and particularly porosities that are rooted in microscale phenomena that arise during powder fusion and solidification of the powder layers. Such microscale culprits may include the characteristics of the very powder that is being used, the trapped gas inside the melt pool, anomalies in powder spreading, behaviors such as balling and spattering that are caused by sporadic nature of the melt pool surface dynamics. Simulation and modeling have been used by researchers and commercial software developers to provide numerical frameworks that facilitate a better insight into the details of an SLM process. One of the key areas of interest in modeling research related to SLM, pertains to the detailed dynamics within and around the melt pool. The behavior of the melt pool, which is directly influenced by process parameters and environmental conditions, is a crucial factor in determining the characteristics of the resulting solidified part and its microstructural properties. However, accurately modeling the melt pool requires accounting for multiple physical phenomena operating at varying length scales.

In the present study a computational fluid dynamics-extended discrete element method (CFD-XDEM) coupling was developed and used to model the dynamics and thermodynamics of the

powder bed and melt pool during SLM. The proposed model can simulate the entire process from the moment of powder deposition on the substrate until the solidification of the melt pool. Within this framework, the discrete element method (XDEM) models various aspects of powder behavior, such as powder deposition, heating via laser radiation, melting and shrinkage, and the associated conduction, radiation, and mass, momentum, and energy transfer between the particles and the surrounding fluid mixture. A 6-way coupling was developed to transfer the source term data between XDEM and CFD. These source terms include mass source of the molten metal, the convective heat transfer between particle and the fluid mixture and drag forces from the liquid to the particles and vice versa. The CFD model is based on volume of fluid (VOF) method and is responsible for simulating the formation and evolution of the melt pool. It considers the surface tension force, Marangoni flow, buoyancy-driven flow inside the melt pool, phase change (solidification and melting) and the laser radiation on the melt surface.

The present study thoroughly tests the reliability of the proposed method at each development stage by validating the model against experimental data and benchmark problems. At the initial stage, the Marangoni model was validated against benchmark problems. In the subsequent stage, the laser model was implemented, and the results of a laser melting experiment on a metal block were predicted. Once the CFD model was finalized, the coupling was developed and a cold model melting experiment was reproduced to validate the reliability of the heat, mass, and momentum transfer of the coupling. This stage marks the completion of the numerical framework for SLM simulation under conduction mode conditions, characterized by relatively low laser power. As a result, the model was employed to predict the outcomes of a low power SLM experiment with a single layer under various laser scanning velocities. The simulation outcomes were found to be in excellent agreement with experimental data and showcased the model's ability to precisely forecast the dimensions of the melt pool. Following this, the model was utilized to simulate a larger powder bed and to examine the characteristics of the melt pool as well as its heat transfer with the powder particles.

To the best of our knowledge, this study represents the first endeavor in the literature to utilize a fully coupled volume-of-fluid computational fluid dynamics (CFD) model and a discrete element method (DEM) model that accounts for heat and mass transfer in addition to momentum for the purpose of simulating the selective laser melting (SLM) process. Here are a few distinctive features of the model:

- A noteworthy feature of the present model is that, unlike conventional approaches that utilize discrete element method (DEM) models solely to generate the powder particles and then represent them as spherical solid geometries, in the current model, the particles are regarded as one-dimensional elements. They are treated as separate entities and are solved for mass, energy, and momentum conservation separately from the CFD domain.It is anticipated that modeling

one-dimensional particles instead of 3-dimensional CFD spherical geometries is computationally more efficient. This is particularly relevant, given that the majority of the particles that become active during the simulation will melt and disappear within a few time steps. In other words, mesh refinement of the particles may impose an unnecessary computational burden on the simulation.

- Phase change of the particles is explicitly solved in the XDEM model. The particles undergo melting at the melting temperature, they shrink and disappear when they are completely melted.
- The XDEM model solves for conduction and radiation between adjacent particles, which offers a significant advantage over continuous powder bed models that require an estimate of effective thermal conductivity.
- The model incorporates all the relevant physical phenomena to the dynamics of the melt pool including Marangoni flow, buoyancy-driven flow and surface tension forces.
- The volumetric heat source for the laser radiation is adaptive to the deformations of the melt surface.
- The CFD model considers the solidification of the melt pool. This is a great leap towards understanding the approximate geometry of the solidified track. The geometry and temperature distribution of the solidified track can be fed into a Phase Field or Cellular Automata (CA) model to predict the microstructre growth of the solidified part.

In summary, the developed simulation framework exhibits promising capabilities in modeling the dynamics of the melt pool. The model has the potential to serve as a fundamental component of a dependable digital twin for both selective laser melting and electron beam melting processes. Nonetheless, there exist specific features that, when integrated into the model, can broaden its scope of applicability. These features are enumerated as follows:

Recommendations for future work

- The present model is capable of modeling the solidification track. This is a significant step towards understanding the process-property relationship in the SLM process. However, to obtain a more comprehensive understanding of the microstructure properties of the material, it is highly recommended to incorporate a microstructure growth model into the simulation. This would enable the prediction the microstructure properties of the solidified track.
- The present model aims to simulate low laser power or conduction model selective laser melting (SLM) processes. However, At higher laser powers boiling and evaporation of the melt pool may highly increase the instabilities of the melt pool. For future work, evaporation and recoil pressure models may also be incorporated.

- Drawing a comparison between the present methodology and traditional pure CFD simulations can prove advantageous to elucidate the potential superiority of the former. Although this comparative study requires a considerable amount of time and effort, the results may as well reveal considerable advantages of the developed method.

Bibliography

[1] Amit Bandyopadhyay and Susmita Bose. *Additive manufacturing*. CRC press, 2019.

[2] Emmanouil L Papazoglou et al. "On the modeling and simulation of SLM and SLS for metal and polymer powders: A review". In: *Archives of Computational Methods in Engineering* (2021), pp. 1–33.

[3] Babis Schoinochoritis, Dimitrios Chantzis, and Konstantinos Salonitis. "Simulation of metallic powder bed additive manufacturing processes with the finite element method: A critical review". In: *Proceedings of the Institution of Mechanical Engineers, Part B: Journal of Engineering Manufacture* 231.1 (2017), pp. 96–117.

[4] Peter S Cook and Anthony B Murphy. "Simulation of melt pool behaviour during additive manufacturing: Underlying physics and progress". In: *Additive Manufacturing* 31 (2020), p. 100909.

[5] Bi Zhang, Yongtao Li, and Qian Bai. "Defect formation mechanisms in selective laser melting: a review". In: *Chinese Journal of Mechanical Engineering* 30 (2017), pp. 515–527.

[6] Behzad Fotovvati et al. "A review on melt-pool characteristics in laser welding of metals". In: *Advances in Materials Science and Engineering* 2018 (2018).

[7] Josefine Svenungsson, Isabelle Choquet, and Alexander FH Kaplan. "Laser welding process–a review of keyhole welding modelling". In: *Physics procedia* 78 (2015), pp. 182–191.

[8] J Alcisto et al. "Tensile properties and microstructures of laser-formed Ti-6Al-4V". In: *Journal of materials engineering and performance* 20 (2011), pp. 203–212.

[9] Stephen Mellor, Liang Hao, and David Zhang. "Additive manufacturing: A framework for implementation". In: *International journal of production economics* 149 (2014), pp. 194–201.

[10] Charles W Hull. *Apparatus for production of three-dimensional objects by stereolithography*. 1984.

[11] Terry Wohlers and Tim Gornet. *History of additive manufacturing*. Wohlers Associates, Inc., 2014.

[12] PM Dickens. "Research developments in rapid prototyping". In: *Proceedings of the Institution of Mechanical Engineers, Part B: Journal of Engineering Manufacture* 209.4 (1995), pp. 261–266.

[13] S Scott Crump. *US5121329 A-Apparatus and method for creating three-dimensional objects*. 1992.

[14] Dionysios E Mouzakis. "Advanced technologies in manufacturing 3D-layered structures for defense and aerospace". In: *Lamination-Theory and Application* 74331 (2018).

[15] Anna Kochan. "Rapid prototyping gains speed, volume and precision". In: *Assembly Automation* 20.4 (2000), pp. 295–299.

[16] Jyoti Mazumder. *Production of smart dies and molds using direct metal deposition*. US Patent 6,937,921. 2005.

[17] Yao Lu et al. "Rapid prototyping of paper-based microfluidics with wax for low-cost, portable bioassay". In: *Electrophoresis* 30.9 (2009), pp. 1497–1500.

[18] Akira Yamada, Fuminori Niikura, and Koji Ikuta. "A three-dimensional microfabrication system for biodegradable polymers with high resolution and biocompatibility". In: *Journal of Micromechanics and Microengineering* 18.2 (2008), p. 025035.

[19] ASTM Standard. "F2792-12a". In: *Standard terminology for additive manufacturing technologies ASTM International, West Conshohocken* (2012).

[20] Kevin Jurrens et al. *Measurement Science Roadmap for Metal-Based Additive Manufacturing*. Tech. rep. National Institute of Standards and Technology, 2013.

[21] ASTM ISO. "ISO/ASTM 52900: 2015 Additive Manufacturing–General Principles–Terminology". In: *ASTM F2792-10e1* 1 (2015), pp. 1–19.

[22] Terry Wohlers and I Campbell. *Wohlers report 2016. Wohlers Associates*. Wohlers Associates, Inc., 2016.

[23] I Campbell et al. *Wohlers Report 2017: 3D Printing and Additive Manufacturing State of the Industry: Annual Worldwide Progress Report*. 2017.

[24] Ian Campbell et al. *Wohlers report 2018: 3D printing and additive manufacturing state of the industry: annual worldwide progress report*. 2018.

[25] TT Wohlers. *Wohlers Report 2022: 3D Printing and Additive Manufacturing state of the industry: annual worldwide progress report*. Wohlers Associates, Inc., 2022.

[26] José A Tamayo et al. "Additive manufacturing of Ti6Al4V alloy via electron beam melting for the development of implants for the biomedical industry". In: *Heliyon* 7.5 (2021), e06892.

[27] Li Yang et al. *Additive manufacturing of metals: the technology, materials, design and production*. Springer, 2017.

[28] John O Milewski and John O Milewski. *Additive manufacturing metal, the art of the possible*. Springer, 2017.

[29] Markus Korpela et al. "Additive manufacturing—Past, present, and the future". In: *Technical, Economic and Societal Effects of Manufacturing 4.0: Automation, Adaption and Manufacturing in Finland and Beyond* (2020), pp. 17–41.

[30] Lishi Jiao et al. "Femtosecond laser produced hydrophobic hierarchical structures on additive manufacturing parts". In: *Nanomaterials* 8.8 (2018), p. 601.

[31] Shoujin Sun, Milan Brandt, and MJLAM Easton. "Powder bed fusion processes: An overview". In: *Laser additive manufacturing* (2017), pp. 55–77.

[32] Harry Shipley et al. "Optimisation of process parameters to address fundamental challenges during selective laser melting of Ti-6Al-4V: A review". In: *International Journal of Machine Tools and Manufacture* 128 (2018), pp. 1–20.

[33] Hiroshige Masuo et al. "Influence of defects, surface roughness and HIP on the fatigue strength of Ti-6Al-4V manufactured by additive manufacturing". In: *International Journal of Fatigue* 117 (2018), pp. 163–179.

[34] S Tammas-Williams et al. "The influence of porosity on fatigue crack initiation in additively manufactured titanium components". In: *Scientific reports* 7.1 (2017), p. 7308.

[35] AE Wilson-Heid, TC Novak, and Allison Michelle Beese. "Characterization of the effects of internal pores on tensile properties of additively manufactured austenitic stainless steel 316L". In: *Experimental Mechanics* 59 (2019), pp. 793–804.

[36] Stefano Beretta and Simone Romano. "A comparison of fatigue strength sensitivity to defects for materials manufactured by AM or traditional processes". In: *International Journal of Fatigue* 94 (2017), pp. 178–191.

[37] Zackary Snow, Abdalla R Nassar, and Edward W Reutzel. "Invited Review Article: Review of the formation and impact of flaws in powder bed fusion additive manufacturing". In: *Additive Manufacturing* 36 (2020), p. 101457.

[38] Ankur K Agrawal, Behzad Rankouhi, and Dan J Thoma. "Predictive process mapping for laser powder bed fusion: A review of existing analytical solutions". In: *Current Opinion in Solid State and Materials Science* 26.6 (2022), p. 101024.

[39] Amir Mostafaei et al. "Defects and anomalies in powder bed fusion metal additive manufacturing". In: *Current Opinion in Solid State and Materials Science* 26.2 (2022), p. 100974.

[40] Cang Zhao et al. "Critical instability at moving keyhole tip generates porosity in laser melting". In: *Science* 370.6520 (2020), pp. 1080–1086.

[41] Ross Cunningham et al. "Keyhole threshold and morphology in laser melting revealed by ultrahigh-speed x-ray imaging". In: *Science* 363.6429 (2019), pp. 849–852.

[42] Zachary A Young et al. "Types of spatter and their features and formation mechanisms in laser powder bed fusion additive manufacturing process". In: *Additive Manufacturing* 36 (2020), p. 101438.

[43] I Yadroitsev et al. "Strategy of manufacturing components with designed internal structure by selective laser melting of metallic powder". In: *Applied Surface Science* 254.4 (2007), pp. 980–983.

[44] Haijun Gong et al. "Analysis of defect generation in Ti–6Al–4V parts made using powder bed fusion additive manufacturing processes". In: *Additive Manufacturing* 1 (2014), pp. 87–98.

[45] Karolien Kempen et al. "Processing AlSi10Mg by selective laser melting: parameter optimisation and material characterisation". In: *Materials Science and Technology* 31.8 (2015), pp. 917–923.

[46] William J Sames et al. "The metallurgy and processing science of metal additive manufacturing". In: *International materials reviews* 61.5 (2016), pp. 315–360.

[47] L Parry, IA Ashcroft, and Ricky D Wildman. "Understanding the effect of laser scan strategy on residual stress in selective laser melting through thermo-mechanical simulation". In: *Additive Manufacturing* 12 (2016), pp. 1–15.

[48] J Robinson et al. "Determination of the effect of scan strategy on residual stress in laser powder bed fusion additive manufacturing". In: *Additive Manufacturing* 23 (2018), pp. 13–24.

[49] Xuan Zhang et al. "Effect of the scanning strategy on microstructure and mechanical anisotropy of Hastelloy X superalloy produced by Laser Powder Bed Fusion". In: *Materials Characterization* 173 (2021), p. 110951.

[50] S Tammas-Williams et al. "XCT analysis of the influence of melt strategies on defect population in Ti–6Al–4V components manufactured by Selective Electron Beam Melting". In: *Materials Characterization* 102 (2015), pp. 47–61.

[51] Deniz Sera Ertay, Henry Ma, and Mihaela Vlasea. "Correlative beam path and pore defect space analysis for modulated powder bed laser fusion process". In: *2018 International Solid Freeform Fabrication Symposium*. University of Texas at Austin. 2018.

[52] Ibiye Aseibichin Roberts et al. "A three-dimensional finite element analysis of the temperature field during laser melting of metal powders in additive layer manufacturing". In: *International Journal of Machine Tools and Manufacture* 49.12-13 (2009), pp. 916–923.

[53] AV Gusarov et al. "Contact thermal conductivity of a powder bed in selective laser sintering". In: *International Journal of Heat and Mass Transfer* 46.6 (2003), pp. 1103–1109.

[54] AV Gusarov et al. "Heat transfer modelling and stability analysis of selective laser melting". In: *Applied Surface Science* 254.4 (2007), pp. 975–979.

[55] Muhammad Mashhood et al. "Developing the AM G-code based thermomechanical finite element platform for the analysis of thermal deformation and stress in metal additive manufacturing process". In: *Journal of Mechanical Science and Technology* (2023), pp. 1–10.

[56] Muhammad Mashhood. "Development of Residual Stress During Part Build in Metal Additive Manufacturing". Available at https://orbilu.uni.lu/handle/10993/54573. PhD thesis. Luxembourg: University of Luxmebourg, 2022.

[57] Weibo Huang and Yimin Zhang. "Finite element simulation of thermal behavior in single-track multiple-layers thin wall without-support during selective laser melting". In: *Journal of Manufacturing Processes* 42 (2019), pp. 139–148.

[58] Pruk Aggarangsi, Jack L Beuth, and Michelle Griffith. "Melt pool size and stress control for laser-based deposition near a free edge". In: *2003 International Solid Freeform Fabrication Symposium*. 2003.

[59] Mischa Jahn et al. "Finite element methods for problems with solid-liquid-solid phase transitions and free melt surface". In: *PAMM* 12.1 (2012), pp. 403–404.

[60] Mahdi Jamshidinia, Fanrong Kong, and Radovan Kovacevic. "The coupled CFD-FEM model of electron beam melting®(EBM)". In: *2003 International Solid Freeform Fabrication Symposium*. 2013.

[61] M Jamshidinia, F Kong, and R Kovacevic. “Temperature distribution and fluid flow modeling of electron beam melting®(EBM)”. In: *ASME International Mechanical Engineering Congress and Exposition*. Vol. 45233. American Society of Mechanical Engineers. 2012, pp. 3089–3101.

[62] V Manvatkar, A De, and Tarasankar DebRoy. “Heat transfer and material flow during laser assisted multi-layer additive manufacturing”. In: *Journal of Applied Physics* 116.12 (2014), p. 124905.

[63] Mustafa Megahed et al. “Metal additive-manufacturing process and residual stress modeling”. In: *Integrating Materials and Manufacturing Innovation* 5 (2016), pp. 61–93.

[64] HW Mindt et al. “Powder bed layer characteristics: the overseen first-order process input”. In: *Metallurgical and Materials Transactions A* 47 (2016), pp. 3811–3822.

[65] HW Mindt et al. “DMLM models-numerical assessment of porosity”. In: *22nd ISABE Conference, Oct*. 2015, pp. 25–30.

[66] Saad A Khairallah et al. “Laser powder-bed fusion additive manufacturing: Physics of complex melt flow and formation mechanisms of pores, spatter, and denudation zones”. In: *Acta Materialia* 108 (2016), pp. 36–45.

[67] Manyalibo J Matthews et al. “Denudation of metal powder layers in laser powder-bed fusion processes”. In: *Additive manufacturing handbook*. CRC Press, 2017, pp. 677–692.

[68] CD Boley, Saad A Khairallah, and Alexander M Rubenchik. “Calculation of laser absorption by metal powders in additive manufacturing”. In: *Applied optics* 54.9 (2015), pp. 2477–2482.

[69] Wayne King et al. “Overview of modelling and simulation of metal powder bed fusion process at Lawrence Livermore National Laboratory”. In: *Materials Science and Technology* 31.8 (2015), pp. 957–968.

[70] F-J Gürtler et al. “Simulation of laser beam melting of steel powders using the three-dimensional volume of fluid method”. In: *Physics Procedia* 41 (2013), pp. 881–886.

[71] F-J Gürtler et al. “Influence of powder distribution on process stability in laser beam melting: Analysis of melt pool dynamics by numerical simulations”. In: *2014 International Solid Freeform Fabrication Symposium*. University of Texas at Austin. 2014.

[72] Chinnapat Panwisawas et al. “Keyhole formation and thermal fluid flow-induced porosity during laser fusion welding in titanium alloys: Experimental and modelling”. In: *Acta materialia* 126 (2017), pp. 251–263.

[73] Chunlei Qiu et al. “On the role of melt flow into the surface structure and porosity development during selective laser melting”. In: *Acta Materialia* 96 (2015), pp. 72–79.

[74] Chinnapat Panwisawas et al. “Modelling of thermal fluid dynamics for fusion welding”. In: *Journal of Materials Processing Technology* 252 (2018), pp. 176–182.

[75] YS Lee and Wei Zhang. “Modeling of heat transfer, fluid flow and solidification microstructure of nickel-base superalloy fabricated by laser powder bed fusion”. In: *Additive Manufacturing* 12 (2016), pp. 178–188.

[76] Yousub Lee. *Simulation of laser additive manufacturing and its applications*. The Ohio State University, 2015.

[77] Carolin Körner, Elham Attar, and Peter Heinl. “Mesoscopic simulation of selective beam melting processes”. In: *Journal of Materials Processing Technology* 211.6 (2011), pp. 978–987.

[78] Carolin Körner, Andreas Bauereiß, and Elham Attar. “Fundamental consolidation mechanisms during selective beam melting of powders”. In: *Modelling and Simulation in Materials Science and Engineering* 21.8 (2013), p. 085011.

[79] Regina Ammer et al. “Simulating fast electron beam melting with a parallel thermal free surface lattice Boltzmann method”. In: *Computers & Mathematics with Applications* 67.2 (2014), pp. 318–330.

[80] Regina Ammer et al. “Validation experiments for LBM simulations of electron beam melting”. In: *International Journal of Modern Physics C* 25.12 (2014), p. 1441009.

[81] Alexander Klassen et al. “Numerical simulation of multi-component evaporation during selective electron beam melting of TiAl”. In: *Journal of Materials Processing Technology* 247 (2017), pp. 280–288.

[82] Gui-Rong Liu and Moubin B Liu. *Smoothed particle hydrodynamics: a meshfree particle method*. World scientific, 2003.

[83] Deepak Shah and Alexey N Volkov. “Numerical simulations of thermal transport in random porous materials and powder systems using the smoothed particle hydrodynamics method”. In: *ASME International Mechanical Engineering Congress and Exposition*. Vol. 58356. American Society of Mechanical Engineers. 2017, V002T02A019.

[84] MA Russell, A Souto-Iglesias, and TI3845621 Zohdi. “Numerical simulation of Laser Fusion Additive Manufacturing processes using the SPH method”. In: *Computer Methods in Applied Mechanics and Engineering* 341 (2018), pp. 163–187.

[85] Claas Bierwisch. “DEM powder spreadingand SPH powder melting models for additive manufacturing processsimulations”. In: *2015 International Solid Freeform Fabrication Symposium*. CIMNE, 2019.

[86] Peter A Cundall and Otto DL Strack. “A discrete numerical model for granular assemblies”. In: *geotechnique* 29.1 (1979), pp. 47–65.

[87] YS Lee and W Zhang. “Mesoscopic simulation of heat transfer and fluid flow in laser powder bed additive manufacturing”. In: *2015 International Solid Freeform Fabrication Symposium*. University of Texas at Austin. 2015.

[88] Trong-Nhan Le et al. “Numerical and experimental investigation into powder entrainment and denudation phenomena in laser powder bed fusion process”. In: *Powder Technology* 410 (2022), p. 117907.

[89] Tao Yu and Jidong Zhao. “Semi-coupled resolved CFD–DEM simulation of powder-based selective laser melting for additive manufacturing”. In: *Computer Methods in Applied Mechanics and Engineering* 377 (2021), p. 113707.

[90] Alvaro Antonio Estupinan Donoso and Bernhard Peters. “Exploring a multiphysics resolution approach for additive manufacturing”. In: *JOM* 70.8 (2018), pp. 1604–1610.

[91] T DebRoy et al. “Metallurgy, mechanistic models and machine learning in metal printing”. In: *Nature Reviews Materials* 6.1 (2021), pp. 48–68.

[92] Alexander Klassen, Thorsten Scharowsky, and Carolin Körner. “Evaporation model for beam based additive manufacturing using free surface lattice Boltzmann methods”. In: *Journal of Physics D: Applied Physics* 47.27 (2014), p. 275303.

[93] Zhidong Zhang et al. “3-Dimensional heat transfer modeling for laser powder-bed fusion additive manufacturing with volumetric heat sources based on varied thermal conductivity and absorptivity”. In: *Optics & Laser Technology* 109 (2019), pp. 297–312.

[94] Jung-Ho Cho and Suck-Joo Na. “Implementation of real-time multiple reflection and Fresnel absorption of laser beam in keyhole”. In: *Journal of Physics D: Applied Physics* 39.24 (2006), p. 5372.

[95] AV Gusarov et al. “Model of radiation and heat transfer in laser-powder interaction zone at selective laser melting”. In: *Journal of heat transfer* 131.7 (2009).

[96] Rishi Ganeriwala and Tarek I Zohdi. “A coupled discrete element-finite difference model of selective laser sintering”. In: *Granular Matter* 18.2 (2016), pp. 1–15.

[97] Bernhard Peters et al. “XDEM multi-physics and multi-scale simulation technology: Review of DEM–CFD coupling, methodology and engineering applications”. In: *Particuology* 44 (2019), pp. 176–193.

[98] Mehdi Baniasadi, Maryam Baniasadi, and Bernhard Peters. “Coupled CFD-DEM with heat and mass transfer to investigate the melting of a granular packed bed”. In: *Chemical Engineering Science* 178 (2018), pp. 136–145.

[99] Bernhard Peters. *Thermal conversion of solid fuels*. WIT Press, 2002.

[100] Jeremiah U Brackbill, Douglas B Kothe, and Charles Zemach. "A continuum method for modeling surface tension". In: *Journal of computational physics* 100.2 (1992), pp. 335–354.

[101] Liu Cao. "Numerical simulation of the impact of laying powder on selective laser melting single-pass formation". In: *International Journal of Heat and Mass Transfer* 141 (2019), pp. 1036–1048.

[102] X He, PW Fuerschbach, and T DebRoy. "Heat transfer and fluid flow during laser spot welding of 304 stainless steel". In: *Journal of Physics D: Applied Physics* 36.12 (2003), p. 1388.

[103] Wenda Tan, Neil S Bailey, and Yung C Shin. "Numerical modeling of transport phenomena and dendritic growth in laser spot conduction welding of 304 stainless steel". In: *Journal of manufacturing science and engineering* 134.4 (2012).

[104] Ajay Kumar Shukla et al. "Cold model investigations of melting of ice in a gas-stirred vessel". In: *Metallurgical and materials transactions B* 42.1 (2011), pp. 224–235.

[105] YL Hao and Y-X Tao. "Non-thermal equilibrium melting of granular packed bed in horizontal forced convection. Part I: experiment". In: *International journal of heat and mass transfer* 46.26 (2003), pp. 5017–5030.

[106] Jian Yang et al. "Computational study of forced convective heat transfer in structured packed beds with spherical or ellipsoidal particles". In: *Chemical engineering science* 65.2 (2010), pp. 726–738.

[107] Harris L Marcus et al. "Solid Freeform Fabrication Symposium Proceedings". In: *NASA STI/Recon Technical Report N* 94 (1993), p. 33441.

[108] Alexander Katz-Demyanetz et al. "Powder-bed additive manufacturing for aerospace application: Techniques, metallic and metal/ceramic composite materials and trends". In: *Manufacturing review* 6 (2019).

[109] Andreas Kirchheim et al. "Dynamic conformal cooling improves injection molding: Hybrid molds manufactured by laser powder bed fusion". In: *The International Journal of Advanced Manufacturing Technology* 114 (2021), pp. 107–116.

[110] Charles R Fisher and Caroline E Vail. "Computational simulation of an additively manufactured marine component". In: *Journal of Materials Engineering and Performance* 28 (2019), pp. 627–632.

[111] AN Aufa, Mohamad Zaki Hassan, and Zarini Ismail. "Recent advances in Ti-6Al-4V additively manufactured by selective laser melting for biomedical implants: Prospect development". In: *Journal of Alloys and Compounds* 896 (2022), p. 163072.

[112] Niloofar Sanaei and Ali Fatemi. “Defects in additive manufactured metals and their effect on fatigue performance: A state-of-the-art review”. In: *Progress in Materials Science* 117 (2021), p. 100724.

[113] Chu Lun Alex Leung et al. “In situ X-ray imaging of defect and molten pool dynamics in laser additive manufacturing”. In: *Nature communications* 9.1 (2018), p. 1355.

[114] Antonella Sola and Alireza Nouri. “Microstructural porosity in additive manufacturing: The formation and detection of pores in metal parts fabricated by powder bed fusion”. In: *Journal of Advanced Manufacturing and Processing* 1.3 (2019), e10021.

[115] Ankur Kumar Agrawal, Gabriel Meric de Bellefon, and Dan Thoma. “High-throughput experimentation for microstructural design in additively manufactured 316L stainless steel”. In: *Materials Science and Engineering: A* 793 (2020), p. 139841.

[116] Tomasz Kurzynowski et al. “Effect of scanning and support strategies on relative density of SLM-ed H13 steel in relation to specimen size”. In: *Materials* 12.2 (2019), p. 239.

[117] C Pauzon et al. “Effect of the process gas and scan speed on the properties and productivity of thin 316L structures produced by laser-powder bed fusion”. In: *Metallurgical and Materials Transactions A* 51 (2020), pp. 5339–5350.

[118] Aiden A Martin et al. “Ultrafast dynamics of laser-metal interactions in additive manufacturing alloys captured by in situ X-ray imaging”. In: *Materials Today Advances* 1 (2019), p. 100002.

[119] Jared Gillespie et al. “In situ characterization of laser-generated melt pools using synchronized ultrasound and high-speed X-ray imaging”. In: *The Journal of the Acoustical Society of America* 150.4 (2021), pp. 2409–2420.

[120] Leila Ladani et al. “Effective liquid conductivity for improved simulation of thermal transport in laser beam melting powder bed technology”. In: *Additive Manufacturing* 14 (2017), pp. 13–23.

[121] Donghua Dai and Dongdong Gu. “Effect of metal vaporization behavior on keyhole-mode surface morphology of selective laser melted composites using different protective atmospheres”. In: *Applied Surface Science* 355 (2015), pp. 310–319.

[122] Donghua Dai and Dongdong Gu. “Influence of thermodynamics within molten pool on migration and distribution state of reinforcement during selective laser melting of AlN/AlSi10Mg composites”. In: *International Journal of Machine Tools and Manufacture* 100 (2016), pp. 14–24.

[123] Aiden A Martin et al. “Dynamics of pore formation during laser powder bed fusion additive manufacturing”. In: *Nature communications* 10.1 (2019), p. 1987.

[124] Sonny Ly et al. “Metal vapor micro-jet controls material redistribution in laser powder bed fusion additive manufacturing”. In: *Scientific reports* 7.1 (2017), p. 4085.

[125] Andre Mussatto et al. “Influences of powder morphology and spreading parameters on the powder bed topography uniformity in powder bed fusion metal additive manufacturing”. In: *Additive Manufacturing* 38 (2021), p. 101807.

[126] Thomas R Watkins et al. “Residual stresses and microstructure within Allvac 718Plus laser powder bed fusion bars”. In: *Additive Manufacturing* 47 (2021), p. 102334.

[127] Yanming Zhang et al. “Dispersion of reinforcing micro-particles in the powder bed fusion additive manufacturing of metal matrix composites”. In: *Acta Materialia* 235 (2022), p. 118086.

[128] Navid Aminnia, Alvaro Antonio Estupinan Donoso, and Bernhard Peters. “Developing a DEM-Coupled OpenFOAM solver for multiphysics simulation of additive manufacturing process”. In: *Proceedings of the 8th European Congress on Computational Methods in Applied Sciences and Engineering*. Eccomas, 2022.

[129] Cyril W Hirt and Billy D Nichols. “Volume of fluid (VOF) method for the dynamics of free boundaries”. In: *Journal of computational physics* 39.1 (1981), pp. 201–225.

[130] Vaughan R Voller and Chander Prakash. “A fixed grid numerical modelling methodology for convection-diffusion mushy region phase-change problems”. In: *International journal of heat and mass transfer* 30.8 (1987), pp. 1709–1719.

[131] AD Brent, Vaughan R Voller, and KTJ Reid. “Enthalpy-porosity technique for modeling convection-diffusion phase change: application to the melting of a pure metal”. In: *Numerical Heat Transfer, Part A Applications* 13.3 (1988), pp. 297–318.

[132] Jian Yang et al. “Experimental analysis of forced convective heat transfer in novel structured packed beds of particles”. In: *Chemical engineering science* 71 (2012), pp. 126–137.

[133] Zekun Wang et al. “Powder-scale multi-physics modeling of multi-layer multi-track selective laser melting with sharp interface capturing method”. In: *Computational Mechanics* 63 (2019), pp. 649–661.

[134] Zhengtao Gan et al. “Benchmark study of thermal behavior, surface topography, and dendritic microstructure in selective laser melting of Inconel 625”. In: *Integrating Materials and Manufacturing Innovation* 8 (2019), pp. 178–193.

[135] T Mukherjee et al. “Heat and fluid flow modeling to examine 3D-printability of alloys”. In: *7th International Symposium on High-Temperature Metallurgical Processing*. Springer. 2016, pp. 471–478.

[136] Yu-Che Wu et al. “Parametric study of surface morphology for selective laser melting on Ti6Al4V powder bed with numerical and experimental methods”. In: *International Journal of Material Forming* 11 (2018), pp. 807–813.

[137] Kenneth C Mills. *Recommended values of thermophysical properties for selected commercial alloys*. Woodhead Publishing, 2002.

[138] Heng Xiao and Jin Sun. “Algorithms in a robust hybrid CFD-DEM solver for particle-laden flows”. In: *Communications in Computational Physics* 9.2 (2011), pp. 297–323.

[139] Umberto Scipioni Bertoli et al. “In-situ characterization of laser-powder interaction and cooling rates through high-speed imaging of powder bed fusion additive manufacturing”. In: *Materials & Design* 135 (2017), pp. 385–396.

[140] WH Lee. “A pressure iteration scheme for two-phase flow modeling. Multiphase Transport Fundamentals, Reactor Safety, Applications”. In: *Hemisphere Publishing, Washington, DC* (1980).

[141] Michael F Zäh and S Lutzmann. “Modelling and simulation of electron beam melting”. In: *Production Engineering* 4.1 (2010), pp. 15–23.

[142] Wenxuan Zhang et al. “Understanding the Rayleigh instability in humping phenomenon during laser powder bed fusion process”. In: *International Journal of Extreme Manufacturing* 4.1 (2022), p. 015201.

[143] Qi Zhang et al. “Comprehensive assessment of energy conservation and CO2 emissions mitigation in China’s iron and steel industry based on dynamic material flows”. In: *Applied Energy* 209 (2018), pp. 251–265.

[144] Jose Adilson de Castro, Cyro Takano, and Jun-ichiro Yagi. “A theoretical study using the multiphase numerical simulation technique for effective use of H2 as blast furnaces fuel”. In: *Journal of Materials Research and Technology* 6.3 (2017), pp. 258–270.

[145] XU Chunbao Charles and Da-qiang Cang. “A brief overview of low CO2 emission technologies for iron and steel making”. In: *Journal of Iron and Steel Research, International* 17.3 (2010), pp. 1–7.

[146] Wenqiang Sun et al. “Material and energy flows of the iron and steel industry: Status quo, challenges and perspectives”. In: *Applied Energy* 268 (2020), p. 114946.

[147] Yansong Shen et al. “Three-dimensional modeling of flow and thermochemical behavior in a blast furnace”. In: *Metallurgical and Materials Transactions B* 46.1 (2015), pp. 432–448.

[148] S Dong et al. “Characterization of tuyere-level core-drill coke samples from blast furnace operation”. In: *Energy & fuels* 21.6 (2007), pp. 3446–3454.

[149] Yoshiyuki MATSUI et al. “Analyses on blast furnace raceway formation by micro wave reflection gunned through tuyere”. In: *ISIJ international* 45.10 (2005), pp. 1432–1438.

[150] GSSRK Sastry, GS Gupta, and AK Lahiri. “Cold model study of raceway under mixed particle conditions”. In: *Ironmaking & steelmaking* 30.1 (2003), pp. 61–65.

[151] GSSRK Sastry. “Void formation and breaking in a packed bed”. In: *ISIJ international* 43.2 (2003), pp. 153–160.

[152] Ruixuan Zhang et al. “Image-based flame detection and combustion analysis for blast furnace raceway”. In: *IEEE Transactions on instrumentation and measurement* 68.4 (2019), pp. 1120–1131.

[153] SS Mondal, SK Som, and SK Dash. “Numerical predictions on the influences of the air blast velocity, initial bed porosity and bed height on the shape and size of raceway zone in a blast furnace”. In: *Journal of Physics D: Applied Physics* 38.8 (2005), p. 1301.

[154] Xiaoping Qiu et al. “A simplified two-fluid model coupled with EMMS drag for gas-solid flows”. In: *Powder technology* 314 (2017), pp. 299–314.

[155] WJ Yang, ZY Zhou, and AB Yu. “Discrete particle simulation of solid flow in a three-dimensional blast furnace sector model”. In: *Chemical Engineering Journal* 278 (2015), pp. 339–352.

[156] BH Xu et al. “A numerical and experimental study of the gas-solid flow in a fluid bed reactor”. In: *Powder Handling & Processing* 13.1 (2001), pp. 71–76.

[157] Yu-Qing Feng et al. “Numerical study of gas-solid flow in the raceway of a blast furnace”. In: *steel research international* 74.9 (2003), pp. 523–530.

[158] Shinichi Yuu, Toshihiko Umekage, and Masatomo Kadowaki. “Numerical simulation of particle and air velocity fields in raceway in model blast furnace and comparison with experimental data (cold model)”. In: *ISIJ international* 50.8 (2010), pp. 1107–1116.

[159] JE Hilton and PW Cleary. “Raceway formation in laterally gas-driven particle beds”. In: *Chemical engineering science* 80 (2012), pp. 306–316.

[160] Shuai Wang and Yansong Shen. “CFD-DEM modelling of raceway dynamics and coke combustion in an ironmaking blast furnace”. In: *Fuel* 302 (2021), p. 121167.

[161] Zhen Miao et al. “CFD-DEM simulation of raceway formation in an ironmaking blast furnace”. In: *Powder technology* 314 (2017), pp. 542–549.

[162] Jiaxin Cui, Qinfu Hou, and Yansong Shen. “CFD-DEM study of coke combustion in the raceway cavity of an ironmaking blast furnace”. In: *Powder Technology* 362 (2020), pp. 539–549.

[163] E Dianyu et al. “Particle-scale study of coke combustion in the raceway of an ironmaking blast furnace”. In: *Fuel* 311 (2022), p. 122490.

[164] Yuting Zhuo, Zhongjie Hu, and Yansong Shen. “CFD study of hydrogen injection through tuyeres into ironmaking blast furnaces”. In: *Fuel* 302 (2021), p. 120804.

[165] Tao Li et al. “Numerical Simulation Study on the Effects of Co-Injection of Pulverized Coal and Hydrochar into the Blast Furnace”. In: *Sustainability* 14.8 (2022), p. 4407.

[166] Tyamo Okosun, Samuel Nielson, and Chenn Zhou. “Blast Furnace Hydrogen Injection: Investigating Impacts and Feasibility with Computational Fluid Dynamics”. In: *JOM* 74.4 (2022), pp. 1521–1532.

[167] Bernhard Peters. *Thermal conversion of solid fuels*. eng. International series on developments in heat transfer Vol. 15 15. Southampton: WIT Press, 2003. ISBN: 1-85312-953-4.

[168] Thomas Fred Eric Rhead and Richard Vernon Wheeler. “CCXXVI.—The effect of temperature on the equilibrium 2CO⇌CO 2+ C”. In: *Journal of the Chemical Society, Transactions* 97 (1910), pp. 2178–2189.

[169] Tao Zhao. *Coupled DEM-CFD analyses of landslide-induced debris flows*. Springer, 2017.

[170] Dimitri Gidaspow. *Multiphase flow and fluidization: continuum and kinetic theory descriptions*. Academic press, 1994.

[171] CY Wen and YH Yu. “Mechanics of fluidization”. In: *The Chemical Engineering* 162 (1966), pp. 100–111.

[172] Sabri Ergun and Ao Ao Orning. “Fluid flow through randomly packed columns and fluidized beds”. In: *Industrial & Engineering Chemistry* 41.6 (1949), pp. 1179–1184.

[173] Edder Rabadan Santana, Gabriele Pozzetti, and Bernhard Peters. “Application of a dual-grid multiscale CFD-DEM coupling method to model the raceway dynamics in packed bed reactors”. In: *Chemical Engineering Science* 205 (2019), pp. 46–57.

[174] Hiroshi Nogami, Hideyuki Yamaoka, and Kouji Takatani. “Raceway design for the innovative blast furnace”. In: *ISIJ international* 44.12 (2004), pp. 2150–2158.